Optimization of Embedded Atom Method Interatomic Potentials to Simulate Defect Structures and Magnetism in α-Fe

THÈSE N^{O} 4775 (2010)

PRÉSENTÉE LE 30 AOÛT 2010

À LA FACULTÉ SCIENCES ET TECHNIQUES DE L'INGÉNIEUR
LABORATOIRE DE MÉTALLURGIE MÉCANIQUE
PROGRAMME DOCTORAL EN SCIENCE ET GÉNIE DES MATÉRIAUX

ÉCOLE POLYTECHNIQUE FÉDÉRALE DE LAUSANNE

POUR L'OBTENTION DU GRADE DE DOCTEUR ÈS SCIENCES

PAR

Samuele CHIESA

acceptée sur proposition du jury:

Prof. A. Mortensen, président du jury
Prof. H. Van Swygenhoven, directrice de thèse
Dr A. Curioni, rapporteur
Prof. E. Kaxiras, rapporteur
Dr F. Willaime, rapporteur

ÉCOLE POLYTECHNIQUE
FÉDÉRALE DE LAUSANNE

Suisse
2010

Acknowledgements

Prof. Helena Van Swygenhoven-Moens, for continuous support to this project and wise direction of my thesis.
Dr. Peter Derlet, for passionate supervision and for giving me permission to use and modify his Fortran codes.
Dr. Sergei Dudarev, for illuminating discussions and advices.
The European Fusion Development Agreement and PSI, for funding this work.
Prof. Jean-Louis Soulié for correcting the French version of the abstract.
Dr. Mark Gilbert, for his efforts and collaboration to the problem of the screw dislocation core structure.
Dr. Christian Brandl, for installing VASP and his unvaluable help in the calculation of the third order elastic constants.
Dr. Andreas Elsener and Dr. Erik Bitzek, for their help at the beginning of my PhD.
Ning Gao, for his contagious passion for molecular dynamics.
The MSS group, for interesting discussions during lunch time.
Thanks to all my friends and parents for letting me forget, from time to time, about this work. And, last but not least, thanks to Camille for everything else.

Abstract

Magnetism is largely responsible for the body centered cubic to face centered cubic structural phase transition occurring in iron at 1185 K and to many anomalies in the vicinity of the ferromagnetic to paramagnetic phase transition at 1043 K, as for instance an anomalous softening of the tetrahedral shear modulus. Current atomistic models including magnetism are either limited to the treatment of perfect lattice models or to zero temperatures, while research and development of candidate materials for future fission and fusion power plants requires the modeling of irradiation induced defects in ferritic/martensitic steels at high temperatures. An attempt to fill this gap is the Dudarev-Derlet potential, which includes zero temperature magnetism in an embedded atom method formalism, together with a more recent extension of the method to the inclusion of spin rotations at non zero temperature with nearly half the computational speed of an embedded atom method potential. In this work, we report on the optimization of the Dudarev-Derlet potential to the zero temperature bulk properties of the non-magnetic and ferromagnetic bcc and fcc phases, including the third order elastic constants of the ferromagnetic bcc phase, the point defects formation and migration energies and the core structure of the screw dislocation with Burgers vector 1/2[111], either from experiments or from density functional theory calculations, where we develop a method to fit the core structure of the screw dislocation based on the Suzuki-Takeuchi model. Three representative fits from the optimization of the Dudarev-Derlet potential are compared with recent semi empirical potentials for iron, with density functional theory and experiments. The migration energies of the self-interstitial range from 0.31 eV to 0.42 eV, compared to a density functional theory value close to 0.35 eV and an experimental value close to 0.3 eV, and the vacancy migration energies range from 0.85 eV to 0.94 eV, compared to a density functional theory value close to 0.65 eV. Clusters composed of parallel self-interstitials are oriented along $\langle 110 \rangle$ if the number of interstitials composing the cluster is smaller or equal than 3, while for bigger clusters the $\langle 111 \rangle$ orientation is more stable, in qualitative agreement with density functional theory. Depending on which one of the three representative fits is chosen, the formation entropy of one $\langle 110 \rangle$ dumbbell calculated by the thermodynamical integration method in the range from 300 K to 600 K varies from 0.28 k_B to 4.02 k_B. The diffusion coefficient of the $\langle 110 \rangle$ dumbbell at 600 K ranges from 1×10^{-6} cm^2/s to 10×10^{-6} cm^2/s, while at room temperatures the scatters extends over three orders of magnitude. The main difficulties, common to all the semi empirical potentials considered in this work, are related to the description

of the fcc phase and the migration mechanism of the screw dislocation. The semi empirical potentials are unable to distinguish the anti-ferromagnetic fcc from the low spin ferromagnetic fcc or the high spin ferromagnetic fcc. Considering the equilibrium volume and the bulk magnetic moment, the high spin phase is the one which most resembles the ferromagnetic fcc phase of the Dudarev-Derlet potentials. Finally, for those fits with a non-degenerate core structure, we investigate some fundamental aspects of the migration mechanism of the screw dislocation with Burgers vector 1/2[111] at zero temperature and at zero applied stress, by calculating the Peierls potential in the $[\overline{2}11]$ direction between two structurally equivalent soft cores. This confirms the existence of a stable core structure in the middle of the migration path not observed in density functional theory, which is actually found to be energetically degenerate with the soft core. The consequences of this are discussed in terms of formation energies of double kinks in the $[\overline{2}11]$ direction.

Keywords: iron, magnetism, embedded atom method, interatomic potential, radiation damage, optimization, third order elastic constants, formation free energy, point defects, clusters, diffusion coefficient, screw dislocation core, Peierls potential, kinks, formation energy, formation volume, migration energy, Suzuki-Takeuchi model, Frenkel-Kontorova model.

Résumé

Le magnétisme est largement responsable de la transition de phase entre la structure cubique centrée et la structure cubique à faces centrées, qui a lieu dans le fer à une température de 1185 K, et de plusieurs anomalies à l'approche de la température de transition entre l'état ferromagnétique et paramagnétique à 1043 K, comme par exemple une diminution anormale de la constante élastique tétragonale. Les modèles atomistiques courants incluant le magnétisme sont, soit limités à des réseaux cristallins, soit à des simulations statiques, alors que la recherche et le développement de matériaux pour les nouveaux réacteurs à fission ou à fusion nécessite une modélisation des défauts produits par l'irradiation, dans des aciers ferritiques-martensitiques à haute température. Le potentiel de Dudarev et Derlet est une tentative pour combler cette lacune. La caractéristique principale de ce potentiel est d'inclure le magnétisme au zéro absolu dans un formalisme équivalent au modèle de l'atome entouré. Une adjonction récente permet à ce même formalisme de prendre en compte la rotation des spins à toute température. L'effet de cette extension sur le temps de calcul est d'à peine le doubler. Dans ce travail, nous avons optimisé le potentiel de Dudarev et Derlet par rapport aux propriétés élastiques et d'équilibre des phases magnétiques ou non magnétiques des structures CFC ou CC, en incluant aussi, mais seulement pour la phase magnétique CC, les constantes élastiques de troisième ordre, les énergies de formation et de migration des défauts ponctuels, et la structure du coeur de la dislocation vis avec un vecteur de Burgers égal à 1/2[111]. Ces informations sont dérivées soit des expériences soit de la théorie de la fonctionnelle de la densité. Pour contrôler la structure du coeur de la dislocation vis on a développé une méthode basée sur le modèle de Suzuki et Takeuchi. Nous avons ensuite choisi trois représentations optimisées du potentiel de Dudarev et Derlet pour pouvoir les comparer de façon plus détaillée à d'autres potentiels interatomique semi-empiriques récemment développés, en utilisant la théorie de la fonctionnelle de la densité et les résultats expérimentaux. Nous trouvons, pour les énergies de migration des défauts interstitiels une fourchette de 0.31 eV à 0.42 eV, à comparer à une valeur proche de 0.35 eV fournie par la théorie de la fonctionnelle de la densité et à une valeur expérimentale proche de 0.3 eV. Nous trouvons pour le coefficient de diffusion des défauts interstitiels à 600 K une plage de 1×10^{-6} cm^2/s à 10×10^{-6} cm^2/s, alors qu'à la température ambiante la variance s'étend sur trois ordres de grandeurs. Nous trouvons pour les énergies de migration des lacunes une fourchette de 0.85 eV à 0.94 eV, à comparer à une valeur proche de 0.65 eV obtenue par la théorie de la fonctionnelle de la densité. Les amas

constitués de défauts interstitiels parallèles sont orientés dans les directions ⟨110⟩ si le nombre des défauts composant le amas est inférieur à trois, tandis que les amas plus grands sont orientés de préférence dans les directions ⟨111⟩. L'entropie de formation d'un défaut interstitiel orienté selon ⟨110⟩ calculée par la méthode de l'intégration thermodynamique entre 300 K et 600 K se trouve dans le domaine de 0.28 k_B à 4.02 k_B. Tous les potentiels semi-empiriques rencontrent des problèmes quand on les applique à la structure CFC et aux mécanismes de migration de la dislocation vis. Par exemple, ces potentiels ne peuvent pas distinguer entre la phase CFC anti ferromagnétique, la phase CFC ferromagnétique à bas spin, et la phase CFC ferromagnétique à haut spin. Mais si on ne considère que le moment magnétique et le volume d'équilibre, alors la phase CFC ferromagnétique à haut spin est la plus proche de la phase CFC ferromagnétique des potentiels de Dudarev et Derlet. Pour finir, nous avons examiné les fondamentaux du mécanisme de migration de la dislocation vis avec un vecteur de Burgers 1/2[111] au zéro absolu, et sans aucune contrainte. Pour les potentiels présentant un coeur non dégénéré on a calculé le potentiel de Peierls dans la direction $[\overline{2}11]$ entre deux coeurs équivalents de la dislocation vis. Cela confirme l'existence d'un coeur stable de la dislocation, au milieu du chemin de migration, coeur qui n'a pas été observé par la théorie de la fonctionnelle de la densité. Nous en avons discuté les conséquences quant aux énergies de formation des décrochement.

Mots clef : fer, magnétisme, modèle de l'atome entouré, potentiels interatomique, dommage produit par les radiations, optimisation, constantes élastiques de troisième ordre, énergie libre de formation, défauts ponctuels, amas, coefficient de diffusion, coeur de la dislocation vis, potentiel de Peierls, décrochement, énergie de formation, volume de formations, énergie de migration, modèle de Suzuki et Takeuchi, modèle de Frenkel et Kontorova.

Table of Contents

List of Tables

List of Figures

Chapter 1

Introduction

The object of this work is a 'magnetic'[1] interatomic potential recently developed by Dudarev and Derlet [1]. The Dudarev-Derlet potential (DD potential) is a way to incorporate zero temperature magnetism in an embedded atom method formalism (EAM), which enables fast evaluation of forces for large scale molecular dynamics (MD) simulations[2]. The DD potential includes two sets of parametrization, one corresponding to the ferromagnetic phase, and one corresponding to the non-magnetic phase, which can then be fitted to properties obtained from spin-polarized or non spin-polarized density functional theory calculations, and where the parameters for the non-magnetic phase are obtained by setting to zero one of the parameters for the ferromagnetic phase. The properties which are mostly fitted to include the equilibrium lattice parameter, the second order elastic constants, the energy difference between the zero temperature phases, the point defect formation and migration energies, the cohesive energy or the surface energies, derived from experiments and/or theoretical calculations.

Two fits for iron of the DD potential, labeled CS1 and CS2 (where CS stands for Case Study), have been optimized to the zero temperature bcc and fcc phases, as well as to the formation energy of the vacancy and of the self-interstitials point defects [1] (see also errata in [3]). CS2 was the natural choice for subsequent work, as it could best reproduce the formation energy of the self-interstitials from spin-polarized density functional theory (DFT). In the same work, the embedding functional of the DD potential was derived using a combination of Stoner theory for itinerant band magnetism and Ginzburg-Landau theory for second order phase transitions. The optimization database includes the recent DFT result that the ground state self-interstitial is a $\langle 110 \rangle$ oriented dumbbell, with a formation energy

[1] The quotes are to avoid confusion with magnetic potentials in electrodynamics

[2] An alternative way to include magnetism in the EAM formalism can be found in [2], but the potential was neither fitted nor further developed.

Figure 1.1: Self-interstitials relaxed using CS2. Atoms are colored according to the formula of the magnetic moment in [6].

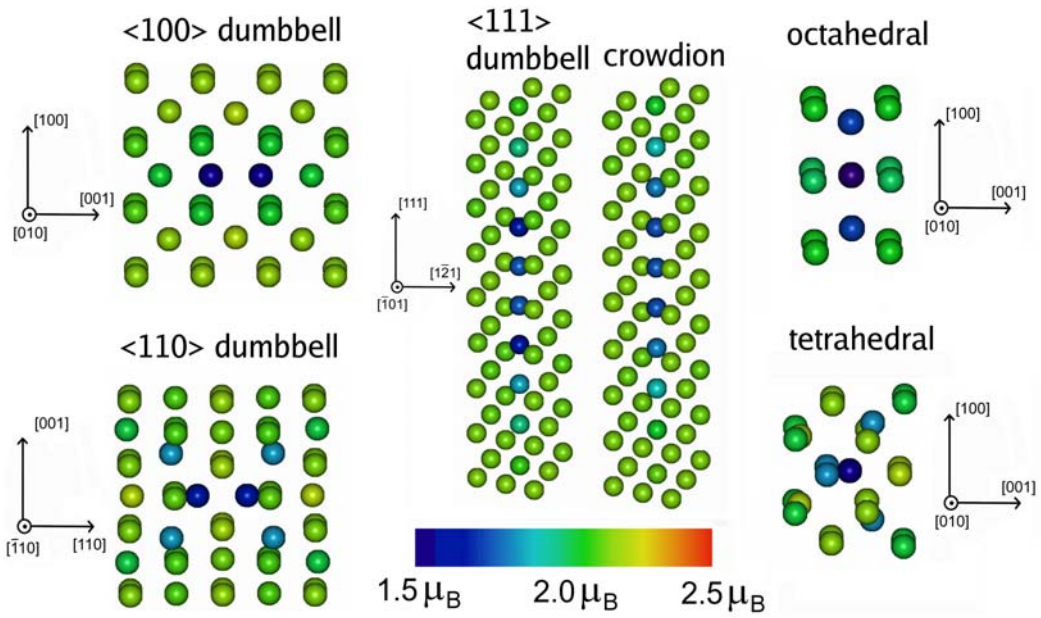

difference of 0.7 eV to the $\langle 111 \rangle$ orientation, which is in striking contrast to the other non-magnetic bcc transition metals, where the ground state is oriented along $\langle 111 \rangle$ [4]. The database has also included from DFT that the ferromagnetic bcc phase is the ground state, followed in order of increasing equilibrium energy by the ferromagnetic fcc phases[3], the nonmagnetic fcc phase and the nonmagnetic bcc phase, and that, while the ferromagnetic bcc is mechanically stable, the non-magnetic bcc is unstable with a negative value of the tetragonal shear modulus C', meaning that in some sense ferromagnetism helps stabilizing the bcc structure. On isotropic compression the energy difference between the ferromagnetic bcc and the nonmagnetic bcc decreases until magnetism is suppressed and a phase transition to closed-packed structures occurs [5].

A first extension of the DD potential was introduced in [6] and [7] with a simple formula to approximate the local magnetic moment on atoms, which allows to gain information not only about the non-magnetic and magnetic contributions to the energy, but also on the magnetic moment distribution. In the same work, this formula was then applied on bcc iron to get the magnetic moment distribution in self-interstitials, see figure 1.1, and in perfect prismatic dislocation loops with Burgers vectors $b = 1/2[111]$ and $b = [100]$. The same formula was employed to

[3]Anti-ferromagnetic, low spin ferromagnetic and high spin ferromagnetic

investigate the magnetic properties of pure amorphous iron [8], and of low index surfaces and nano clusters [9]. The (111) and (110) surface properties are in relative good agreement with DFT, but the (100) surface is not reproduced by any of the semi empirical potentials. The reason for this was argued to be that the (100) surface contains a strong peak of the surface electronic density of states near the Fermi energy, while the electronic density of states of the other low index surfaces does not differ significantly from the bulk. The properties of surfaces are of primary importance for radiation damage studies of voids.

The DD potential was then further extended to so called spin-lattice dynamics to treat magnetic temperature effects with two to six times the computational time [10], which was applied in [11] to the study of surface magnetism in iron thin films. The positions of the atoms and the directions of the atomic spins are treated as classical independent variables and the equations of motion for the spin directions are derived within a semi empirical classical approximation from a generalized Heisenberg Hamiltonian, where the exchange coupling function is represented by a pairwise function fitted to DFT data, and where the scalar part of the Hamiltonian is given by the zero temperature parametrization of the DD potential, that is the fit CS2. The local magnetic moment enters in the algorithm as an effective mass in the equations of motion for the spin directions. The extension of CS2 to spin-lattice dynamics enhances the thermal expansion coefficient, see figure 1.2, but also produces an inflection point (not shown in the figure) in the volume expansion curve at the Curie temperature which is not observed experimentally. The predicted value for the Curie temperature, defined in that work by the full loss of collinearity of the spin orientations, is in good agreement with experiments.

The DD potential and CS2 were developed within the european radiation damage community, which is interested in multiscale modeling of ferritic/martensitic stainless steels like EUROFER97 for fission and fusion reactor applications [12]. Molecular dynamics are used in this context to model bcc iron and some simple alloys, like Fe-Cr, Fe-He, Fe-C and Fe-Cr-C. Because of this, most of the applications of CS2 are related to radiation damage materials science, where semi empirical potentials are mostly used to investigate

- the structure of the primary damage by cascade simulations [13],
- the stability, mobility and interaction dynamics of small clusters of point defects for improvement of microstructural evolution models [14],
- and the interactions of dislocations with the defects produced during irradiation, like voids, He bubbles and dislocation loops [15].

Semi empirical potentials for radiation damage materials science are thus required to describe at best the point defect properties, like their formation energies and

Figure 1.2: Volume expansion of CS2 with spin-lattice dynamics from [10], or without spin-lattice dynamics as calculated in this work. The volume expansion curve of the Ackland-Mendelev potentials, also calculated in this work, does not include spin-lattice dynamics.

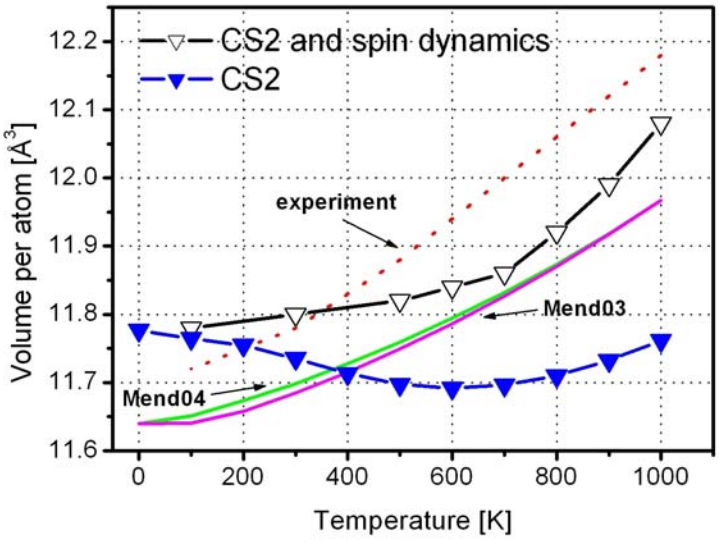

diffusivities. The past experimental controversy on the point defects properties in bcc iron [16] is only recently being resolved after DFT calculations became available of their formation and migration energies and of their binding energies with impurities [17]. As a consequence of this, only the most recently developed semi empirical potentials for bcc iron are consistent to the current understanding of the point defects formation and migration energies.

More specifically, all iron semi empirical potentials fitted before 2001 do not include that the formation energy difference between the $\langle 110 \rangle$ and the $\langle 111 \rangle$ oriented dumbbell is as big as 0.7 eV, although some of them can correctly reproduce that the dumbbell is oriented along $\langle 110 \rangle$ in the ground state. Because the ferromagnetic parametrization of CS2 may be seen as just any other EAM potential, it can be in principle compared to any semi empirical potential for bcc iron, but here we will use only recent EAM potentials fitted to DFT point defects properties to benchmark the new fits of the DD potential. These benchmark potentials are the potential number 2 in [18], which will be referred to as Mend03 in this thesis, and an improved version in [19], which will be referred to as Mend04. Another semi empirical potential that can be employed in large scale molecular dynamics simulations and fitted to DFT point defect properties is the analytic bond order potential for bcc iron, published in [20] and referred to as ABO in this work, which

is a Brenner type interatomic potential including angular terms and originally developed to treat sp-bonded materials. In the following, we will review publications where the fit CS2 has been compared to other semi empirical potentials or DFT.

In [21], CS2 was fitted in the intermediate interaction range[4] by requiring a smooth interpolation between the short range universal screened Coulomb potential and the equilibrium potential and a good match with experimental threshold displacement energies. It was then compared to Mend04 and ABO with respect to cascade damage simulations in bcc iron up to 20 keV. The scatter in the number of Frenkel pairs produced after thermalization of the cascades as a function of the primary knock on atom energy is strongly reduced among these potentials when compared to the scatter produced by older semi empirical potentials for iron. This is attributed to the fact that these semi empirical potentials provide an incorrect description of the self-interstitial formation energies as compared to more recent semi empirical potentials. The scatter in the fraction of point defects in clusters is however not reduced when compared to older semi empirical potentials.

The interaction of an edge dislocation with a nanometric void was fully characterized in [22] using CS2 and Mend03, where it was also found that CS2 has a negative thermal expansion coefficient.

Other work considered the formation energies of the bi-crystal symmetric grain boundaries $\Sigma3\{112\}$, $\Sigma3\{111\}$ and $\Sigma5\{013\}$ in bcc iron using CS2, Mend03, Mend04 and the Ackland potential [23]. The EAM potentials results are very similar to DFT.

Mend03, Mend04, CS2 and the Ackland potential have been compared with respect to self-interstitial clusters in bcc Fe [24]. The formation free entropy of small clusters of point defects oriented either along $\langle 100\rangle$, $\langle 110\rangle$ or $\langle 111\rangle$ was calculated by the quasi-harmonic approximation. It was found that CS2 gives negative formation entropies and that Mend03, Mend04 and CS2 all agree that small clusters with up to 4 or 6 self-interstitial atoms are more stable in the $\langle 110\rangle$ orientation than in the $\langle 111\rangle$ orientation. As the size increases, the $\langle 111\rangle$ orientation is always preferred. The formation energy of clusters with up to 1000 atoms was also investigated by static calculations. These are perfect prismatic dislocation loops with Burgers vector $b = 1/2[111]$ or $b = [100]$, which correspond to the experimentally observed interstitial dislocation loops in bcc iron. In the bcc lattice, a $\langle 111\rangle$ dumbbell is very similar to a crowdion, because in the $\langle 111\rangle$ direction atoms are

[4] In cascade damage simulations atoms are coming very close together and far from the equilibrium conditions for which the semi empirical potentials were fitted to. At very short interatomic distances, say smaller than ~ 1.5 Å in iron, the interaction is dominated by the universal screened Coulomb potential, whereas at distances bigger than ~ 2.3 Å the equilibrium potential can be used, but not much is known about the transition between these two regimes, which is called the intermediate interaction range.

close packed, and the point defect is spread over many atoms along this direction. A ⟨111⟩ dumbbell or crowdion can migrate very fast along this direction, with activation energies in the sub 0.1 eV range [25] corresponding to temperatures of few degrees Kelvin. A ⟨110⟩ dumbbell is inherently more sessile, and needs to rotate close to the ⟨111⟩ orientation to jump to a nearest neighbor site. This has important consequences on microstructural evolution models for bcc iron [14], as shown in object kinetic Monte Carlo simulations [26], because the ⟨111⟩ oriented dumbbells and its clusters migrate by fast one dimensional motion, in contrast with the three dimensional migration mechanism with much higher activation energy of the ⟨110⟩ dumbbell and its clusters.

The interaction of perfect prismatic dislocation loops with Burgers vector $b = 1/2[111]$ or $b = [100]$ with self-interstitial atoms was studied in [27] using CS2 and Mend04, and the reactions between pairs of $b = 1/2[111]$ interstitial dislocation loops in [28] using CS2 and Mend04. It was found that independent of the potential used, when two clusters of comparable size collide, a sessile metastable configuration consisting of non-parallel self-interstitial atoms is formed.

In [29] the elastic properties of the ⟨110⟩ dumbbell were investigated using CS2. It was found that the dependence of the second order elastic constants on defects concentrations is at odds with experiments.

In [30] the effect of temperature on the stability of dislocation loops in bcc iron was studied using anisotropic elasticity, and the CS2 and Mend04 potentials were used to estimate dislocation core parameters.

The formation energy of the mesoscopic circular $b = 1/2[111]$ and $b = [100]$ vacancy (closed, open, bubble) and interstitial loops, using almost exclusively CS2, is the subject of [31].

Other work where CS2 was employed is: radiation damage in nanocrystalline iron [32], atomistic kinetic Monte Carlo [33], positron annihilation at grain boundaries [34], Peierls stress for screw and edge dislocation [35] and stability of helium bubbles through the use of published Fe-He potentials [36]. Cascade damage simulations including the electron-phonon coupling have been performed using CS2 [37]. The number of simulated cascades is however not enough to draw any conclusions.

Another source for the present thesis is the work of Müller, Erhart and Albe [20]. After describing the fitting procedure of an analytic bond order potential for iron (ABO in this work) the optimal fit is extensively compared to some widely used EAM potentials, including CS2, Mend03 and DFT calculations. The focus is on phase properties, including bulk properties of the bcc, fcc, hcp, simple cubic and diamond structures. The CS2 potential is reported to give a negative thermal expansion coefficient at room temperature, which is linked to a negative pressure derivative of the bulk modulus. All the semi empirical potentials are found to overestimate the zero temperature equilibrium volume of the ferromagnetic fcc

phase. In addition, the ferromagnetic fcc phase of CS2 and of Mend03 is unstable up to the melting point. Other properties investigated of the bcc and fcc phases include melting temperature, phonon dispersion curves, surface energies, point defect formation and migration energies, and free energies. The formation volumes of the $\langle 110 \rangle$ self-interstitial dumbbell is found to be negative for CS2, at odds with the other semi-empirical potentials. In [20], the migration energies of point defects were determined by fitting the diffusion coefficient obtained in a dynamical calculation up to 2200 K for the vacancy and up to 1600 K for the dumbbell with a rather small bcc supercell, but no further details of the calculation method are given. The migration energies of both the vacancy and the stable self-interstitial so determined are found to be significantly underestimated with respect to the static calculation. For instance a value of 0.18 eV for the self-interstitial migration energy is given for the Mend03 potential, compared to a static calculation of 0.34 eV. This however contradicts results in [14], where static and dynamic estimates of the migration barrier are found to be in excellent agreement, with a value close to 0.3 eV.

To summarize, the work cited above revealed that

- CS2 shows anomalous anharmonic properties when compared to the other semi empirical potentials. For instance the quasi-harmonic approximation fails at very low temperatures, as shown in [38]. The most apparent effect is that the expansion coefficient is negative up to ~ 600 K. Related to this is a very low formation volume for the point defects. This is not the case for Mend04 and ABO. Although the inclusion of spin orientation degrees of freedom shifts the thermal expansion coefficient of CS2 up to positive values the comparison with experiments is still not satisfactory [10], see also figure 1.2.

- The core structure of the $b = 1/2[111]$ screw dislocation predicted by CS2 is at odds with DFT calculations [39]. This is also the case for ABO, but not for the Ackland-Mendelev potentials.

- The ferromagnetic fcc phase is unstable in molecular dynamics calculations up to the melting point [20]. This is also the case for the Ackland-Mendelev potentials, but not for ABO.

This work was partly funded by the European Fusion Development Agreement to further investigate these problems and to optimize the DD potential to molecular dynamic simulations of bcc iron, but excluding spin-lattice dynamics, with priority to those properties considered most relevant to radiation damage studies. In order of importance these are:

1. the point defects migration and formation energies,
2. the bulk properties of the bcc ferromagnetic phase, including anharmonic behavior,
3. the $b = 1/2[111]$ screw dislocation core structure and migration mechanism,
4. zero temperature magnetism in bcc iron.

The mobility of the $b = 1/2[111]$ screw dislocation is important in the study of the ductile to brittle transition temperature and magnetic effects are important when simulating iron and its alloys at high temperatures. We will thus mainly focus on the ferromagnetic bcc phase, although we will also discuss problems related to the description of the fcc phase.

The present thesis is organized as follows. In chapter 2 we discuss critically an appropriate fitting strategy. We start by the formalism of the semi empirical potentials considered in this work, that is the DD potential, the Ackland-Mendelev potentials and ABO. We will then rationalize the anomalous anharmonic behavior of CS2 in terms of third order elastic constants, which have been implemented in the optimization software. To fit to the correct core structure of the screw dislocation, we will develop and validate a method based on the Suzuki-Takeuchi model. We will then discuss the non-magnetic and ferromagnetic properties of the bcc and fcc phases and finally describe the optimization algorithm. Three representative fits, labeled CS3-00, CS3-30 and CS3-33 are then discussed in more detail in chapter 3 with respect to the bulk properties of the non-mangetic and ferromagnetic bcc and fcc phases and the static point defect properties, that is formation and migration energies, formation volumes and clustering of parallel self-interstitials. We then develop more complex methods to test and compare the new fits. These are a molecular dynamics calculation of the diffusion coefficient of the $\langle 110 \rangle$ dumbbell and a Monte Carlo calculation of the anharmonic contribution to the formation free energy of the $\langle 110 \rangle$ dumbbell. Table 1.1 shows a summary of the fits of the DD potential with the properties included in the optimization algorithm, some of which, however, could not be fitted. In chapter 4 we have also investigated some fundamental aspects of the mobility of the $b = 1/2[111]$ screw dislocation. Finally, we summarize the results in chapter 5.1 and give in the outlook some ideas for further research.

Table 1.1: Summary of the fits of the DD potential. The present work is referred to as 'version 2009'.

	version 2005	version 2009
fits	CS1, CS2	CS3-00, CS3-30, CS3-33
fit database	ferromagnetic, non-magnetic bcc and fcc	ferromagnetic, non-magnetic bcc and fcc
fit database	point defects	point defects
fit database		third order elastic constants
fit database		screw dislocation core

Chapter 2

Fitting strategy

2.1 Formalism of the semi empirical potentials

Over the years, many semi empirical[1] potentials for bcc iron have appeared in the literature, see [13, 40] and references therein. Among the oldest the pair potential of Johnson published in 1964 [41]. In a pair potential, the energy is a sum over functions which depend only on the distance between pairs of atoms. The total energy of atoms $1, 2, \ldots, N$ at positions $\vec{R}_1, \vec{R}_2, \ldots, \vec{R}_N$ can be written as

$$E(\vec{R}_1, \vec{R}_2, \ldots, \vec{R}_N) = \frac{1}{2} \sum_{\substack{i,j=1 \\ i \neq j}}^{N} V(r_{ij}), \tag{2.1}$$

where r_{ij} is the distance between atom i and j, and V is a short range function, that is it is non zero for a finite number of neighboring atoms only. Pair potentials suffer from some important limitations, for example the unrelaxed vacancy formation energy is equal to the cohesive energy, and at equilibrium zero pressure, any pair potential satisfies the Cauchy relation $K - 2/3C' = C_{44}$ between the anisotropic elastic constants, where K is the bulk modulus, C' the tetragonal shear modulus and C_{44} the rhombohedral shear modulus. Because the Cauchy relation is experimentally not satisfied by most of the transition metals, this was adjusted by adding to the pair potential a volume dependent term in the energy, which however makes it difficult to handle free surfaces and vacancies.

To overcome this problem, Daw and Baskes [42] (EAM) and Finnis and Sinclair [43] added to the pair potential an effective many body term, the so called embedding functional. This is a function of an additional pair function, the so

[1] semi indicates either that there exist some motivation for the functional form or that some properties are fitted to ab initio calculations.

called electronic density:

$$E(\vec{R}_1, \vec{R}_2, \ldots, \vec{R}_N) = \sum_{i=1}^{N} F(\rho_i) + \frac{1}{2} \sum_{\substack{i,j=1 \\ i \neq j}}^{N} V(r_{ij}), \tag{2.2}$$

where the electronic density on atom i is given by

$$\rho_i = \sum_{\substack{j=1,\ldots,N \\ j \neq i}} f(r_{ij}). \tag{2.3}$$

In the EAM formulation of Daw and Baskes, the embedding function F is determined from the equation of states, while Finnis and Sinclair assumed that the embedding function has a square root form,

$$F(\rho) = -A\sqrt{\rho}, \tag{2.4}$$

which can be motivated by a scalar second moment approximation of the electronic density of states within the tight binding model [44]. With these modifications it was then possible to accurately fit the second order elastic constants, overcoming the Cauchy pressure problem without adding any volume dependent term to the energy. The short range functions V and f are parameterized and fitted to basic material properties like phase structures, equilibrium lattice parameter and second order elastic constants. The fact that only short range interactions are taken into account makes any application of EAM potentials very efficient and easy to implement in parallel computing, allowing MD simulations with millions of atoms up to nanoseconds, but at the price of accuracy, because interactions in solids are actually long range. These functions are usually represented by splines, continuous at the cutoff radius beyond which the function value is set to zero.

Finnis and Sinclair included in their work [43] also a set of parameterizations for transition metals which are known in the literature as the Finnis-Sinclair potentials. The functions V and f are represented by simple polynomials with a cutoff between the second and third neighbor shell and they were fitted to the equilibrium lattice constant, elastic constants and cohesive energy. The Finnis-Sinclair potential for iron was the first EAM potential to be used in a simulation of a displacement cascade [45], and is up to now the most employed potential in cascade damage simulations, with over thirty publications including reviews [13]. An improved version of the Finnis-Sinclair potential for iron was published in 1997 [23] as the Fe-Fe part of a Fe-Cu potential, which is referred to in this work as the Ackland potential.

As already stated in the introduction, in 2001 DFT calculations confirmed the

experimental findings [16] that the lowest energy self-interstitial configuration in bcc iron is actually the $\langle 110 \rangle$ dumbbell [17], with a migration energy close to 0.3 eV [46], but all the potentials developed previously do not reproduce this property. Recent semi empirical potentials with improved point defects properties, and in this work a benchmark to the new fits of the DD potentials, are the Ackland-Mendelev potentials [18, 19] referred to as Mend03 and Mend04 in this work, the analytic bond order potential [20], referred to as ABO in this work, and the fit CS2 of the DD potential [1].

2.1.1 The Ackland-Mendelev potentials for bcc iron

Mend03 was the first published EAM potential for iron fitted to DFT point defect properties [18]. The embedding function is given by

$$F(\rho) = -\sqrt{\rho} + a_{F,2}^{\mathrm{M03}} \rho^2, \tag{2.5}$$

where $a_{F,2}^{\mathrm{M03}}$ is a fitting parameter. The function V was represented by a combination of third order splines and exponential functions at shorter range, and f by third order splines. Four sets of parameters for V and f were presented in [18], called potential number 1, 2, 3 and 4. The potential number 2, that is Mend03, reproduces at best the DFT point defect formation and migration energies. In the range between 0 K and 20 K, however, Mend03 has a negative thermal expansion coefficient, which led to the development of an improved version [19], referred to as Mend04 in this work, with the modified embedding function

$$F(\rho) = -\sqrt{\rho} + a_{F,2}^{\mathrm{M04}} \rho^2 + a_{F,4}^{\mathrm{M04}} \rho^4. \tag{2.6}$$

The representation of the model functions V and f is exactly the same as for Mend03, and also the parameters of Mend04 are close to Mend03.

The ground state configuration of the self-interstitial is a $\langle 110 \rangle$ oriented dumbbell, with a formation energy of 3.5 eV and a migration energy of 0.34 eV [14]. The vacancy has a formation energy of 1.7 eV with a migration energy of 0.67 eV, in rather good agreement with DFT. The Ackland-Mendelev potential was, up to the present thesis, the only known semi empirical potential for iron to give a non-degenerate core structure of the $b = 1/2[111]$ screw dislocation [47], in agreement with DFT. The Ackland-Mendelev potentials have a relatively long range of interaction: the cutoff radius of CS2 and ABO is, respectively, 4.3 Å, that is up to the third neighbor shell, and 3.35 Å, that is up to the second neighbor shell, while it is 5.3 Å for Mend03 and Mend04, that is up to the fifth neighbor shell. The way these potentials were constructed by fitting to liquid iron configurations from DFT is rather obscure and does not explain *why* Mend03 and Mend04 are so

successfull, which is a further motivation for the present work.

2.1.2 Analytic bond order potential for bcc iron

The analytic bond order potential was first proposed by Tersoff [48] to model silicon, carbon and germanium and later refined by Brenner [49] to model hydrocarbons and more generally multi component systems. The analytic bond order potentials have been then derived for the σ and π bond orders by a momentum expansion of the two-center, orthogonal tight-binding model [50]. They are thus best suited for the description of covalent sp-bonds. After application to many semiconductors, the Brenner potential formalism has been also applied to transition metals, including platinum and platinum-carbon [51] and bcc tungsten, tungsten carbide [52] and recently also bcc iron [20]. The authors give some motivation for applying a model originally developed for sp-bonds to transition metals, where the properties depend significantly on the d-band, based on the fact that a Brenner potential with no angular dependence is equivalent to an EAM potential. More generally, the difference between the EAM and Tersoff-Brenner potentials is that they can be derived from a *scalar* versus *matrix* second level recursion expansion of the two-center, orthogonal tight-binding model.

The analytic bond order potential for bcc iron (ABO in this work) is of the Brenner form, and the configurational energy of atoms $1, 2, \ldots, N$ at positions $\vec{R}_1, \vec{R}_2, \ldots, \vec{R}_N$ is given by

$$E(\vec{R}_1, \vec{R}_2, \ldots, \vec{R}_N) = \frac{1}{2} \sum_{\substack{i,j=1 \\ i \neq j}}^{N} f^c(r_{ij}) \left[V^R(r_{ij}) - \frac{b_{ij} + b_{ji}}{2} V^A(r_{ij}) \right], \tag{2.7}$$

with r_{ij} as before the distance between atom i and j. V^R and V^A are represented by exponential functions with four parameters and f^c is a cut-off function determined by two parameters, one of which is the interaction range. Finally, the angular dependent term is b_{ij} with four adjustable parameters, which is a function of *all* the angles θ_{ijk} between the bonds $i - j$ and $i - k$ for all atoms k within the interaction range of i. Only the cosinus of the angles enters in b_{ij},

$$\cos(\theta_{ijk}) = \frac{\left(\vec{R}_j - \vec{R}_i\right) \cdot \left(\vec{R}_k - \vec{R}_i\right)}{r_{ij} r_{ik}}. \tag{2.8}$$

More details about the formalism and the parameters of the analytic bond order iron potential as well as a detailed analysis of some basic properties and comparison with established EAM potentials (including CS2) can be found in [20].

ABO is defined by ten parameters, which is quite smaller than the number of parameters required in the Dudarev-Derlet or Ackland-Mendelev potentials for iron, typically from thirty to forty. This is done at the price of the complexity of the fitting procedure and of the implementation, plus a somewhat lower computational speed. ABO was fitted to DFT point defect formation energies and can reproduce that the $\langle 110 \rangle$ self-interstitial is the ground state self-interstitial, with a formation energy of 4.19 eV and a migration energy of $\sim$ 0.22 eV. The formation energy of the vacancy is 1.56 eV with a migration energy of 0.90 eV. The point defect properties are thus not as close to the DFT predictions as the Ackland-Mendelev potentials or CS2, because the priority in the fitting was given to phase properties, and in particular to the competition between the bcc and fcc phases. ABO was *directly* and successfully fitted to the α-γ-δ transition temperatures by adjusting the energy difference between the bcc and fcc phases at zero temperature. This *ad hoc* adjustment is needed because these transitions are driven by local magnetic moment fluctuations not yet explicitly included. There is thus at present no direct evidence that a Brenner type potential is significantly more successful in describing the many features of pure iron than a simpler EAM potential, because in principle the same method to get the transition temperatures right could be applied to any EAM potential.

2.1.3 The Dudarev-Derlet potential

The EAM density functional of the DD potential has been derived within the Stoner theory for itinerant electron band magnetism and using the Ginzburg-Landau theory for second order phase transitions, see an alternative derivation in appendix A. The embedding function is [1]

$$F(\rho) = -A\sqrt{\rho} - BM(\rho), \tag{2.9}$$

where A and B are positive parameters. The first term in (2.9) mimics a contribution from electrons in a non-magnetic band, that is with the same total number of spin up and down electrons, while the second term mimics the energy of band splitting. The magnetic part of the embedding function is

$$M(\rho) = \frac{1}{\ln 2}(1 - \sqrt{\rho}) \ln(2 - \rho)\Theta\,(1 - \rho) \tag{2.10}$$

where ρ is the relative electronic density and $\Theta(x)$ is the Heaviside function which is equal to zero for $x < 0$ and equal to one otherwise. This formalism thus explicitly includes the suppression of magnetism for $\rho > 1$, that is at high compressions.

A very simple expression for the local ferromagnetic moment on atom i has

been derived in [6]

$$\zeta_i = C\left(1-\sqrt{\frac{\rho_i}{\rho_c}}\right)^{\gamma}\Theta\left(1-\rho_i/\rho_c\right) \tag{2.11}$$

where C, ρ_c and γ are also model parameters fitted to the DFT magnetic moment distributions. These parameters have been fitted for CS2 to the bulk magnetic moment dependence on isotropic volume changes from DFT [6], where ρ_c was set to 1 for consistency with the interpretation of M as the magnetic contribution to the energy. We will develop here an alternative approach to fit these parameters, in such a way as to get a magnetic moment which can be compared between different fits of the DD potential, as explained in appendix A.

In the present work we do not employ the same parametrization of the model functions as for CS2, that is third order splines. Instead we parameterize the functions V and f with fifth order splines

$$V(r) = \sum_{n=1}^{N^V} V_n\left(r_n^V-r\right)^5 e^{-\lambda_V\left(r_n^V-r\right)}\Theta\left(r_n^V-r\right), \tag{2.12}$$

$$f(r) = \sum_{n=1}^{N^f} f_n\left(r_n^f-r\right)^5 e^{-\lambda_f\left(r_n^f-r\right)}\Theta\left(r_n^f-r\right). \tag{2.13}$$

In this way the model functions are continuous up to the fourth order, making it easier to fit the third order elastic constants. The fitting parameters r_V^n and r_f^n are the knot points; V_n and f_n the knot coefficients; N^V and N^f the number of knot points and the exponential factors λ_V and λ_f have been introduced to increase the fitting flexibility.

The parameters of the DD potential given in [1] and in tables 3.7, 3.8 and 3.9 correspond to the magnetic parametrization. The non-magnetic parametrization is obtained by setting B=0 in the magnetic parametrization, because of the interpretation of the term $M(\rho)$ as the magnetic part of the embedding function.

Note also that within the 'magnetic' interatomic potential formalism the cohesive energy and the energy per atom are different quantities. The cohesive energy is defined as the energy per atom needed to separate all the atoms from the condensed phase, and is given by

$$E_{\mathrm{coh}} = E_\infty - E_{\mathrm{bcc}} = -\left(E_{\mathrm{bcc}} + BM(0)\right) = -\left(E_{\mathrm{bcc}} + B\right) \tag{2.14}$$

where E_{bcc} is the energy per atom in the perfect bcc lattice at the equilibrium lattice constant and E_∞ is the energy per atom of non-interacting atoms, that is at a distance beyond the cutoff radius. While in Mend03, Mend04 and ABO E_∞ vanishes, in the 'magnetic' interatomic potentials it is equal to the magnetic part

of the energy functional evaluated at zero density and multiplied by the parameter B.

2.2 Anomalous anharmonicity of CS2

CS2 shows anomalous anharmonic properties when compared to the other semi empirical potentials, the most apparent effect is that the expansion coefficient is negative up to 600 K, see figure 1.2 on page 6, which is not the case for Mend04 and ABO, where the thermal expansion coefficient was also calculated by MD simulations using the Parrinello-Rahman barostat method [53] from 0 K to 100 K, see table 2.1 on page 25. In addition, in CS2 the quasi-harmonic approximation fails at very low temperatures, as shown in [38].

These semi empirical potentials are almost exclusively employed in classical molecular dynamics simulations, which is not very accurate at high temperatures, because it is essentially a classical method neglecting electronic and magnetic contributions, but it is also difficult to compare to low temperature experimental data, because below the Debye temperature quantum effects must be taken into account. What is needed to accurately fit semi empirical potentials is thus a classical extrapolation method which accounts for electronic and magnetic contributions, which would give the appropriate experimental value for a comparison at zero temperatures, but since this goes beyond the scope of this work, we apply a very simple *ad hoc* strategy instead. We observe that, in the experiment reported in [54], the true thermal expansion coefficient of pure iron shows a nearly perfect linear dependence in the temperature range between 300 K and 850 K, we thus choose to simply linearly extrapolate the experimental expansion coefficient from this range to 0 K, and obtain for the relative volume expansion coefficient α_{dyn}=2.8×10^{-5} 1/K, see table 2.1 on 25. For comparison, the experimental value at 600 K is α_{dyn}=4.2×10^{-5} 1/K, that is 50% higher than the linear extrapolation at 0 K, but in the source for the experimental data [54] it was not specified whether the experimental samples was a single crystal, so very likely this experimental value refers to a polycrystal.

All the semi-empirical potentials considered here have been fitted to essentially the same second order elastic constants, see table 2.1 on page 25. The vibrational thermal expansion coefficient can then be rationalized in terms of third order elastic constants, see [55]. In this work we employ the definition of Brugger [56] for the third order elastic constants

$$C_{\lambda\mu\nu} = m_0 \left.\frac{\partial^3 E}{\partial\eta_\lambda \partial\eta_\mu \partial\eta_\nu}\right|_{\eta=0}, \tag{2.15}$$

where m_0 is the mass density, E is the configurational energy and the derivatives are taken with respect to (homogeneous) Lagrangian strains in the usual contracted notation. Note that third order elastic constants are very sensitive on whether one considers Euler or Lagrange deformations. For a cubic system there exist six independent non zero third order elastic constants, in analogy with the case of second order elastic constants where this number is reduced to three, and it is possible to extract them by application of a set of six deformations, see for instance [57]. For each deformation, the strain parameter is varied from -1% to 1%; the energy curves so obtained are then fitted to fourth order polynomials and the third order elastic constants are extracted from the coefficients of the polynomials. The results are collected in table 2.1 on page 25. The third order elastic constants of all the semi-empirical potentials are negative, except C_{111} of CS2, which is positive and anomalously big. This is a clear indication that the anomalous behavior of the thermal expansion coefficient calculated by MD can be rationalized in terms of third order elastic constants. A direct comparison with the experimental third order elastic constants must be taken with care, because these are measured at room temperature and it is yet not possible to extrapolate these data to zero temperature, due to the lack of measurements of third order elastic constants at different temperatures.

Calculation of second and third order elastic constants using DFT have been performed using the Vienna Ab Initio Simulation package VASP in the projected augmented wave formalism. Exchange and correlation have been described within the generalized gradient approximation by the Perdew-Burke-Ernzerhof functional and the pseudopotential has been taken from the VASP library. The energy cutoff for the plane wave basis set has been set to 400 eV. Electronic density relaxations have been performed on primitive cells containing one atom with a convergence criteria of 1×10^{-4} eV, and the k-point sampling has been performed by a $35\times35\times35$ Gamma centered Monkhorst-Pack grid. To get an accurate total energy we have employed the tetrahedron method with Blöch corrections. The results are collected in table 2.1 on page 25.

In general, anisotropic elasticity theory is fairly complex and most of the results and expressions in dislocation theory, including dislocation-dislocation and defect-dislocation interactions, have been derived within isotropic elasticity. We will now consider, for simplicity, some third order effects on isotropic elasticity, that can be related to third order elastic constants. The isotropic bulk modulus K, the shear modulus μ and the anisotropy factor H have been calculated by Voigt averages of the anisotropic second order elastic constants, see [58]. This corresponds roughly to averaging the single crystal elastic properties for a polycrystalline sample. Note that the DFT isotropic bulk modulus K and shear modulus μ, as calculated by Voigt averages, are very close to experiments, but even if the anisotropy factor is

underestimated by as much as 50%, the effect of this on results of DFT simulations has, to our knowledge, never been investigated. A simple relation to third order elastic constants is given by the change of the isotropic elastic constants on volume changes [59]

$$V\frac{\partial K}{\partial V} \simeq \frac{1}{9}\left(C_{111}+6C_{112}+2C_{123}\right) \tag{2.16}$$

$$V\frac{\partial \mu}{\partial V} \simeq K+\frac{1}{3}\mu+\frac{1}{15}\left(3C_{144}+6C_{166}+C_{111}-C_{123}\right), \tag{2.17}$$

and the values of these derivatives are also collected in table 2.1 on page 25. A comparison with experimental data is not straightforward, as third order elastic constants refer to room temperature, while the calculations are at zero temperature. We just note again that the derivatives of the bulk and shear modulus predicted by CS2 are big compared to the other interatomic potentials. The dependence of the isotropic elastic constants on volume changes is also shown in figure 2.1 and compares well with the derivatives deduced from equations (2.16) and (2.17). Figure 2.1 also reveals steep slope discontinuities of both the bulk and shear modulus for CS2, one of which exactly located at the equilibrium volume per atom, and an instability at higher compressions, which have been produced by the use of third order splines to parameterize the model functions. These discontinuities are additional sources of anharmonicity. The formation volumes of the $\langle 110\rangle$ self-interstitial and of the vacancy as predicted by CS2 are also low when compared to Mend04 and ABO, see table 3.2 on page 41. This can also be intuitively related to the anomalous third order elastic constants, as they impact the derivatives of the elastic constants on compression.

On the basis of a continuum model the thermal expansion of a solid can be calculated from third order elastic constants within standard Debye theory by assuming linear dispersion of phonons, see [55]. In [55] it was also shown that the thermal expansion coefficient calculated from third order elastic constants is very close to the experimental coefficient. Since numerical techniques are required to relate exactly the expansion coefficient to the third order elastic constants, we just derive here a simplified analytic expression for the case of isotropic solids. As explained in [55], the thermal expansion coefficient is given by

$$\alpha = \gamma\chi_T C_V/V \tag{2.18}$$

where γ is the Grüneisen parameter, $\chi_T = -\frac{1}{V}\frac{1}{K}$ is the isothermal compressibility, C_V is the specific heat at constant volume and V is the volume of the system. In the high temperature harmonic and classical limit, the specific heat from atomic vibrational degrees of freedom is C_V=$3k_B$ where k_B is the Boltzmann constant. In

Figure 2.1: Isotropic bulk modulus K and shear modulus μ in GPa of the ferromagnetic bcc lattice as a function of the volume per atom in Å^3. The semi empirical potentials are compared to experimental data at room temperature from [60] and zero temperature DFT calculations from [61].

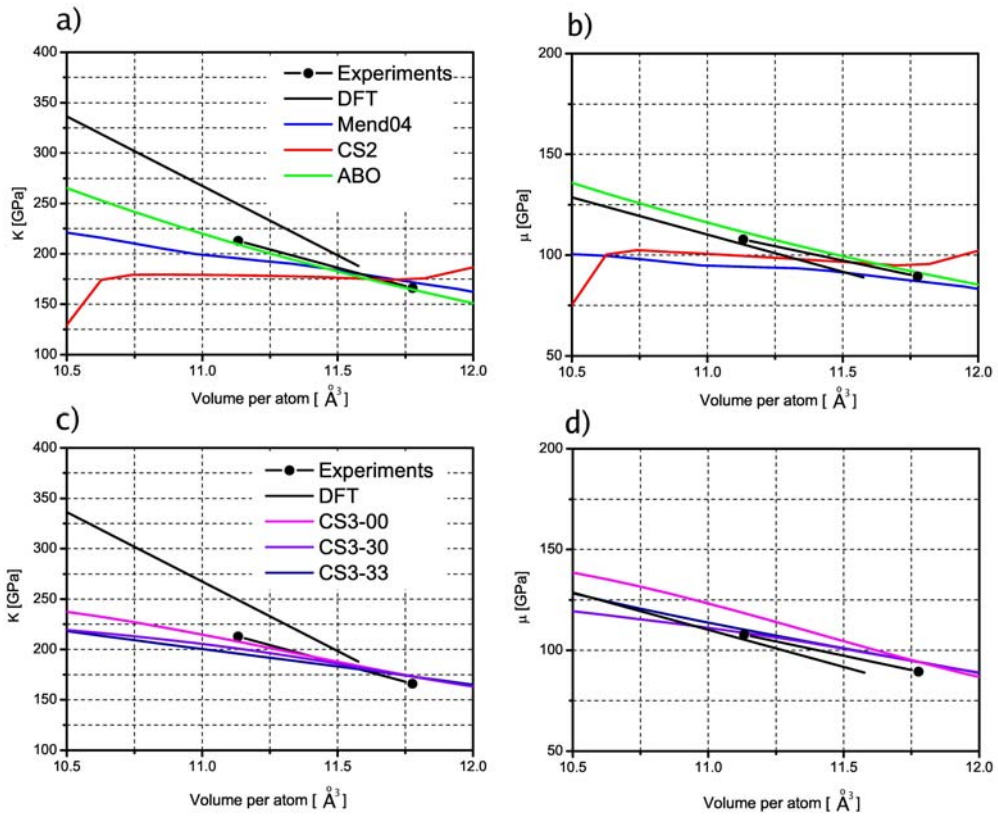

the high temperature limit the Grüneisen parameter γ can then be written as

$$\gamma = \frac{1}{3N} \sum_{q,p} \gamma_{q,p} \tag{2.19}$$

where

$$\gamma_{q,p} = \frac{1}{3} - \left(\frac{\partial \ln c_{q,p}}{\partial \ln V} \right), \tag{2.20}$$

p is the polarization of the $q = 1, \ldots, N$ modes and $c_{q,p}$ is the sound velocity of the (q, p) mode. By assuming an isotropic medium

$$c_{q,1} = c_L \tag{2.21}$$
$$c_{q,2} = c_T \tag{2.22}$$
$$c_{q,3} = c_T \tag{2.23}$$

where c_T and c_V are respectively the transverse and longitudinal sound velocities, and thus using the previous equations

$$\alpha_{\text{iso}} = \frac{k_B}{VK} \left(1 - 2\frac{V}{c_T}\frac{\partial c_T}{\partial V} - \frac{V}{c_L}\frac{\partial c_L}{\partial V} \right) \tag{2.24}$$

where V is the volume of the system. The isotropic sound velocities are related to the isotropic elastic constants by

$$c_L = \sqrt{\frac{K + \frac{4}{3}\mu}{m_0}}, \tag{2.25}$$
$$c_T = \sqrt{\frac{\mu}{m_0}}. \tag{2.26}$$

We have then calculated the expansion coefficient as given by the above equations using the volume derivatives of the isotropic elastic constants in table 2.1 on page 25. Comparing this value derived within isotropic theory, and the expansion coefficient obtained from low temperature MD, we see that for the EAM potentials the contribution for the neglected anisotropy is approximately -1$\times 10^{-5}$ 1/K, which in the case of CS2 is however small enough to explain its negative value.

To conclude we see that the present simplified analysis of the interatomic potentials in terms of third order elastic constants and isotropic elasticity is sufficient to rationalize the anomalous behavior of CS2 regarding the thermal expansion coefficient, the formation volumes of point defects and the failure of the quasi-harmonic approximation.

Table 2.1: Bulk properties of the ferromagnetic bcc lattice. The equilibrium lattice constant a is given in Å. The isotropic bulk modulus K and shear modulus μ as well as the anisotropic factor H and the third order elastic constants C_{ijk} are given in GPa. The volume derivatives of the isotropic elastic constants have been calculated from (2.16) and (2.17) using data from this table. The volume expansion coefficient α is given in units of 1×10^{-5}. It represents the relative volume change per degree Kelvin and was estimated both by a NPT molecular dynamic simulation at zero pressure up to 100 K (dynamical) and by the isotropic elastic approximation (2.24).

	Exp.	VASP	Mend04	ABO	CS2	CS3-00	CS3-30	CS3-33
a	2.855[a]	2.8340	2.8533	2.8603	2.8655	2.8677	2.8665	2.8665
K	173[b]	178	178	169	173	173	173	173
μ	94[b]	83	89	92	94	94	94	94
H	137[b]	64	134	169	140	140	140	140
C_{111}	-2876[c]	-3290	-245	-2070	3500	-1760	-1600	-1625
C_{112}	-542[c]	-1230	-880	-935	-470	-720	-700	-570
C_{144}	-747[c]	-480	-145	-290	-420	-995	-780	-780
C_{166}	-869[c]	-870	-670	-670	-455	-650	-435	-435
C_{123}	-533[c]	-1340	-825	-805	-830	-275	-240	-130
C_{456}	-557[c]	-530	-255	-485	-630	-740	-520	-510
$\frac{V}{K}\frac{\partial K}{\partial V}$	-4.6	-8.3	-4.5	-6.1	-0.6	-4.3	-4.0	-3.4
$\frac{V}{\mu}\frac{\partial \mu}{\partial V}$	-4.7	-4.4	-0.6	-2.3	2.4	-3.8	-2.3	-2.4
α_{dyn}	2.8[a]		1.0	0.6[d]	-1.0	3.5	2.0	2.4
α_{iso}	5.5	6.0	2.0	3.9	-1.2	4.6	3.3	3.3

[a] linear extrapolation at 0 K from data in [54]
[b] linear extrapolation at 0 K from data in [62]
[c] room temperature data from [56]
[d] value taken from [20]

2.3 Core properties of the $b = 1/2\,[111]$ screw dislocation.

For a more detailed explanation of the core properties of the screw dislocation, and of the method used to control these properties in the optimization algorithm, we refer the reader to chapter 4, the goal here is just to summarize the method we have employed to control the core structure during the optimization.

To fit the core properties of the $b = 1/2\,[111]$ screw dislocation we employ a recent development of the multi-string rigid Frenkel-Kontorova model, see [63]. In this model one projects the perfect bcc lattice onto the $\{111\}$ plane. Every point in the two dimensional projection represents an infinite string (or column) of atoms in the [111] direction. The strings are allowed to move up and down along the direction perpendicular to the plane, but not in the plane itself; the strings themselves are rigid, that is atoms in a column are kept fixed relative to each other. By appropriate displacement of the strings it is then possible, for instance, to create a degenerate or a non-degenerate screw dislocation core. The interaction law between strings up to the third nearest neighbor string is derived by rigidly moving one or more strings, and by calculating the unrelaxed energy of the corresponding three dimensional periodic configuration, employing any model for interatomic interactions, as for instance DFT, Tight Binding or EAM. For short range EAM potentials, extending up to the second nearest neighbor in the perfect bcc lattice, or with a very small component beyond the second nearest neighbor, the relevant part of the string interaction is given by the nearest neighbor string interaction [63]. In this case, which is also the case of the semi-empirical potentials considered here, the interaction law between strings can be derived by just moving *one* string of atoms, so called single-string Frenkel-Kontorova model or Suzuki-Takeuchi model. We call the unrelaxed energy as a function of the string displacement the *single string potential*, which we denote $\sigma(d)$, where d is the displacement of the string in units of the periodic distance between two (111) planes $a_{111} = b = \sqrt{3}/2a$. We also show in chapter 4 that there is a correlation between the shape of the single string potential and the ground state core structure of the screw dislocation. For this reason, we have included the single string potential from DFT in the optimization algorithm. In figure 2.2 we show the single string potentials of the semi empirical potentials and of DFT.

2.4 Ferromagnetic properties

DFT within the generalized gradient approximation predicts that, at zero temperature, the ferromagnetic bcc phase is the ground state, followed in order of

Figure 2.2: Sting potential. It is obtained by displacing a [111] row of atoms along the [111] direction and by calculating the unrelaxed energy as a function of the row (or string) displacement. We denote it by $\sigma(d)$ and measure it in units of eV per length of the row, where d is the displacement of the string in units of the Burgers vector $b = (\sqrt{3}/2)a$. The DFT curve is taken from [64].

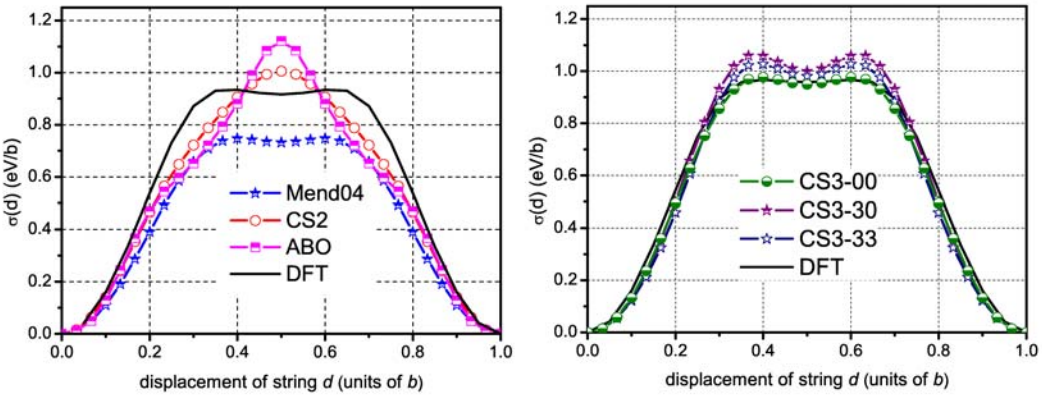

increasing energy by the anti-ferromagnetic fcc, the low-spin ferromagnetic fcc, the high-spin ferromangetic fcc, the nonmagnetic fcc and the nonmagnetic bcc [5]. The ferromagnetic bcc is mechanically stable while the nonmagnetic bcc is unstable with a negative value of the tetragonal shear modulus C'. On isotropic compression the energy difference between the ferromagnetic bcc and the nonmagnetic bcc decreases and a phase transition to closed-packed structures occurs, see figure 3.3 (b) on page 37.

It is well known that a second-moment approximation is not sufficient to describe the competition between the bcc and the close packed fcc and hcp symmetries in transition metals [65]. To pick up the shape changes of the DOS from the bcc to a close packed phase it is necessary to include at least the fourth moment contribution, which requires summation over four body terms [66]. We thus don't expect an accurate description of *both* the fcc and bcc phases, a very small weight is therefore given within the optimization algorithm to the bulk ferromagnetic and non-magnetic fcc properties. It is also not possible, within the present 'magnetic' interatomic potential formalism, to distinguish the low-spin ferromagnetic fcc phase from the high-spin ferromagnetic fcc phase. The only obvious requirement we set is that the ferromagnetic bcc be lower in energy than both the ferromagnetic and non-magnetic fcc.

We note here that the ABO potential was fitted directly to the α-γ-δ transitions in iron by adjusting the energy difference between the bcc and fcc phases. This is a trick to compensate for the missing spin contributions to the free energy, as stated by the developers of ABO in [20]. Because the DD potential can be extended to

include spin directions [10], and the interest is here focused on defect properties in the ferromagnetic bcc, we do not make here any *ad hoc* adjustment.

The only property which can be rigorously derived within the 'magnetic' interatomic potential formalism is the energy difference between the ferromagnetic and non-magnetic bcc on isotropic compressions, where the nonmagnetic phases are obtained by setting the parameter B in (2.2) equal to zero. We nevertheless also tried to optimize the value of

$$\Delta C' = C'_{\rm fm} - C'_{\rm nm}, \tag{2.27}$$

that is the difference in tetragonal shear modulus between the ferromagnetic and non-magnetic bcc phase, to the DFT value, see table 3.1 on page 38. A positive value of $\Delta C'$ means that the magnetic functional effectively helps stabilize the ferromagnetic bcc lattice. We will see later however that the fitting flexibility of the self-interstitial is strongly reduced by too much constraining $\Delta C'$ to positive values.

We have deliberately omitted the cohesive energy from the optimization algorithm. Its value has no effect on bulk simulations, as for instance displacement cascades simulations of neutron damage. Moreover, the energetics of free iron atoms are governed by orbital magnetism and Hund rules, while the 'magnetic' interatomic potential is an analytical model for itinerant band magnetism. Also note that in principle the cohesive energy can be corrected by modifying the low density limit of the magnetic embedding function.

Formation energies and diffusivities of self-interstitial, vacancies and clusters of them are of primary interest in radiation damage studies. DFT predicts that in all the non-magnetic bcc transition metals the $\langle 111 \rangle$ dumbbell has the lowest formation energy with migration barriers in the sub 0.1 eV range. This is in contrast with iron where the $\langle 110 \rangle$ dumbbell has ~ 0.7 eV lower formation energy than the $\langle 111 \rangle$ dumbbell [4]. DFT treats ferromagnetism as a local exchange interaction between spin up and down valence electrons and predicts that the local magnetic moment at the core of (all) the self-interstitial point defects is strongly reduced, see table 3.6 on page 65 for the specific case of the $\langle 110 \rangle$ dumbbell, for the other orientations, see [17]. This suggests that the differences in the formation energies between the $\langle 110 \rangle$ and the $\langle 111 \rangle$ self-interstitial dumbbell in iron and thus the migration energy barrier may be related to itinerant electron magnetism. The connection of ferromagnetism to point defect properties is yet not clear, since the Tight Binding Bond Stoner Model, which was not optimized to the self-interstitial formation energies, but can reproduce the local ferromagnetic moment in the core of the dumbbell, and qualitatively also the bulk properties of the non-magnetic, ferromagnetic and anti-ferromagnetic bcc, fcc and hcp phases, predicts a formation

energy difference of only ~ 0.3 eV between the $\langle 110 \rangle$ and the $\langle 111 \rangle$ dumbbells [67].

2.5 Optimization algorithm

We have optimized the fitting parameters of the model functions (2.13) and (2.12) as follows. The model functions are restricted to be short range including up to the second or third neighbors shells in the ferromagnetic bcc; furthermore V is allowed to have at most one local minimum and f is always restricted to be monotonically decreasing and positive, because of its interpretation as the contribution of a spherical inter atomic bond to the local electronic density. The electronic density parameters A and B are restricted to be positive.

Two consecutive simulated annealing and one run of the downhill non-linear simplex algorithm are employed to optimize some properties not involving lattice relaxations[2], that is the experimental third order elastic constants, see table 2.1 on page 25, the unrelaxed vacancy formation energy[3], the single string potential, see chapter 4, as well as the bulk properties of the ferromagnetic and nonmagnetic bcc and fcc, where the nonmagnetic phase is obtained by setting B=0 in (2.2) on page 14. The value of the fitted properties is the same as in [1], except for the third order elastic constants which were not included in the objective function of the CS2 fit.

Because of the complexity of the optimization we have performed systematic fits. For a particular choice of the objective function weights, we vary the cut off radius of V from 3.0 Å to 4.7 Å and the cut off radius of f from 3.0 Å to 4.0 Å in steps of 0.1 Å. The minimum knot point was set to 2.6 Å for both V and f and the knot points were distributed uniformly up to the cutoff. The number of knot points for both V and f was set to 5, 6, 7 and 8. The equilibrium lattice constant and second order elastic constants of the ferromagnetic bcc were solved exactly within the optimization algorithm thus reducing the number of free fitting parameters by four. Penalty functions were applied to third order elastic constants to constrain them within 50% of the experimental value. Fitting to third order elastic constants *exactly* results in too great a constraint on the model.

We then relax all the self-interstitials and correct anomalies in the short range until they are stable by adding a repulsive knot at 2.5 Å in V. This does not affect the bulk properties or the vacancy formation energy and prevents the relaxed dumbbell atoms to come too close to each other. Indeed if the short range

[2]Relaxations are just too slow to be implemented in the first stage of the optimization

[3]In general, the relaxed vacancy formation energy is smaller that the unrelaxed one, but anyhow not significantly different, which is on the other hand the case for the self-interstitials.

repulsion is too small, undesirable metastable configurations with the same orientation may occur where the dumbbell atoms are separated by less than 1 Å. From experience in the fitting we have noted that modifying this repulsive knot has the effect to change the relative formation energy of the dumbbell atoms. The smaller the repulsions, the smaller the distance between the dumbbell atoms, and the smaller the energy difference between the orientations. A higher repulsion increases the distance between the dumbbell atoms and also the energy difference between dumbbell orientations, but at the same time also the formation energies are increasing.

In the first half of the fits (PD_1) we apply penalty functions to $\Delta C'$ in (2.27) on page 28. We try to fit it by constraining systematically its value to at least 30, in a first trial, and then to at least 50, 70, 90 and 110 GPa in subsequent trials. The weights on the third order elastic constants have been also varied. In the second half of the fits (PD_2) we have included the value of the bulk modulus on isotropic compressions at a volume per atom of ~ 9.5 Å^3, setting its value to 100, 200, 300 and 400 GPa in subsequent trials. Fits in PD_2 have been fitted to the single string potential given by DFT, to be able to reproduce the correct core properties of the $b = 1/2[111]$ screw dislocation, but not to $\Delta C'$. Fits in PD_1 have not been optimized to the single string potential given by DFT.

To filter through we select fits with vacancy formation energies between 1.6 eV and 2.3 eV and an energy difference between the equilibrium ferromagnetic bcc and the ferromagnetic and non-magnetic fcc of at least 0.03 eV per atom; we refer to this first selection as BS_1 and BS_2, respectively obtained by filtering PD_1 and PD_2. We have then further reduced BS_1 and BS_2 by considering only fits with an energy difference between the equilibrium ferromagnetic bcc and fcc of at least 0.1 eV per atom and we refer to this as FCC_1 and FCC_2.

We can not fit $\Delta C'$ to the DFT value without other properties being too much compromised. The most serious is that the relative formation energies between the $\langle 110 \rangle$ and the $\langle 111 \rangle$ dumbbell are then restricted to a maximum energy difference of approximately 0.3 eV, see figure 2.3. This figure shows frequency counts of the formation energy difference between the $\langle 110 \rangle$ and the $\langle 111 \rangle$ dumbbell for all the fits generated within the optimization algorithm. The formation energies have been determined by relaxing the self-interstitial using all the potentials in the fit databases BS_1, BS_2. A negative value for the energy difference in this curve means that the $\langle 110 \rangle$ dumbbell forms with lower energy than the $\langle 111 \rangle$ dumbbell. This figure also shows that by selecting potentials with an energy difference between the bcc and the fcc phases of less than 0.1 eV/atom, that is neither in FCC_1 nor in FCC_2, the energy difference between the dumbbells is also restricted.

We have thus selected fits from FCC_2 by requiring a formation energy difference between the $\langle 110 \rangle$ and the $\langle 111 \rangle$ dumbbells of at least 0.4 eV, as well as a positive

Figure 2.3: Frequency counts of the formation energy difference between the ⟨110⟩ and the ⟨111⟩ dumbbell for all the fits in the BS database generated within the optimization algorithm. A negative value for the energy difference in this curve means that the ⟨110⟩ dumbbell forms with lower energy than the ⟨111⟩ dumbbell. The FCC database is obtained by selecting fits from the BS database with an energy difference between the ferromagnetic bcc and fcc phases of at least 0.1 eV/atom. As explained in the text, BS_1 refers to fits with a local minima in the model function V, whereas BS_2 refers to fits with a purely repulsive function V.

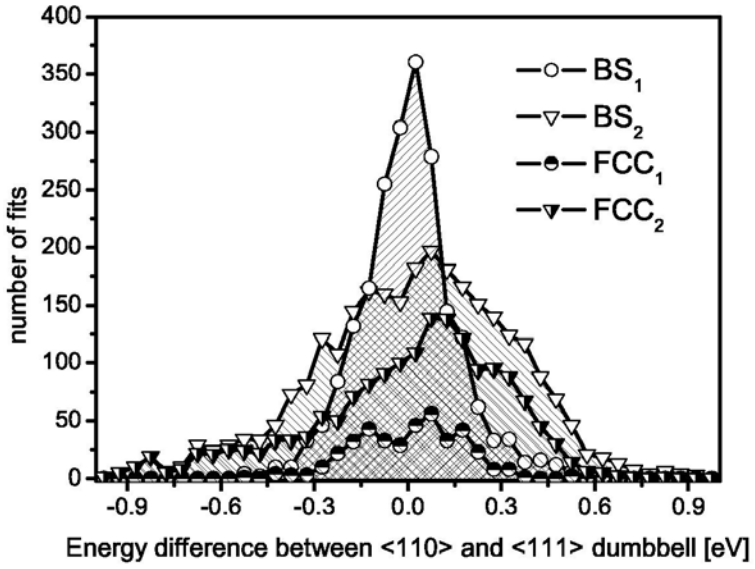

curvature midway in the single string potential. As will be shown later on in chapter 4, a positive curvature in the single string potential favors a non-degenerate ground state core structure for the screw dislocation. Since many potentials satisfy these criteria, we have calculated by the nudged elastic band method (NEB) the Peierls Barrier for migration of the screw dislocation and the migration energy of the vacancy and ⟨110⟩ self-interstitial of *all* the fits, and from this selected three representative potentials to be discussed in more detail in the following chapter.

The fits in database PD_1 have been also employed in [64] to demonstrate that, in the case of second-moment potentials, there is a strong correlation between the shape of the single string potential and the core structure of the $b = 1/2\,[111]$ screw dislocation. A similar proof will be given later at the end of chapter 4.

Beware that although this chapter is rather short and the optimization process may seem at a first glance rather simple, it is actually a formidable task and a great part of this thesis, almost one year of fitting. The modification of the optimization software, for instance to include third order elastic constants or to

control the shape of the model functions, is not easy. Moreover, the Fortran code employed for CS2 was written to get a so called proof of principle potential, not really a true universal optimization, which is needed to compete with the very accurate benchmark potentials for iron of the last generation. For instance, the previous fitting strategy did not include splitting of the optimization jobs on cluster computers, but fits were generated on a single processor in an almost interactive way. Thus a great part of this work was devoted to software development to implement a strategy to split jobs on cluster computers and to build a database to collect their properties and analyze them. To get the three optimal fits required the generation of something like 10'000 accepted fits corresponding to weeks of computing on the public PSI cluster, and the selection of the optimal fits was actually the result of a long error and trial process, combined with an extensive literature search for comparison with experiments or other theoretical methods.

Chapter 3

Detailed properties of optimized fits

We refer to the new optimized fits of the 'magnetic' interatomic potential as CS3-00, CS3-30 and CS3-33. The parametrization of these potentials is given in table 3.7, table 3.8 and table 3.9 at pages 67-69, and the parameters for the local magnetic moment, see (2.11) on page 18, are in table 3.5 at page 63. CS3-00 and CS3-30 have been also published in [38].

Figure 3.1 shows the model functions of the EAM potentials. To make the density function of Mend04 compatible with the relative electronic density of the DD potentials, we have divided it by 40 so as to scale the relative electronic density per atom of the bcc lattice to 1.0 at a volume per atom of 9.0 Å^3, which roughly corresponds to the volume at which magnetism should be suppressed. Except CS2 which has a deep local minima in V, the other EAM potentials have very similar model functions, although Mend04 features an additional attractive-repulsive part close to the third nearest neighbor of the bcc lattice and a longer range of interaction extending up to the fifth nearest neighbor.

3.1 Bulk properties

The bulk equilibrium properties of the ferromagnetic bcc phase are summarized in table 2.1 on page 25. The second order elastic constants are essentially the same for all the potentials, the third order elastic constants are all negative and the thermal expansion coefficient is now positive for CS3-00, CS3-30 and CS3-33, see figure 3.2. Note that the third order elastic constants of the CS3 potentials are very similar, although this was not intentional, since the selection of the fits was based exclusively on the point defect properties, the string potential, the Peierls barrier and the energy difference between the ferromagnetic bcc and the ferromagnetic fcc

Figure 3.1: Model functions of the EAM potentials. The figure shows on the left the pair potential $V(r)$ and on the right the density funcion $f(r)$, where r is in Å.

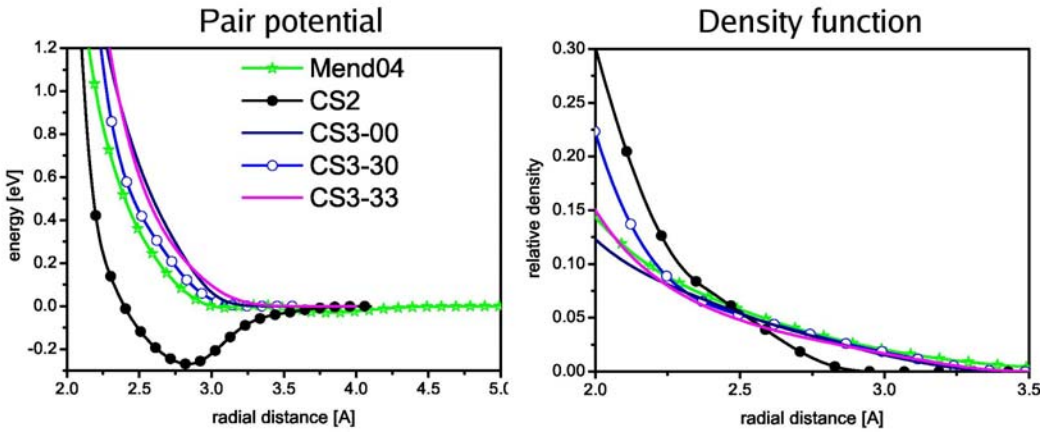

phases. The bulk properties of the non-magnetic and ferromagnetic bcc and fcc phases are summarized in table 3.1 on page 38, and figure 3.3 on page 37.

We will now refer to table 3.1 on page 38 in the following discussion.

CS2 underestimates the cohesive energy (2.14) and the CS3 potentials overestimate the cohesive energy, where the error is of the order of 10% to 50% in the worst case. Given the extreme simplicity of the 'magnetic' interatomic potential formalism this is actually not so bad. In principle, this could be corrected by modifying the low density limit of the magnetic part of the embedding function, see also the discussion in appendix A.

The energy difference between the non-magnetic and the ferromagnetic bcc could be fitted with an error of 20% to 50%, although the equilibrium volume of the non-magnetic bcc is generally underestimated, where the worst agreement in terms of volume per atom is for CS3-33 and the best for CS2. None of the potentials could anyhow come close to the DFT prediction that C' is as low as -110 GPa in the non-magnetic bcc phase, but CS2 at least leads to a negative value of C' in the non-magnetic bcc phase. For the CS3 potentials, however, the non-magnetic bcc is mechanically stable at zero temperature, but note again that the fitting of this properties was abandoned at the benefit of the defect properties in the ferromagnetic bcc lattice.

A direct comparison of the fcc phase with DFT is rather problematic, since the semi-empirical potentials give only one fcc phase, with the exception of the 'magnetic' interatomic potential which also gives a non-magnetic fcc phase obtained by setting B=0 in (2.9) on page 17. Even the DD potential is at present unable to distinguish between the anti-ferromagnetic, low spin ferromagnetic and high spin ferromagnetic fcc phases encountered in DFT, and gives only one ferromagnetic

Figure 3.2: Volume expansion curves without spin-lattice dynamics of the new fits, as calculated in the present work using MD.

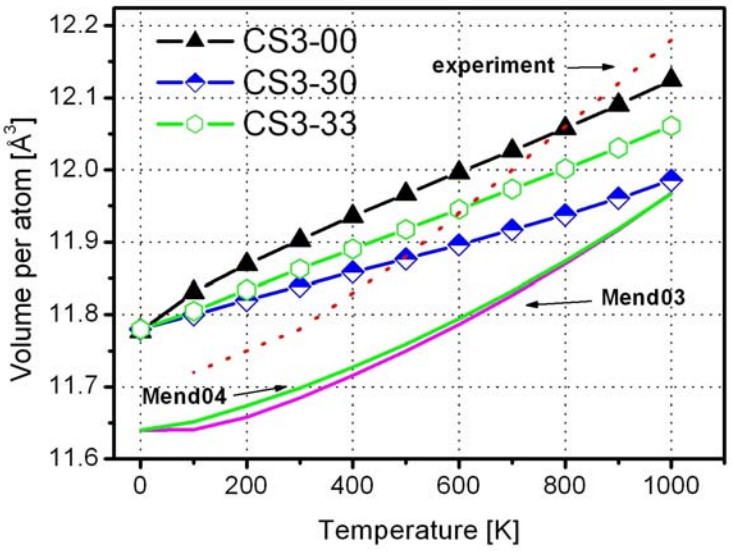

and one nonmagnetic phase, although when considering the equilibrium ferromagnetic moment and the equilibrium volume per atom of the ferromagnetic fcc phase, these are closer to the DFT high spin ferromagnetic fcc phase, see figure 3.3 on page 37 and table 3.1 on page 38. The CS3 potentials significantly overestimate the equilibrium energy and underestimate the equilibrium volume of the non-magnetic fcc. Moreover, the nonmagnetic fcc is, contrary to DFT, mechanically unstable with a negative C', see table 3.1 on page 38.

DFT gives a very small energy difference between the non-magnetic, antiferromagnetic, low spin ferromagnetic and high spin ferromagnetic fcc phases, when compared to the energy difference between the non-magnetic and ferromagnetic bcc phase, see figure 3.3 (b). The new fits fail to reproduce this feature, and give an energy difference between the non-magnetic and ferromagnetic fcc phases of the same order as the energy difference between the bcc phases. We attribute this to a deficiency of the second-moment approximation to resolve the shape change of the electronic density of states for different lattice structures, which is essential to determine an analytical solution within the Stoner Theory for itinerant band magnetism. For the DD potential, a parabolic shape with a width related to the second moment of the density of states was assumed. A change in higher moments of the density of states, such as the change from bcc to fcc, is however not included in the parabolic approximation, because with EAM potentials one can only access the second-moment contribution. The density of states of non-magnetic fcc iron is indeed rather flat near the Fermi level, see for instance [67], as opposed to the

non-magnetic bcc density of states, with its characteristic peak near the Fermi level.

Figure 3.3: Equation of states of the magnetic and non-magnetic bcc (in blue) and fcc phases (in red). For the DD potentials, the continuous line refers to the ferromagnetic phase, and the dotted line to the non-magnetic phase.

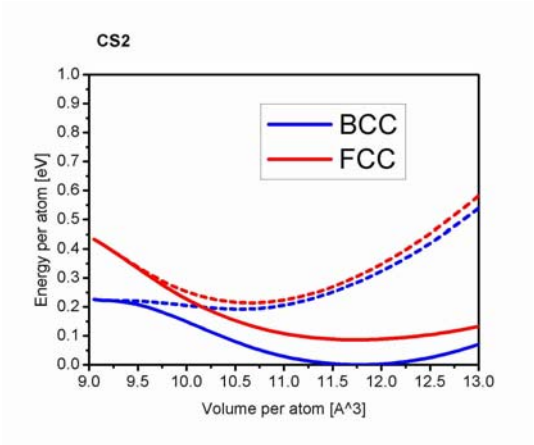

(a)

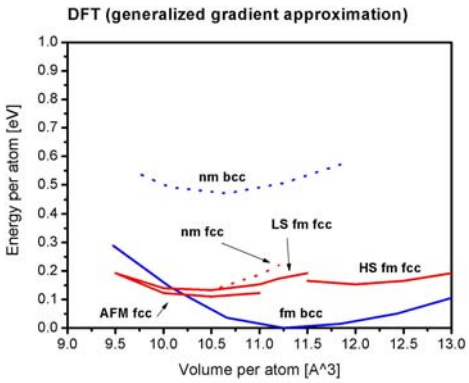

(b)

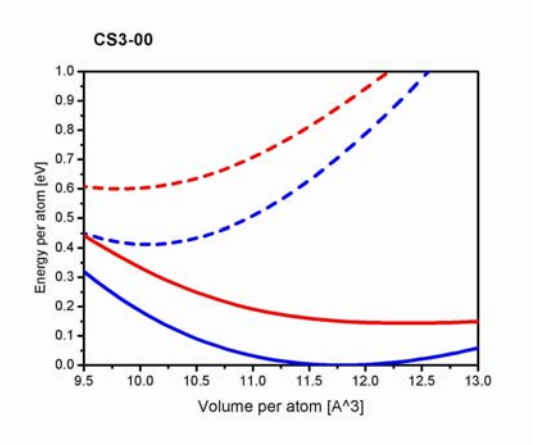

(c)

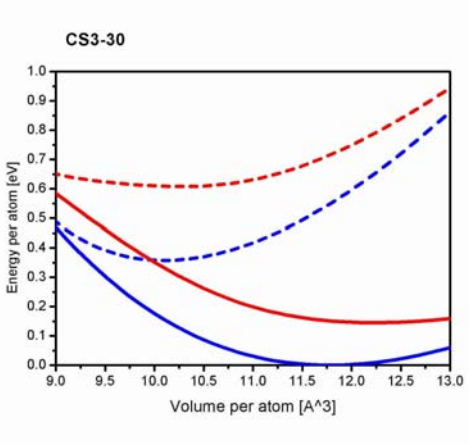

(d)

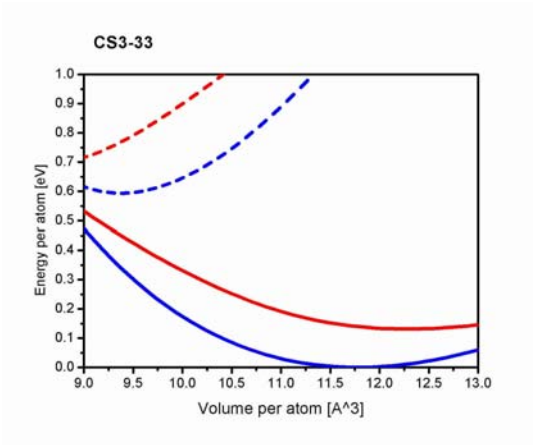

(e)

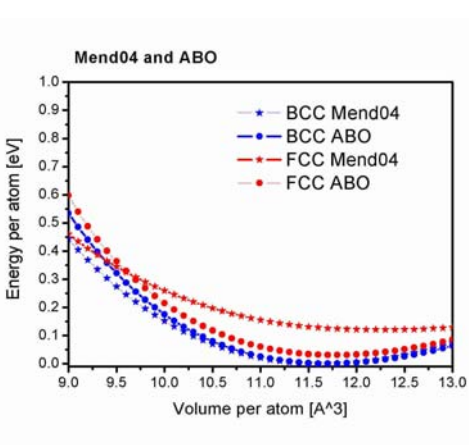

(f)

Table 3.1: Bulk properties of the ferromagnetic and non-magnetic bcc and fcc lattice. The cohesive energy E_{coh} and the energy per atom E_0 are given in eV/atom, the equilibrium volume V_0 in Å^3/atom, the equilibrium ferromagnetic moment ζ_0 in μ_{B}/atom and the anisotropic second order elastic constants in GPa. The energy per atom of the non-magnetic bcc and fcc phases is the relative energy difference per atom to the ferromagnetic bcc lattice.

	DFT	CS2	CS3-00	CS3-30	CS3-33
Ferromagnetic bcc					
E_{coh}	4.3[a]	2.5	5.3	5.1	5.8
E_0	-8.3[b]	-4.3	-11.7	-9.9	-13.9
V_0	11.4[a]	11.8	11.8	11.8	11.8
ζ_0	2.32[a]	2.2	2.2	2.2	2.2
K	190[a]	173	173	173	173
C_{44}	96[a]	122	122	122	122
C'	65[a]	52	52	52	52
Non-magnetic bcc					
E_0	0.48[d]	0.20	0.41	0.36	0.60
V_0	10.7[d]	10.5	10.1	10.1	9.4
K	276[d]	184	374	269	439
C_{44}	141[d]	102	209	93	208
C'	-110[d]	-22	55	51	25
Ferromagnetic fcc					
E_0	0.15[c]	0.09	0.14	0.15	0.13
V_0	12.0[c]	11.8	12.4	12.2	12.3
ζ_0	2.57[c]	2.06	2.48	2.34	2.47
K	170[c]	130	62	105	119
C_{44}		99	30	67	72
C'	<0[c]	33	15	34	37
Non-magnetic fcc					
E_0	0.16[d]	0.21	0.60	0.61	0.70
V_0	10.4[d]	10.7	9.8	10.3	8.7
K	317[d]	295	238	118	558
C_{44}	287[d]	164	210	110	280
C'	125[d]	71	-145	-120	-61

[a] from [20]

[b] spin-polarized VASP calculation.

[c] high spin ferromagnetic fcc from [5]

[d] from [1]

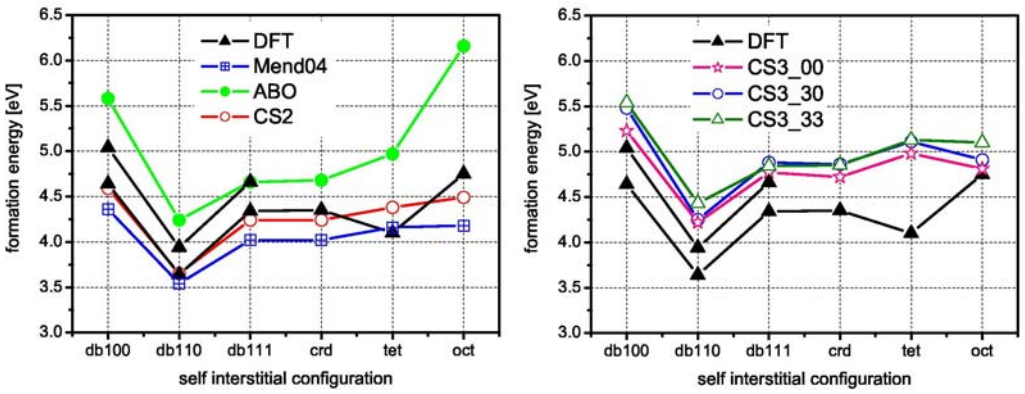

Figure 3.4: Self-interstitial formation energies. For the DFT data both the formation energy calculated at constant pressure from [4] (lower points) and that at constant volume from [17] are shown.

3.2 Static point defect properties

The formation energies and the formation volumes of the vacancy and self-interstitial point defects are summarized in table 3.2 one page 41 and figure 3.4.

For the semi empirical potentials in this work, the formation energies are obtained by relaxing at constant volume a perfect bcc supercell with one point defect, see figure 3.5 for the unrelaxed self-interstitial configurations. The formation energy is then given by

$$E_f = E_{\text{rel}} - (N \pm 1)E_0, \tag{3.1}$$

where E_{rel} is the total energy of the relaxed supercell containing one point defect, with a total of $N+1$ atoms for a self-interstitial and $N-1$ atoms for a vacancy, and E_0 is the energy per atom of the (ferromagnetic) bcc phase, see table 3.1 on page 38. The supercell containing the point defect is constructed from a perfect bcc supercell with the equilibrium lattice constant of the (ferromagnetic) bcc phase, see table 2.1. The supercell containing the point defect is thus under pressure. The pressure is however small since a supercell containing N=432 atoms was employed. The effect of pressure in the point defect formation energies of the semi-empirical potentials considered here is thus small, of the order of $\sim 3\%$. Note that this is however *not* the case for the DFT formation energies, because they were calculated on much smaller supercells with N=128 atoms. In this case, the constat volume formation energy of the dumbbells is ~ 0.3 eV higher than the constant pressure formation energy, and for the vacancy the difference is ~ 0.1 eV. The constant volume formation energies of the other self-interstitial defects have not been published.

The values of the vacancy formation energy of CS2, CS3-30 and CS3-33 from

Figure 3.5: Unrelaxed interstitial structures.

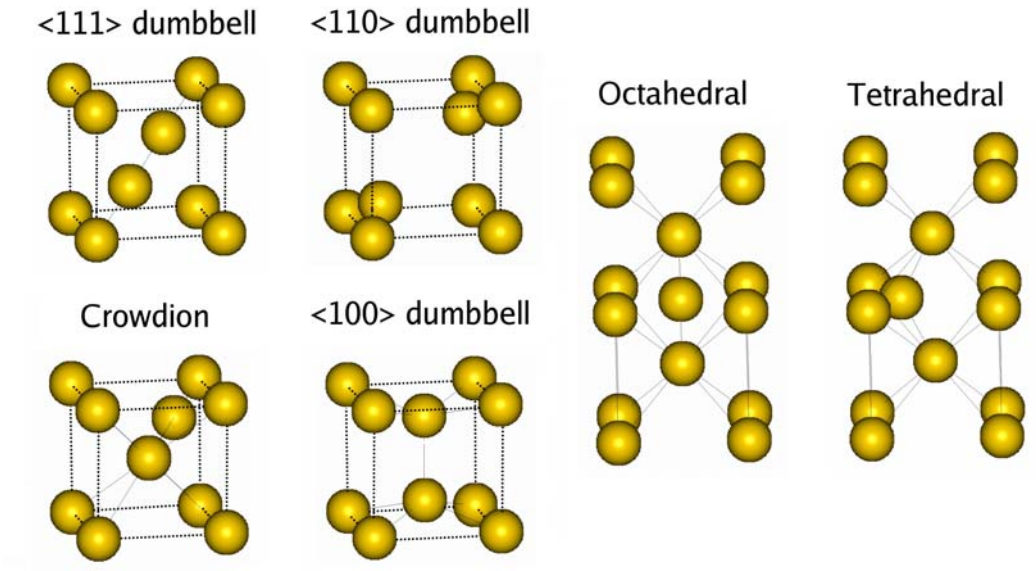

table 3.2 on page 41 are within the DFT estimate, which is also within the experimental range. CS3-00 gives a somewhat lower value closer to the vacancy formation energy of Mend04. The CS3 potentials and ABO overestimate the DFT formation energy of the self-interstitial dumbbells by ~ 0.3 eV. An important quantity in radiation damage studies is the Frenkel Pair formation energy, given by the sum of the vacancy and self-interstitial formation energies. The semi-empirical potentials are scattered around the DFT values with a deviation of ~ 0.5 eV. A comparison with the experimental range for the formation energy of a Frenkel Pair, should be taken with care because in our calculation we are neglecting the interaction energy between vacancies, self-interstitial and impurities or other defects, but also possible errors in the low temperature calorimetric measurement, or in the estimation of the total number of Frenkel Pairs.

In general, all the semi-empirical potentials can reproduce the DFT relative formation energies of the $\langle 100 \rangle$, $\langle 110 \rangle$, $\langle 111 \rangle$ dumbbells and the crowdion, but fail to reproduce the relative formation energies of the tetrahedral and octahedral self-interstitial. Note that from DFT the tetrahedral has a lower formation energy than the $\langle 111 \rangle$ dumbbell. Within our extensive fitting, it was however not possible to get a closer match of the octahedral and tetrahedral relative formation energies. The relative formation energies, and in particular the fact that the $\langle 110 \rangle$ is the ground state configuration and not the $\langle 111 \rangle$ dumbbell, are very important in radiation damage studies, because they determine to a great extent the activation energies and mobilities of the self-interstitial. The reason for this is the well known

Table 3.2: Properties of point defects in the ferromagnetic bcc lattice. For the formation and NEB migration energies (in eV) of the semi-empirical potentials the point defects are relaxed in a supercell of the same volume (but with different volume per atoms) as the reference perfect bcc supercell. The exponential prefactor of the self-interstitial diffusion coefficient is given in units of 1×10^{-3} cm^2/s with an error from the fit of 20%.

							CS3	
	Exp.[a]	DFT	Mend04	ABO	CS2	00	30	33
$E^f_{\rm vac}$	1.7,2.0	1.93[b],2.02[c]	1.71	1.56	2.07	1.70	1.95	1.95
$E^f_{\rm Frenkel}$	6.3,6.6	6.0[c]	5.2	5.8	5.7	5.9	6.2	6.4
$E^m_{\rm int,NEB}$	0.3	0.34[d]	0.30	0.22	0.25	0.37	0.40	0.33
$E^m_{\rm int,dyn}$	0.3	-	0.34	-	0.28	0.36	0.42	0.31
$D_{0,\rm int}$			1.5		1.3	2.0	3.9	2.5
$E^m_{\rm vac,NEB}$	0.55, 1.11	0.64-0.71[e]	0.62	0.90	0.78	0.94	0.94	0.85
$\beta_{\langle110\rangle}$	1.10	-	1.30	1.40	0.45	1.45	1.40	1.55
$\beta_{\rm vac}$	-0.05	-	-0.15	-0.35	-0.15	-0.10	-0.15	-0.10

[a] experimental data from [16]
[b] constant pressure calculation: the supercell of the point defect is at zero pressure [4]
[c] constant volume calculation: the supercell of the point defect is of the same size as the reference perfect bcc supercell [17]
[d] [68]
[e] [69]

fact that the $\langle111\rangle$ dumbbell has a low energy saddle point in the meV range for migration in the $\langle111\rangle$ direction. On the other hand, the $\langle110\rangle$ dumbbell migrates by a combined rotation and translation in the $\langle111\rangle$ direction, with a saddle point orientation similar to the $\langle111\rangle$ dumbbell. The activation energy for migration of the $\langle110\rangle$ dumbbell is thus correlated to the relative formation energy of the $\langle111\rangle$ and the $\langle110\rangle$ dumbbell.

We have already seen before when discussing the formation energies of point defects, that the presence of point defects changes the equilibrium volume of the system.The volume change produced by a single point defect with respect to a perfect lattice containing the same number of atoms is referred to as the formation volume of the point defect. To calculate it with semi-empirical potentials we minimize the pressure on a N=5488 atoms supercell containing either one vacancy ($N-1$ atoms) or one $\langle110\rangle$ dumbbell ($N+1$ atoms), the volume change with respect to the N atoms perfect bcc supercell and induced by the point defect is the relaxation volume ΔV, which is related to the trace of the elastic dipolar tensor of the point defect [17] and which is given here relative to the volume per atom V_0 of

the ferromagnetic bcc phase at zero temperature,

$$\beta = \frac{\Delta V}{V_0}. \tag{3.2}$$

The formation volume relative to V_0 is then given by $\beta - 1$ for a self-interstitial and $\beta + 1$ for a vacancy [17]. The relaxation volumes are collected in table 3.2 on page 41. We note that experimental values are in rather good agreement with the semi-empirical potentials, except CS2 which significantly underestimates the relaxation volumes of the $\langle 110 \rangle$ dumbbell. Note that in experimental literature there is sometimes a confusion between relaxation volume and formation volume.

As a further test of the new fits we consider small clusters of self-interstitial point defects. We have seen that the $\langle 110 \rangle$ dumbbell is the lowest energy self-interstitial predicted by all the semi-empirical potentials considered in this work, in agreement with DFT. There is however also a tendency to form clusters of self-interstitial, because the energy of a self-interstitial in a cluster is lower than the energy of an isolated self-interstitial. DFT calculations also showed that as the cluster gets bigger in size, containing more and more self-interstitial defects, the $\langle 111 \rangle$ orientation becomes energetically favored, and this happens already at a cluster size of approximately five self-interstitials [70]. We have thus studied the relative stability of these two orientations in clusters containing up to six self-interstitial dumbbells oriented either along $\langle 110 \rangle$ or along $\langle 111 \rangle$ using ABO, CS2, the CS3 potentials and Mend04. To get the zero temperature lowest energy configurations we employ a cubic shaped perfect bcc cell containing 5'488 atoms, and one $\langle 110 \rangle$ or $\langle 111 \rangle$ dumbbell. A second dumbbell with parallel orientation is added at all bcc lattice positions within 5.0 Å from the first self-interstitial. Among all relaxed configurations preserving the original ($\langle 110 \rangle$ or $\langle 111 \rangle$) symmetry, we select the one with the lowest energy. A parallel dumbbell is again added to the lowest energy configuration containing two dumbbells at all positions within 5.0 Å from the center of mass of the two self-interstitial clusters, and the resulting configurations containing three parallel dumbbells are relaxed to find the lowest energy configuration of a three self-interstitial, symmetry preserving cluster. This procedure is then iteratively repeated to find the ground state formation energies of $\langle 110 \rangle$ or $\langle 111 \rangle$ clusters containing up to six self-interstitial. Note that the position of the self-interstitial defects in the ground state cluster configurations is the same for all the semi-empirical potentials. The energy differences between the $\langle 110 \rangle$ and $\langle 111 \rangle$ ground state clusters have been plotted in figure 3.6. The comparison is made between clusters containing the same number of point defects. A negative value in the formation energy means that the cluster composed of $\langle 111 \rangle$ self-interstitial is more stable. In general, the DFT prediction that large clusters favor the $\langle 111 \rangle$ orientation is confirmed by all the semi-empirical potentials. Note however that,

for the DFT calculation, much smaller cells, with $\sim$ 100 atoms, were employed. The precise cluster size at which the transition occurs varies between three clustered self-interstitial for ABO, four clustered self-interstitial for CS2 and the CS3 potentials, and five self-interstitial for Mend04. Surprisingly, the new fits give very similar relative formation energies, in contrast with ABO and Mend04, although the third order elastic constants of the CS2 and CS3 potentials are very different. This may exclude elasticity to explain this behavior, leaving as an explanation the different cutoff radius and/or form of the interatomic interactions, that is so called core effects.

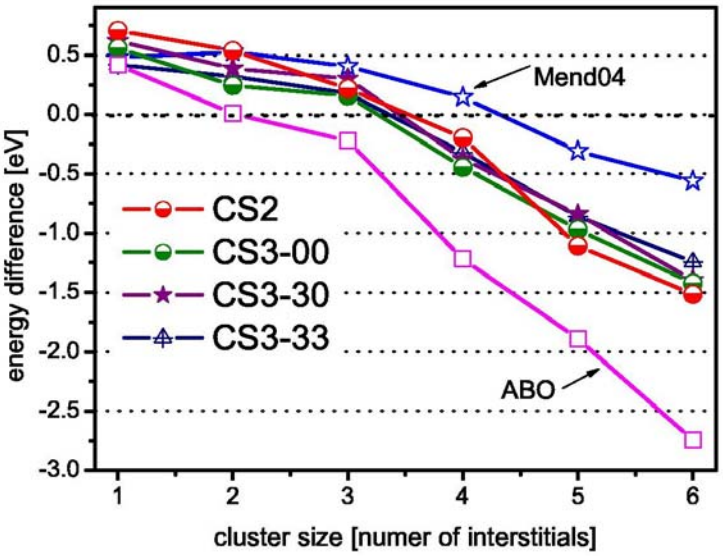

Figure 3.6: Relative formation energy of small parallel clusters. A negative value in the energy means that the cluster composed of $\langle 111 \rangle$ self-interstitials is more stable. The ground state configurations of clusters composed of M=1, ..., 6 parallel self-interstitials oriented either along $\langle 110 \rangle$ or $\langle 111 \rangle$ is obtained iteratively by adding a parallel self-interstitial to the ground state configuration of size $M-1$ at every lattice position within 5 Å from the center of mass of the $M-1$ cluster. The so obtained relaxed ground state configurations of all the semi empirical potentials are exactly the same: for the $[0\bar{1}1]$ cluster the center of mass of the dumbbells lyes on a $\{0\bar{1}1\}$ plane, that is a prismatic loop, and for the $1/2[11\bar{1}]$ cluster it lyes either on a $\{0\bar{1}1\}$ or equivalently on a $\{\bar{1}01\}$ plane, and in this case the Burgers vector is neither parallel nor perpendicular to the habit plane.

3.3 Diffusion of point defects

3.3.1 Introduction

The diffusion coefficient is a proportionality constant between the flux of point defects and the gradient in the concentration of the point defects, which is usually assumed to be independent of concentration, and to follow a simple Arrhenius law for its temperature dependence

$$D = D_0 e^{-E_A/(k_B T)}. \tag{3.3}$$

where D_0 is the diffusion coefficient at infinite temperature and E_A is the activation energy for diffusion. Our MD calculation of the diffusion coefficient of the self-interstitial in the temperature range between 300 K and 700 K shows a very good fit to the Arrhenius law. For self point defects, deviations from the Arrhenius law are first expected at temperatures which are very high compared to the migration energy [30]. We have also calculated the activation energy for migration of the $\langle 110 \rangle$ dumbbell and of the vacancy by the nudged band elastic method, see table 3.2 on page 41. The self interstitial migration energy deduced from fitting the diffusion coefficients obtained by MD to (3.3) and from the static calculation are found to be in rather good agreement in this temperature range. The vacancy migration barrier is too big for a straightforward MD computation of the diffusion coefficient in bcc iron, also because at higher temperatures magnetic effects should be taken into account.

The diffusion coefficient of the self point defects is a very important quantity in radiation damage theory [71]. For instance, the diffusion coefficients of vacancies, self-interstitial and clusters of them are used as input in microstructural evolution models like mean-field rate theory or kinetic Monte Carlo. For instance, in a recent object kinetic Monte Carlo study [26], the migration energy of the vacancy was set to 0.65 eV and the migration energy of the self-interstitial to 0.3 eV, both with an exponential pre factor of D_0=3.73$\times 10^{-3}$cm^2/s.

Experimental estimates of the self point defect diffusivities are difficult. In contrast to the case of impurities, there exist no direct way of measuring the diffusion coefficient of self point defects. For instance, the diffusivities of the self point defects can be related to the self diffusion coefficient by

$$D_{\text{self}} = D_{\text{V}} C_{\text{V}} + D_{\text{I}} C_{\text{I}} \tag{3.4}$$

where $D_{\text{V,I}}$ is the diffusivity of the vacancy or self-interstitial and $C_{\text{V,I}}$ is the concentration of vacancies or self-interstitials. In unirradiated α-iron and at intermediate

temperatures the concentration of self-interstitials is always negligible, and a measurement of the self-diffusion coefficient can thus be related to the diffusion coefficient of the vacancies, assuming a good knowledge of the concentration of vacancies, which is however not precisely the case. In α-iron, the self diffusion coefficient was measured at temperatures close to the Curie point. Experimental estimates give for the pre exponential factor for self diffusion $D_{\text{self},0}$ values from 1 cm^2/s to 1×10^2 cm^2/s and an activation energy for self diffusion E_{self} between 2.6 eV and 3.11 eV, while recent DFT estimates in pure iron give $D_{\text{self},0}=6.7\times10^{-1}\text{cm}^2/\text{s}$, using harmonic transition state theory, and $E_{\text{self}}=2.88$ eV, using NEB [69]. Thus, because the activation energy for self diffusion is given by the sum of vacancy formation and migration energy, and assuming a value of 2.0 eV for the vacancy formation energy, we see that experimental estimates of the vacancy migration energy are at least scattered between 0.6 eV and 1.11 eV. The situation is even more complicated by a still unresolved controversy in the interpretation of resistivity recovery experiments after low temperature electron irradiation, giving a value for the migration energy of the vacancy of either 0.55 eV or 1.1 eV [16]. The experimental value for the migration energy of the self-interstitial close to 0.3 eV is undisputed [16]. DFT gives a value for the migration energy of the vacancy in pure bcc iron between 0.64 eV and 0.71 eV [69], and a value for the migration energy of the self interstitial of 0.34 eV [68]. Current understanding is that the higher experimental value for the vacancy migration energy are related to a high sensibility of the vacancy diffusion coefficient to impurities, in particular to carbon, which from DFT has a binging energy to the vacancy close to 0.4 eV. On the other hand the self-interstitial seems to be only weakly interacting with carbon, which may explain why the theoretical value for the migration energy of the self-interstitial in pure iron is so close to the experimental value [72]. This finding was recently confirmed by comparison of ab initio based rate theory modeling of helium desorption experiments in α-iron. Only through the inclusion of carbon, either directly or effectively, it was possible to reproduce experiments satisfactorily, where the effective value for the vacancy migration energy in the presence of carbon must be set to 0.83 ± 0.08 eV.

The dynamical calculation of the diffusion coefficient was performed by standard NPT molecular dynamics at constant zero pressure on a periodic bcc supercell containing one dumbbell over a simulation time of 20 ns and with a time step Δt of 1 fs. To check the effect of cell size, the simulation was repeated on two supercells containing 1'025 and 15'361 iron atoms, that is with side lengths of ~ 2.2 nm and ~ 4.5 nm respectively. For Mend04, only the small supercell has been used, because the activation energy of the $\langle 110 \rangle$ dumbbell by molecular dynamics was already estimated elsewhere, and agrees very well with our calculation [14]. To calculate the diffusion coefficient, we identify the position of the two dumbbell atoms at every time step by the instantaneous center of mass of the two highest

Figure 3.7: Diffusion coefficient of isolated self-interstitial defects, calculated using either the small supercell with side length of 2.2 nm (empty stars) or the bigger supercell with side length of 4.5 nm (full circles). At a given temperature, we do not consider the diffusion coefficient if during the 20 ns simulation a jump of the self-interstitial occurs which exceeds half the simulation cell size. Diffusion coefficients lower than 0.1×10^{-6} cm^2/s are hidden from the figure, because the number of jumps (less than 100) is too low for statistical accuracy.

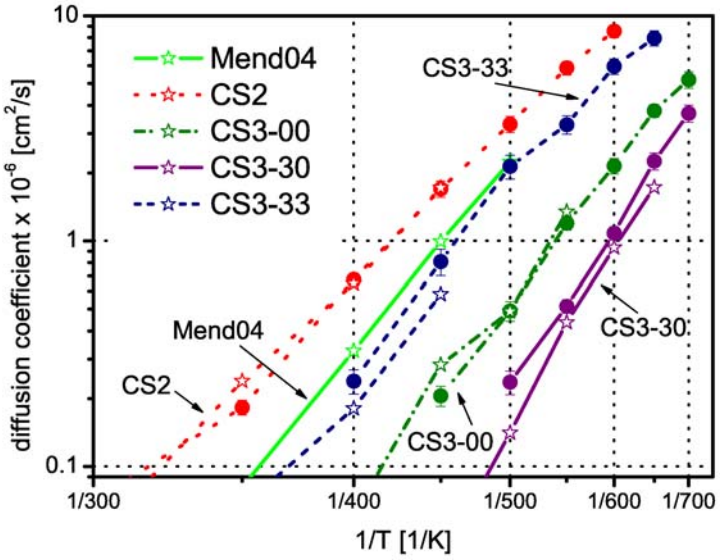

energy atoms in the supercell

$$\vec{R}_{\mathrm{h}}(t) = \frac{\vec{R}_1(t) + \vec{R}_2(t)}{2}, \tag{3.5}$$

where $\vec{R}_1(t), \vec{R}_2(t)$ are the positions of the two atoms with the highest energy over all the atoms in the supercell at time t, and $t = m\Delta t$ after m MD steps. As explained in [73], we shift the trajectory of $\vec{R}_{\mathrm{h}}(t)$ to correct for zero drift velocity. The results are shown in figure 3.7 using either the small supercell (empty stars) or the bigger supercell (full circles). At a given temperature, we do not consider the diffusion coefficient if during the 20 ns simulation a jump of the self-interstitial occurs which exceeds half the simulation cell size, see later for more details. Diffusion coefficients lower than 0.1×10^{-6} cm^2/s are hidden from the figure, because the number of jumps (less than 100) is too low for statistical accuracy. We note that the scatter between the semi empirical potentials is most important at low temperatures, where the difference can extend over many orders of magnitude, but at 700 K the scatter is strongly reduced to less than one order

of magnitude, with a diffusivity between 1×10^{-6} cm^2/s and 10×10^{-6} cm^2/s. For the case of the vacancy, assuming that the pre exponential factor be the same for all the semi empirical potentials, we expect from the static calculations of the activation energies, which range from 0.62 eV for Mend04 to 0.94 eV for CS3-00, a scatter of four orders of magnitudes at room temperatures and of two orders of magnitudes at 600K. Within our extensive fitting, it was not possible to get a value for the vacancy migration energy closer to the DFT value, but the CS3 potentials overestimate the DFT vacancy migration energy by 0.1 eV to 0.2 eV.

3.3.2 Details of the MD calculation of the diffusion coefficient of the self-interstitial

At low temperatures, the self-interstitial performs few diffusive jumps during the simulation time, which do not allow a precise enough determination of the diffusion coefficient to extract the activation energies, because the diffusion coefficient is proportional to the *mean* square displacement over time, and thus requires good statistics. At high temperatures, on the other hand, the jumps events are very frequent, but the self-interstitial point defect is also migrating very fast over distances comparable to the periodic supercell size.

A self-interstitial is substantially different than an interstitial impurity, because the diffusion of the self-interstitial does not mainly involve displacement of one atom over the jump distance, as in the case of impurities, but relatively small displacements of many atoms. Diffusion of impurities is in comparison easier to handle, because the position of the impurity atom is unambiguously known at every time step. On the other hand, the precise location of the self-interstitial dumbbell is sometimes not clearly defined because of thermal fluctuations. Although the center of mass $\vec{R}_{\mathrm{h}}(t)$ of the two highest energy atoms can be employed to calculate the diffusion coefficient, since thermal fluctuations are averaged out, it cannot be straightforwardly related to the position of the dumbbell at every time t and thus to the length of the jumps. In a standard MD code, if an atom crosses the boundary, it will be automatically shifted by the periodic lattice vectors. Since however at high temperature the precise location of the dumbbell, especially when it is migrating, is not precisely known, it is difficult to estimate when the point defect is approaching the periodic boundary. If this is not properly taken into account the diffusion coefficient will depend on the supercell size.

We now describe a method to partially overcome this problem. The method gives an estimate for the size of the jumps and can identify a situation (which always occurs at high temperatures) where the jump length is comparable to the supercell size. In this case the interaction with the periodic images of the point defect cannot be neglected any more. Since this is very difficult if not impossible

to correct, we will just neglect all simulations where the point defect jump lengths become comparable to the supercell size. If one does calculate the diffusion coefficient when the jump lengths are comparable to the supercell size, one would very likely underestimate the diffusion coefficient.

At zero temperature the position of the two dumbbell atoms is unambiguously given by the two highest energy atoms $\vec{R}_1$ and $\vec{R}_2$. As the temperature is increased, the dumbbell starts oscillating so strong from its local minima, that at some times one or both of the two highest energy atoms do not correspond with the two dumbbell atoms any more, but for instance to a nearest neighbor of the dumbbell atoms. This may occur also without the onset of a diffusive jump and is just an effect of thermal fluctuations. On the other hand, when a diffusive jump occurs, there is a very high chance that for some time the two highest energy atoms will not correspond with the dumbbell atoms, also because during the migration the point defect itself is not clearly defined. A way to handle this is by looking at the distance between the two highest energy atoms

$$l_{\mathrm{h}} = \left| \vec{R}_1 - \vec{R}_2 \right| . \tag{3.6}$$

Let us then consider a reference lattice as given by the perfect bcc supercell, with a lattice constant corresponding to the thermal expansion given by MD. We refer to the atomic positions in the reference lattice as $\vec{R}_{1,\mathrm{bcc}}, \ldots, \vec{R}_{N,\mathrm{bcc}}$. We say that at time t the dumbbell atoms are *localized* at the reference lattice position $\vec{R}_{i,\mathrm{bcc}}$ if the distance between the two highest energy atoms l_{h} is smaller than an appropriate maximum distance l_0. Now, it is clear that l_0 must be smaller than the bcc nearest neighbor distance $a\sqrt{3}/2$, because if l_{h} is bigger than this, then the two highest energy atoms cannot correspond to the two dumbbell atoms. The distance between the dumbbell atoms, and the distance from one dumbbell atom to its next nearest neighbor, are however very close and smaller than the bcc next nearest neighbor distance. l_0 must therefore be set smaller than this. A good choice is to set the maximum distance for localization l_0 equal to the distance between the two dumbbell atoms for a relaxed interstitial in the reference lattice. Consider then what happens at very low temperatures when the two highest energy atoms always correspond to the two dumbbell atoms. The distance between the two dumbbell atoms l_{h} will oscillate around l_0, and the dumbbell atom will be most of the time *not localized*, according to our definition. The way out of this is to define a characteristic thermal vibration time τ. If the dumbbell is not localized for a time smaller than τ, after which it is again localized at the last position, then we consider this as an oscillation of the dumbbell, the dumbbell has not actually moved from the last position. As already mentioned, when the temperature is increased, and the oscillations are stronger, it happens at some times that the two highest

energy atoms do not correspond at all with the dumbbell atoms. The distance l_h may *anyhow be smaller* than l_0 because the distances between the dumbbell atoms and the next nearest neighbors are very close, and according to our definition the dumbbell may be localized at a different reference lattice position. Only if this is a diffusive jump, however, will this occur for a time *bigger* than τ. Otherwise the next fluctuation will probably localize the dumbbell again at the next to last position.

Based on these considerations, let us now specify the algorithm we have developed to analyze diffusive jumps of self-interstitial defects up to moderate temperatures. Let the output of the algorithm after some iterations be

$$\left(\left(t^{\mathrm{s}}_{i,1}, t^{\mathrm{f}}_{i,1}\right), \ldots, \left(t^{\mathrm{s}}_{i,p_i}, t^{\mathrm{f}}_{i,p_i}\right)\right), \tag{3.7}$$

which means that from the start time $t^{\mathrm{s}}_{i,q}$ to the final time $t^{\mathrm{f}}_{i,q}$ the dumbbell was oscillating at position $\vec{R}_{i,\mathrm{bcc}}$, and it was oscillating here for p_i times before the current time t. Let us now assume that at

$$t = \max_{i,q}\left\{t^{\mathrm{f}}_{i,q}\right\} + \Delta t \tag{3.8}$$

the dumbbell is not localized, that is $l_{\mathrm{h}} > l_0$, and that at time $t_{\mathrm{loc}} > t$ it gets localized again at the reference lattice position $\vec{R}_{j,\mathrm{bcc}}$, , that is $l_{\mathrm{h}} < l_0$ and $\vec{R}_{j,\mathrm{bcc}}$ is the closest reference lattice point to $\vec{R}_{\mathrm{h}}(t_{\mathrm{loc}})$. Then the algorithm makes the following choice

- if $t_{\mathrm{loc}} - t^{\mathrm{f}}_{j,p_j} < \tau$ then wait until the dumbbell gets delocalized again at time t_{deloc} and then set
$$t^{\mathrm{f}}_{j,p_j} = t_{\mathrm{deloc}}, \tag{3.9}$$
- if $t_{\mathrm{loc}} - t^{\mathrm{f}}_{j,p_j} > \tau$ then wait until the dumbbell gets delocalized again at time t_{deloc}, then set
$$t^{\mathrm{s}}_{j,p_j+1} = t_{\mathrm{loc}} \tag{3.10}$$
$$t^{\mathrm{f}}_{j,p_j+1} = t_{\mathrm{deloc}}. \tag{3.11}$$

This operation is an update of (3.7) and is repeated for the entire simulation time. The first choice corresponds to an oscillation of the dumbbell at lattice position j. The second choice corresponds to the localization of the dumbbell at a new reference lattice position. At the end of the algorithm we then just consider the time intervals with

$$t^{\mathrm{f}}_{i,q} - t^{\mathrm{s}}_{i,q} > \tau \tag{3.12}$$

to give the position of the dumbbell.

To suppress the dumbbell from crossing the periodic boundary we shift the position of every atom in the supercell at every time step m so that the center of mass of the *six* highest energy atoms is kept exactly at the center of the periodic supercell, and the effect of the shift is correctly accounted for in $\vec{R}_{\rm h}(t)$. The reason why we employ the six highest energy atoms is just that at zero temperature this corresponds to the two dumbbell atoms and its four next nearest neighbors, and as the temperature is increased the center of mass of the six highest energy atoms fluctuates less around the position of the dumbbell than the two highest energy atoms.

We have then analyzed all the MD simulations with the above algorithm by setting τ=1 ps and l_0 equal to the distance between the dumbbell atoms in the reference lattice. We have checked the algorithm by comparing at every time t the position of $\vec{R}_{\rm h}(t)$ and we have found that $\vec{R}_{\rm h}(t)$ fluctuates around the position predicted by the algorithm, as can be seen in figure 3.10 on page 53, where we compare $\vec{R}_{\rm h}(t)$ calculated in the small supercell and using CS3-33 at 600 K with the position predicted by the algorithm. We have also compared the diffusion coefficient calculated with $\vec{R}_{\rm h}(t)$ or with the position given by the algorithm, and found perfect agreement between these two values. The algorithm in thus validated.

When the position of the dumbbell as predicted by the algorithm changes to a new lattice site it means that the dumbbell is now oscillating for a time longer than τ at the new position. It is thus possible and very interesting to extract information about the distance traveled by the interstitial between two successive localizations at different lattice sites, which we call a jump of the self-interstitial. Figure 3.8 shows the frequency count of the jump distances (or lengths) calculated in the small supercell unsing CS3-33 at 600 K. Each peak in the figure corresponds to a neighboring shell in the perfect bcc lattice, and the height of the peak gives how many times over the 20 ns simulation the self-interstitial has displaced in a given neighboring shell. With 55% of the total number of jumps, the most frequent event is the displacement of the self-interstitial to the nearest neighbor position, that is the first neighbor along the $\langle 111 \rangle$ direction. Almost 15% of the jumps are to the second nearest neighbor along the $\langle 111 \rangle$ direction, and 5% of the jumps are to the third nearest neighbor along the $\langle 111 \rangle$ direction. We thus see that, according to our algorithm, most of the jumps occur along the $\langle 111 \rangle$ directions, and the distance traveled by the self-interstitial between successive localizations is bigger than the nearest neighbor distance. The displacement of the $\langle 110 \rangle$ dumbbell can be thought as an excitation of the crowdion self-interstitial, which then decays again to a $\langle 110 \rangle$ dumbbell. The relative height of the peaks depends on temperature, and on the choice of the semi empirical potential. At lower temperatures, the most probable event is the diffusion to the next nearest neighbor, and as the temperature

Figure 3.8: Frequency count of the jump distances (or lengths) calculated in the small supercell unsing CS3-33 at 600 K. Each peak in the figure corresponds to a neighboring shell in the perfect bcc lattice, and the height of the peak gives how many times over the 20 ns simulation the self-interstitial has displaced in a given neighboring shell.

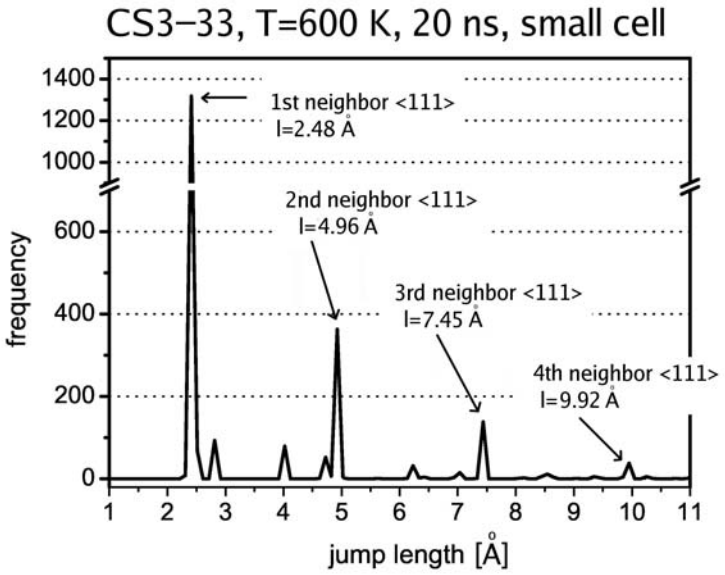

increases diffusive events to neighbors along the $\langle 111 \rangle$ direction, as well as to other neighbors, become more likely. This is a general behavior of all the semi empirical potentials considered in this work.

In figure 3.9 we show the maximum jump length over our 20 ns MD simulations. The left side of the figure refers to the small simulation cell with a side length of 2.2 nm, while the right side refers to the bigger cell with a side length of 4.4 nm. Simulations in the shaded area of the figure, which corresponds to jumps exceeding half the supercell size, are not considered, because in those cases the self-interstitial may have crossed the periodic boundary without notice. Moreover, the jump length becomes comparable to the distance between the periodic images of the dumbbell. At low temperatures, on the other hand, we need at least 100 jumps over the 20 ns for statistical accuracy. Only diffusion coefficient of simulations satisfying these criteria are shown in figure 3.7 on page 46, and have been employed to get the activation energies by linear (1/T-log) fit. The activation energies so obtained are in rather good agreement with the static NEB calculation, see table 3.2 on page 41.

An alternative way to identify the position of the dumbbell is by counting the number of atoms occupying each Wigner-Seitz cell, and by identifying the position of the self-interstitial as the cell containing two atoms [14]. This method

is more accurate but also more expensive, especially if it has to be employed after every time step. It is moreover not clear whether this method is more successful in tracking the position of the dumbbell when it is quickly jumping along the $\langle 111 \rangle$ directions, and thus avoid the dumbbell from crossing the periodic boundary without notice. One would however probably need to employ this more accurate method in the study of the vacancy diffusion coefficient.

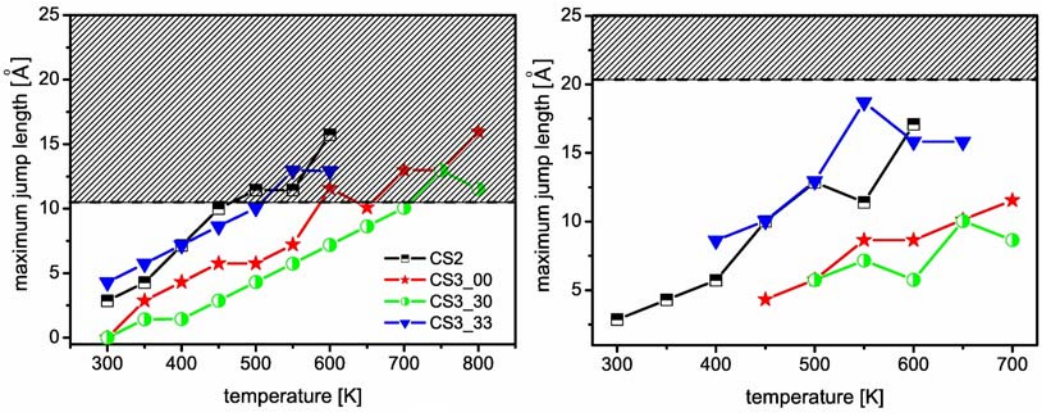

Figure 3.9: Maximum jump length over our 20 ns MD simulations. The left side of the figure refers to the small simulation cell with a side length of 2.2 nm, while the right side refers to the bigger cell with a side length of 4.4 nm. Simulations in the shaded area of the figure, which corresponds to jumps exceeding half the supercell size, are not considered in the calculation of the activation energy for diffusion.

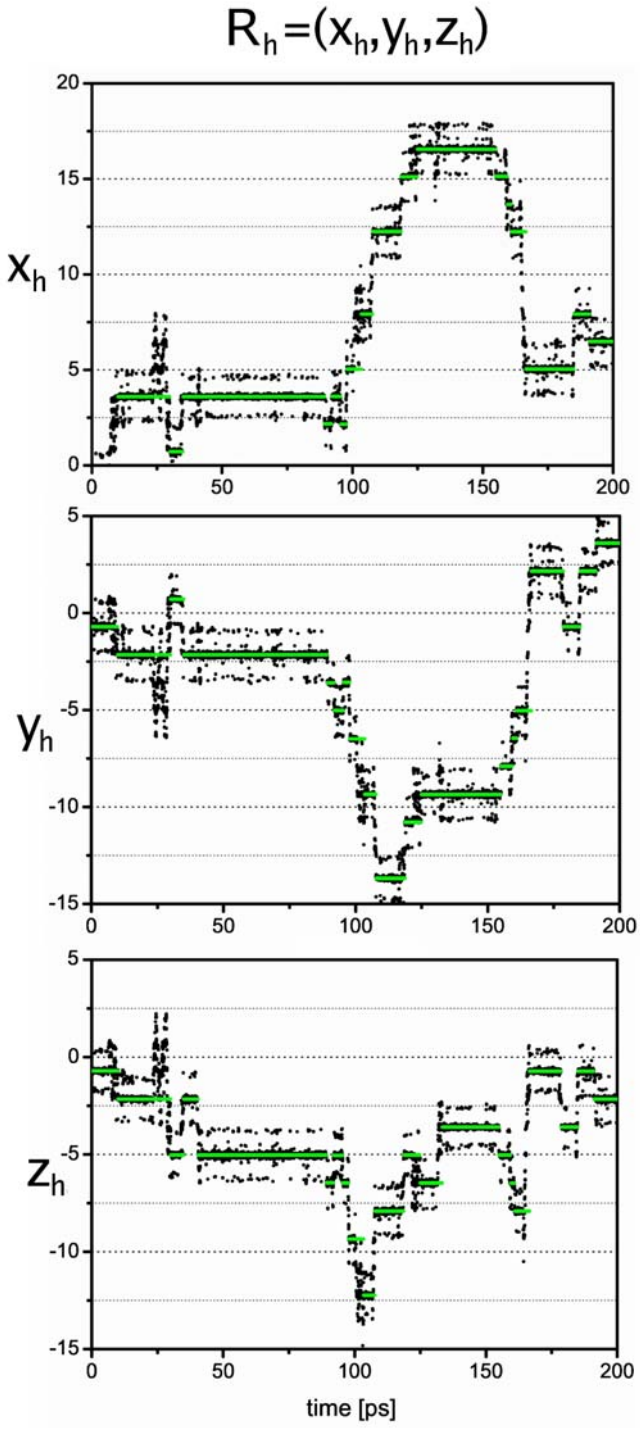

Figure 3.10: Validation of the algorithm to locate the position of the dumbbell. In black the position of the center of mass R_h of the two highest energy atoms in the small supercell, using CS3-33 at 600 K. The green line is the average position of the dumbbell given by the algorithm.

3.4 Formation free energy of the ⟨110⟩ dumbbell, harmonic and anharmonic contributions

The formation free energy of the ⟨110⟩ dumbbell has been calculated using Mend03, Mend04, CS2, CS3-00 and CS3-30 and comparing the harmonic, quasi-harmonic and thermodynamic integration methods. This work has been published in [38]. The calculations do not consider CS3-33, because at that time when the calculation for the other potentials was performed, it was not yet selected as an optimal fit. CS3-33 is expected to perform very similar to the other semi-empirical potentials.

3.4.1 Introduction

The vibrational properties of defects give information about how a defect behaves at finite temperature within a molecular dynamics simulation and can be used to investigate the stability of defects through a comparison of the formation free energies. These vibrational properties are generally calculated within the harmonic approximation to the crystal potential enabling a straightforward determination of thermodynamic quantities such as the vibrational free energy, entropy, and heat capacity. Moreover through an analysis of the low frequency modes, information can be gained at possible transition pathways for structural migration or transformation of defects. Work of this nature has been done to investigate the relative stability as a function of temperature of ⟨110⟩ and ⟨111⟩ single interstitials as well as small clusters of interstitials forming either glissile prismatic loops [24] or so-called 'self-trapped' sessile structures [28]. Work comparing the harmonic vibrational properties of vacancies, single interstitial and small interstitial loops for the above mentioned empirical potentials has however revealed a wide spread in the defect formation entropies and therefore the temperature behavior of the corresponding formation free energies. A recent ab initio calculation of the harmonic vibrational properties of the ⟨110⟩ and ⟨111⟩ dumbbell interstitials in bcc Fe [74] now provides additional data through which a quantitative assessment of an empirical potential can be made.

It is however unclear to what extent the harmonic term contributes to the total free energy of the defect. For a perfect lattice containing inversion symmetry, third order anharmonic contributions are expected to cancel at low temperatures and it is only at the fourth order that anharmonic contributions will begin to be present. At higher temperatures where the atomic vibrations increasingly deviate away from the perfect lattice configuration a non-negligible anharmonic contribution to the vibrational entropy and corresponding free energy will increasingly occur [75]. For the case of interstitials, which break the lattice symmetry at and around the core of the defect and also involve large local compressive strains, little

knowledge exists about the magnitude of the anharmonic contribution to the free energy. Additionally, the harmonic approach to estimating the free energy becomes problematic when defect diffusion occurs at a time scale comparable to the characteristic vibrational period of the defect. In this regime, where a diffusion event (a so-called lattice "hop") may no longer be considered a rare event, the defect cannot reach local thermal equilibrium before the next migration and the concept of a harmonic ground state becomes meaningless.

The main goal is to investigate the anharmonic contribution to the total formation free energy of the single $\langle 110 \rangle$ dumbbell interstitial by comparing the usual harmonic result with the anharmonic free energy obtained using a thermodynamic integration technique.

3.4.2 Harmonic, quasi-harmonic and anharmonic contribution to the free energy

Harmonic method

The most popular method to calculate vibrational free energy of a particular atomic configuration is based on the harmonic approximation. Within this approximation, the potential energy function (2.2) of a periodic system of N atoms is expanded to second order near a local minima obtained either by conjugate gradient or molecular statics structural relaxation methods. This local minimum defines the zero temperature ground state structure of the atomic configuration. Let the atomic coordinates of this local minima be given by $\vec{R}_1^0, \ldots, \vec{R}_N^0$, and let $\vec{u}_1, \ldots, \vec{u}_N$ be small displacements of the atoms away from this local minima. Then we have

$$E(\vec{R}_1^0 + \vec{u}_1, \ldots, \vec{R}_N^0 + \vec{u}_N) \approx E_{\text{local}} + \frac{1}{2} \sum_{\substack{i,j=1,\ldots,N \\ \mu,\nu=x,y,z}} u_i^\mu D_{ij}^{\mu\nu} u_j^\nu, \tag{3.13}$$

where $\mu, \nu = x, y, z$ refer to the Cartesian coordinate (polarization) directions, $i, j = 1, \ldots, N$ are the atomic indices and $E_{\text{local}} = E(\vec{R}_1^0, \ldots, \vec{R}_N^0)$ is the local energy minima. The translational invariant force matrix is given by

$$D_{ij}^{\mu\nu} = \Lambda_{ij}^{\mu\nu} - \delta_{ij} \sum_k \Lambda_{ik}^{\mu\nu}, \tag{3.14}$$

where $\widehat{\Lambda}$ is the Hessian matrix of rank $3N$ defined by

$$\Lambda_{ij}^{\mu\nu} = \left. \frac{\partial^2 E(\vec{R}_1, \ldots, \vec{R}_N)}{\partial R_i^\mu \partial R_j^\nu} \right|_{\vec{R}_1^0, \ldots, \vec{R}_N^0}. \tag{3.15}$$

The classical vibrational free energy within the harmonic approximation is then given by [75]

$$F(T,N) = E_{\text{local}} + k_B T \sum_{n=1}^{3N-3} \ln\left(\frac{\hbar\omega_n}{k_B T}\right) \tag{3.16}$$

where $\omega_n = \sqrt{\frac{d_n}{M}}$, $n = 1, \ldots, 3N$ are the vibrational frequencies of the system calculated from the eigenvalues d_n of the force matrix $\widehat{D}$. The sum in (3.16) excludes the zero frequency translational modes and thus spans the positive $3N-3$ frequencies. Here M is the mass of an Fe atom, $\hbar$ Planck's constant and k_B Boltzmann's constant.

When considering either a perfect lattice or a defect structure, the corresponding atomic configuration is relaxed at a particular volume to obtain the force matrix. The chosen volume can be the 0 K equilibrium value or a value obtained from zero-pressure finite temperature dynamical simulations. Performing a harmonic expansion at the chosen volume will result in the vibrational frequencies depending implicitly on that volume - this approach is referred to as the quasi-harmonic approximation. In what follows, the harmonic free energy will refer to a harmonic expansion at the 0 K equilibrium volume whose temperature dependence arises explicitly via (3.16). On the other hand, a quasi-harmonic free energy at a given temperature T arises from a harmonic expansion at a volume obtained from zero-pressure dynamical simulations performed at temperature T where (3.16) is evaluated only at T.

Estimation of the anharmonic contribution to the free energy: the Frenkel-Ladd method

The free energy of a system is defined entirely by its Hamiltonian $H_1 = H_1\left[(\vec{r}_i, \vec{p}_i)\right]$, and cannot be expressed as a simple ensemble average such as can be done for internal energy, heat capacity and stress. However by constructing the Hamiltonian

$$H(\lambda) = (1-\lambda)H_0 + \lambda H_1, \tag{3.17}$$

where $H_0 = H_0\left[(\vec{r}_i, \vec{p}_i)\right]$ is a reference Hamiltonian, the difference in free energy can be expressed in terms of a thermodynamic integration over an ensemble average [76] with respect to $H(\lambda)$

$$F_1 - F_0 = \int_0^1 \frac{dF(\lambda)}{d\lambda} d\lambda = \int_0^1 \langle \frac{\partial H(\lambda)}{\partial \lambda} \rangle_\lambda d\lambda = \int_0^1 \langle H_1 - H_0 \rangle_\lambda d\lambda, \tag{3.18}$$

where

$$\langle H_1 - H_0 \rangle_\lambda = \frac{1}{Z_\lambda} \int d\vec{p}_1 \cdots \vec{p}_N d\vec{r}_1 \cdots \vec{r}_N (H_1 - H_0) \exp\left[-\beta H(\lambda)\right] \tag{3.19}$$

in which, Z_λ is the corresponding partition function of $H(\lambda) = (1-\lambda)H_0 + \lambda H_1$ and $\beta = 1/(k_B T)$.

Equation (3.16) can then be used to determine the total free energy, F_1, of an N atom configuration, by choosing a $H_0 = H_0\left[(\vec{r}_i, \vec{p}_i)\right]$ for which F_0 is known, and calculating $\langle H_1 - H_0 \rangle_\lambda$ either via a molecular dynamics or an ensemble Monte Carlo (MC) simulation. In the present work we employ as a reference Hamiltonian, H_0; the harmonic expansion around a local minima, see equation (3.13) and use the Monte Carlo numerical technique to determine the ensemble average. In this way, Monte Carlo simulations will yield $F_1 - F_0$ via equation (3.18), which is the anharmonic contribution to the free energy. Adding the harmonic contribution (3.16), to this then gives the total free energy of the atomic system.

3.4.3 Results

Formation free energy of the $\langle 110 \rangle$ interstitial dumbbell

The formation free energy of a self-interstitial at temperature T is defined as

$$\Delta F(T) = F_{\mathrm{DB}}(T, N+1) - \frac{N+1}{N} F_{\mathrm{bcc}}(T, N), \tag{3.20}$$

where $F(T) = F_{\mathrm{DB}}(T, N+1)$ and $F_{\mathrm{bcc}}(T, N)$ are, respectively the absolute free energy of the periodic super-cell containing $N+1$ atoms including the single interstitial and of the perfect bcc periodic super-cell containing N atoms. The formation free energy may depend sensitively on whether the two supercells have the same volume, the same volume per atom or the same pressure.

In the present section the free energy of the $\langle 110 \rangle$ dumbbell is calculated using the harmonic, the quasi-harmonic and the thermodynamic integration methods. For all cases a periodic simulation cell consisting of 2'001 atoms for the interstitial configuration and 2'000 atoms for the bcc reference lattice is employed to ensure minimal super-cell size effects. For the harmonic calculation we relax the $\langle 110 \rangle$ dumbbell configuration using molecular statics in a simulation cell that has a fixed volume per atom equal to that of the 0 K equilibrium bcc volume per atom. For the quasi-harmonic calculation, the $\langle 110 \rangle$ dumbbell is further relaxed at fixed volumes per atom corresponding to the 300, 400, 500 and 600 K equilibrium bcc volume per atom obtained from zero pressure molecular dynamics simulations using the

Figure 3.11: $\langle H_1 - H_0 \rangle_\lambda$ for the $\langle 110 \rangle$ interstitial dumbbell as a function of the thermodynamic integration parameter λ for the temperatures 300 and 600 °K for the empirical potentials (a) Mendelev-2003, (b) Mendelev-2004, (c) CS3-00, (d) CS3-30, and (e) CS2. At values of λ close to unity, $\langle H_1 - H_0 \rangle_\lambda$ does not converge for all empirical potentials due to diffusion of the defect.

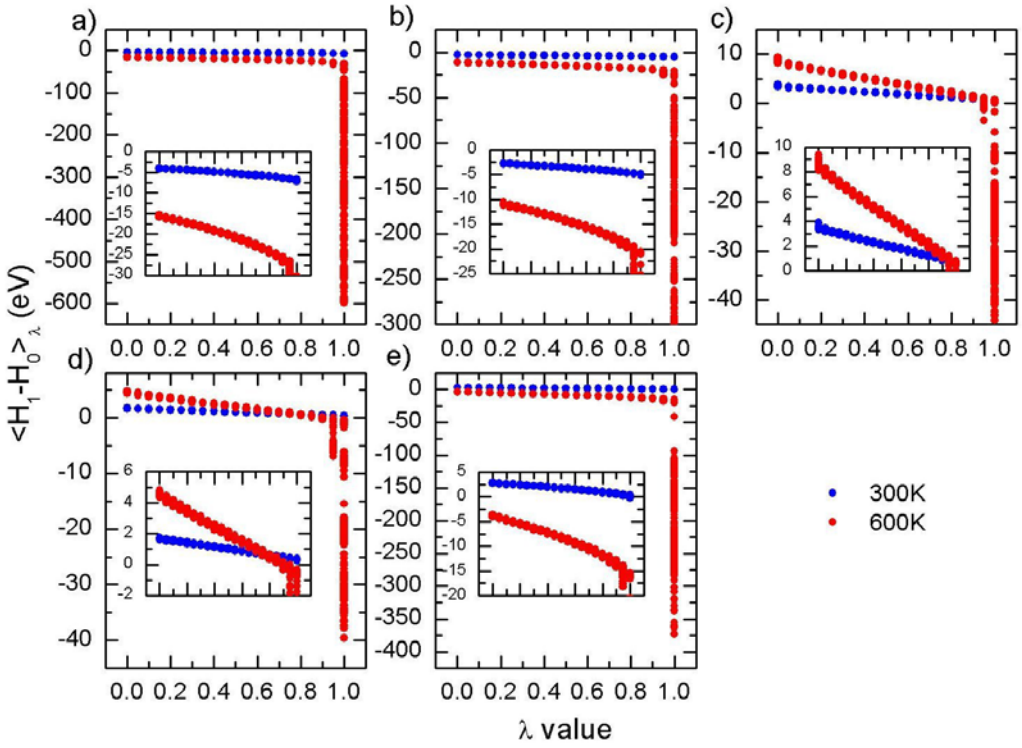

Parrinello-Rahman barostat method. Table 3.4 on page 62 shows the temperature dependent equilibrium bcc energies per atom and volumes for the empirical potentials used, and we see that for the case of the CS2 potential thermal contraction rather than thermal expansion occurs for the considered temperature range. Table 3.4 also displays the relaxed defect formation energies of the $\langle 110 \rangle$ dumbbell interstitial at these temperatures and corresponding fixed volumes per atom. For all empirical potentials a decrease in the relaxed formation energies occurs with increasing temperature.

For the thermodynamic integration free energy calculation, these fixed volumes per atom configurations are used in constant volume ensemble MC simulations at the corresponding temperatures to determine $\langle H_1 - H_0 \rangle_\lambda$ for λ=0.00, 0.05, 0.1, ..., 0.95, 1.00 using the Frenkel-Ladd method outlined in the previous section. To obtain a high level of precision the ensemble averages are performed using $\sim 10^8$ accepted Monte Carlo steps. Each trial Monte Carlo step involved a randomly

chosen atom being randomly displaced by a maximum distance of 0.1 Å. We note that by keeping the volume fixed the present calculations do not consider free energy contributions arising from volume fluctuations. Due to the translational invariance of the full Hamiltonian, $H_1 = H_1\left[(\vec{r}_i, \vec{p}_i)\right]$, and therefore also of $H(\lambda)$ at $\lambda = 1$, the center of mass of the system is also coupled to an artificial harmonic oscillator to minimize fluctuations in $H_1 - H_0$ as λ approaches 1. The resulting free energies are then accordingly corrected using the known analytical result for the free energy of a harmonic oscillator to yield the total free energy of the defect.

Figure 3.11 displays $\langle H_1 - H_0 \rangle_\lambda$ for the interstitial defect, as a function of the temperatures 300 and 600 K. Data for all potentials are shown. Each data point represents the average of approximately 300'000 to 500'000 accepted Monte Carlo steps. For the 300 K calculation good convergence is seen for all values of λ and the thermodynamic integration may be easily performed. On the other hand, for the 600 K calculation, $\langle H_1 - H_0 \rangle_\lambda$ does not converge for λ values at and close to unity indicating large fluctuations in $H_1 - H_0$ occur during the MC sampling. The origin of such fluctuations lies in the interstitial defect undergoing diffusion, where inspection of the 600 K atomic configurations derived from the Monte-Carlo simulations reveals that the $\langle 110 \rangle$ dumbbell has moved to a rotated $\langle 110 \rangle$ dumbbell centered at a different site. This occurs naturally in the full Hamiltonian of the system $H_1 = H_1\left[(\vec{r}_i, \vec{p}_i)\right]$ whilst being entirely suppressed in the reference (harmonic) Hamiltonian $H_0 = H_0\left[(\vec{r}_i, \vec{p}_i)\right]$. At values of λ close to unity, diffusion is therefore allowed resulting in large values of H_0 since the defect is far away from the Harmonic minimum. This is a fundamental limitation of the Frenkel-Ladd method. Although diffusion is present in the 600 K simulations, the $\langle 110 \rangle$ dumbbell interstitial defect will spend most of its time in its ground state configuration and the lack of convergence encountered in figure 3.11 can be remedied by standard cubic-spline extrapolation of $\langle H_1 - H_0 \rangle_\lambda$ to values of λ near 1.

Figure 3.12 displays the harmonic, quasi-harmonic and total formation free energies as a function of temperature for the potentials considered. There are significant differences across the empirical potentials due firstly to the different zero temperature formation energies, see table 3.4 on page 62, and secondly the different temperature dependencies of the free energy. The latter being particularly the case for CS2, see figure 3.12 (b), where the harmonic and quasi harmonic formation free energies increase with increasing temperature. When comparing the harmonic, quasi-harmonic and total formation free energies for a given potential, we see that the harmonic values generally overestimate the free energy. For the CS2 potential (in figure 3.12 (b)) the over estimation is considerable indicating it's strongly anharmonic nature, whereas for the Ackland-Mendelev (in figure 3.12 (a)) and CS3 (in figure 3.12 (c)) potentials the anharmonic correction is relatively small and indeed negligible for the CS3-30 potential.

Figure 3.12: The formation free energy of the ⟨110⟩ dumbbell interstitial derived from the harmonic, quasiharmonic, and thermodynamic integration techniques using (a) the Mendelev-2003 and Mendelev-2004 empirical potentials, (b) the CS2 empirical potentials, and (c) the CS3-00 and CS3-30 empirical potentials. The solid lines represent the harmonic, the triangled data represent the quasiharmonic, and the filled circles represent the total free energy.

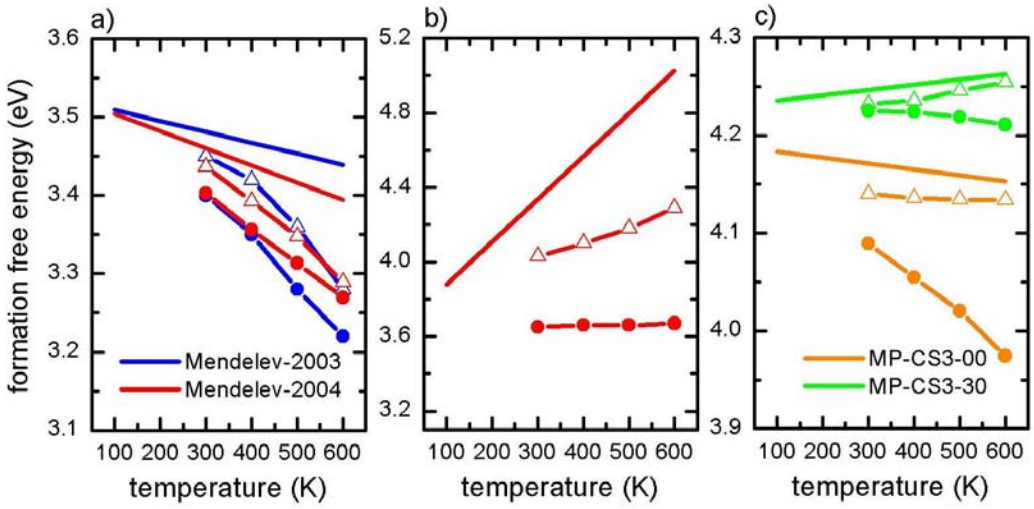

Formation entropies

The temperature dependence of the vibrational free energy may be largely understood from knowledge of the vibrational entropy. Thermodynamically, entropy may be obtained from the free energy via

$$S = -\frac{\partial F}{\partial T}. \tag{3.21}$$

For a direct measure of the total formation entropy, the results contained within figure 3.12 are fitted to $\Delta F(T) = \Delta E_0 - \Delta S_V T$, where ΔE_0 is the 0 K formation energy of the ⟨110⟩ dumbbell taken from table 3.4 on page 62 and ΔS_V is the formation entropy at fixed volume per atom. We note that the formation entropy of a defect structure is defined analogously to the formation free energy, see equation (3.20). In columns one to four of table 3.3 we show the results of this method applied to all three free energy estimates. Whilst absolute entropy can only be positive, the formation entropy of a defect can be negative and simply indicates that the defect lowers the entropy relative to that of the surrounding lattice.

Within the harmonic and quasi-harmonic approximation, the vibrational entropy may be easily obtained by explicitly differentiating (3.16). Table 3.3 also

lists for all potentials the harmonic formation entropy at 300 K at fixed volume (ΔS_0), constant volume per atom (ΔS_V) and zero hydrostatic pressure (ΔS_P). For the case of fixed volume and constant volume interstitial structures, the reference is the equilibrium bcc lattice for the corresponding potential. Data from the literature are also shown, in particular the constant pressure calculation of Marinica and Willaime [24] and a recent DFT calculation of Lucas and Schäublin [74].

	Harmonic method	Quasi-harmonic method	Thermo-dynamic integration	Harmonic ΔS_0	Harmonic ΔS_V	Harmonic ΔS_P
CS2	-26.58	-12.71	-0.28	-23.66	-26.59	-24.73 **(-21.04)**
Mend03	1.80	4.08	5.67	2.94	1.62	1.27 **(2.84)**
Mend04	2.55	4.20	4.92	1.81	2.72	4.02
CS3-00	0.71	1.31	4.02	-5.39	0.53	3.13
CS3-30	-0.63	-0.34	0.28	-4.17	-0.65	0.69
DFT [74]					0.24	

Table 3.3: Formation entropies in units of k_B of the $\langle 110 \rangle$ interstitial dumbbell. In parentheses for comparison results from [24].

Table 3.4: Equilibrium bcc volume per atom (Å^3) and energy per atom (eV) as a function of temperature for the empirical potentials considered in the present work. Also shown are the $\langle 110 \rangle$ interstitial dumbbell formation energies (eV) as a function of temperature for atomic configurations whose volume per atom is set to the corresponding equilibrium bcc volume per atom.

Temperature (K)	bcc equilibrium volume per atom (Å^3)	bcc energy per atom (eV)	$\langle 110 \rangle$ dumbbell formation energy (eV)
		CS2	
0	11.7768	-4.3160000	3.65
300	11.7381	-4.3159312	3.63
400	11.7135	-4.3158156	3.61
500	11.6972	-4.3157079	3.60
600	11.6912	-4.3156619	3.60
		Mend03	
0	11.6393	-4.12243923	3.52
300	11.6845	-4.12234347	3.51
400	11.7141	-4.12217542	3.51
500	11.7472	-4.12189093	3.50
600	11.7859	-4.12142889	3.49
		Mend04	
0	11.6393	-4.01298646	3.53
300	11.7001	-4.01280968	3.51
400	11.7295	-4.01259930	3.51
500	11.7602	-4.01229416	3.50
600	11.7948	-4.01186661	3.49
		CS3-00	
0	11.7768	-11.64735826	4.19
300	11.9001	-11.64683629	4.13
400	11.9297	-11.64650881	4.12
500	11.9595	-11.64610405	4.11
600	11.9889	-11.64562897	4.09
		CS3-30	
0	11.7768	-9.89319216	4.23
300	11.8387	-9.89301704	4.21
400	11.8573	-9.89289711	4.20
500	11.8755	-9.89274959	4.19
600	11.8941	-9.89256858	4.18

3.5 Fitting parameters of the local ferromagnetic moment

For CS2 the parameters for the local ferromagnetic moment were previously optimized to reproduce the bulk magnetic moment as a function of homogeneous volume changes computed with DFT [6]. In the present work we try a new approach where we focus on the variation of the Stoner exchange energy

$$E_{\mathrm{X}}(\zeta) - E_{\mathrm{X}}(\zeta_0) = \frac{1}{4} I_S \left(\zeta_0^2 - \zeta^2\right). \tag{3.22}$$

which is related to the magnetic moment ζ via the Stoner parameter I_S, and where ζ_0 is the equilibrium value of the magnetic moment per atom. A comparison of the local magnetic moment between different dynamical models seem to us only meaningful if they are related in a similar way to a change in the total energy of the system. For this reason we have optimized the parameters C, ρ_c and γ in (2.11) such that the magnetic moment is related to the Stoner exchange energy via a Stoner parameter of $I_S \simeq 0.7$ eV/(atom μ_{B}^2), which is in the theoretical and experimental range of bcc iron, that is from 0.4 to 0.8 eV/(atom μ_{B}^2) [67, 77]. We also require an equilibrium ferromagnetic moment per atom in the bcc phase of ζ_0=2.2 μ_B, which is close to the experimental value. Moreover, we keep an eye on the ferromagnetic moment distribution in the core of the $\langle 110 \rangle$ self-interstitial. For more details, see (A.36), (A.38), (A.39) and (A.40) in appendix A.

In table 3.6 we show the local ferromagnetic moment in the core of the $\langle 110 \rangle$ self-interstitial for the optimal parameter set. The magnetic moment in the core of the self-interstitial is indeed strongly reduced, see figure 3.14.

Figure 3.13 shows the dependence of the bulk ferromagnetic moment on homogeneous volume changes. It is evident from this picture that for moderate compressions the magnetic moment is almost linearly related to the isostatic pressure. As explained in the appendix A, however, the comparison is only meaningful for positive values of the magnetic moment $\zeta > 0$. Note again that the present parametrization does not reproduce the Stoner exchange energy as given in figure

	CS2	CS3-00	CS3-30	CS3-33
C	3.2959	4.6869	4.2309	4.4511
ρ_c	0.88	0.70	0.75	0.66
γ	0.3	0.3	0.3	0.3

Table 3.5: Parameters to set in equation (2.11), on page 18. C is given in units of μ_{B}, ρ_c and γ are dimensionless

Figure 3.13: Bulk ferromagnetic moment as a function of volume per atom changes using the optimal parameter set of table 3.5, the inset shows the ferromagnetic moment as a function of pressure.

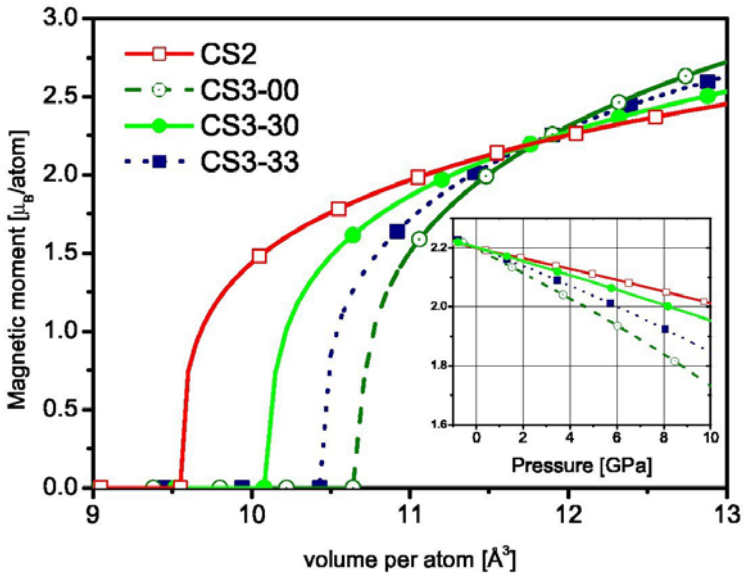

A.2 exactly, but only the relative ordering and the order of magnitude are retained. We have done this to improve the description in the core of the dumbbell, and in particular not to allow the moment to become zero. Considering the exchange energy in (A.38) *exactly*, the value of the magnetic moment at 10 GPa would have been ζ=2.11 μ_B for CS2, ζ=1.85 μ_B for CS3-30, ζ=1.76 μ_B for CS3-33 and ζ=1.65 μ_B for CS3-00. Thus we see that compared to a magnetic moment giving an exact description of the Stoner exchange energy (A.38) with a Stoner parameter of 0.7 eV/(atom μ_{B}^2), the present parametrization slightly underestimates the magnetic moment on compressions for CS2, and overestimates it for the CS3 potentials.

The DD interatomic potential formalism offers for the first time the possibility to study the magneto-elastic effect on million atom simulations at a very cheap computational cost. The effect on the $b = 1/2[111]$ edge dislocation core is quite significant. In the compressive region of the core, that is the lower half plane on figure 3.15 (a), the magnetic moment is reduced down to $\sim$ 1.7 μ_B, while in the tensile region of the core in the upper half plane the magnetic moment increases up to $\sim$ 2.5 μ_B. On the other hand, the magneto-elastic effect on the $b = 1/2[111]$ screw dislocation is negligible, see figure 3.15 (b). This is due to the lack of a strong hydrostatic stress variation in the case of the screw dislocation.

Figure 3.14: Magnetic moment on self-interstitial using CS3-30 and the new parametrization.

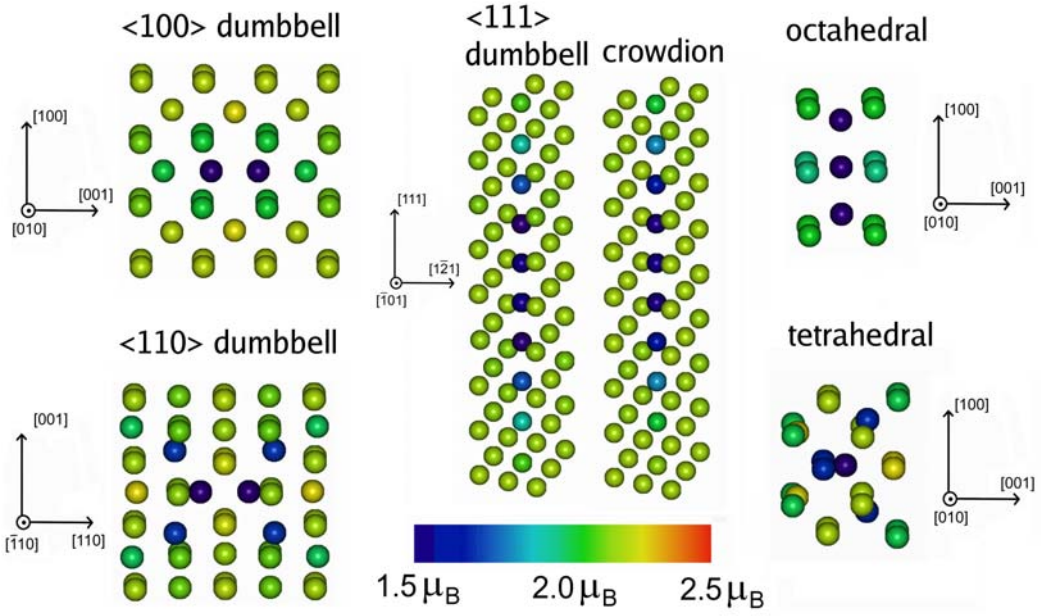

	DFT[a]	CS2	CS3-00	CS3-30	CS3-33
[110] db	-0.18	1.38	1.79	1.13	1.46
[111] nn	1.87	1.71	1.95	1.85	1.88
[11$\bar{1}$] nn	1.87	1.71	1.95	1.85	1.88
[1$\bar{1}$1] nn	2.52	2.16	2.18	2.17	2.18
[$\bar{1}$11] nn	2.52	2.16	2.18	2.17	2.18
mean	1.7	1.8	2.0	1.8	1.9
bcc	2.3	2.2	2.2	2.2	2.2

[a] data from Ref. [17]

Table 3.6: Local ferromagnetic moment on atoms in the core of the $\langle 110 \rangle$ dumbbell self-interstitial in units of μ_B. The total number of atoms in the core of the dumbbell considered in this table is ten: the two dumbbell atoms along [110], four equivalent nearest neighbors of the dumbbell along [111] and [11$\bar{1}$], and four equivalent nearest neighbors of the dumbbell along [1$\bar{1}$1] and [$\bar{1}$11] from the center of the bcc cell. The mean magnetic moment is then obtained by weighted average over the core atoms.

Figure 3.15: Local ferromagnetic moment on b=1/2[111] edge and screw dislocations. The structures have been relaxed using CS3-30. The local ferromagnetic moment is colored according to the legend, the lower value in blue correspond to $\sim$ 1.5 μ_B, the higher value in red to $\sim$ 2.5 μ_B. CS2 and the other fits of the DD potential lead to similar results.

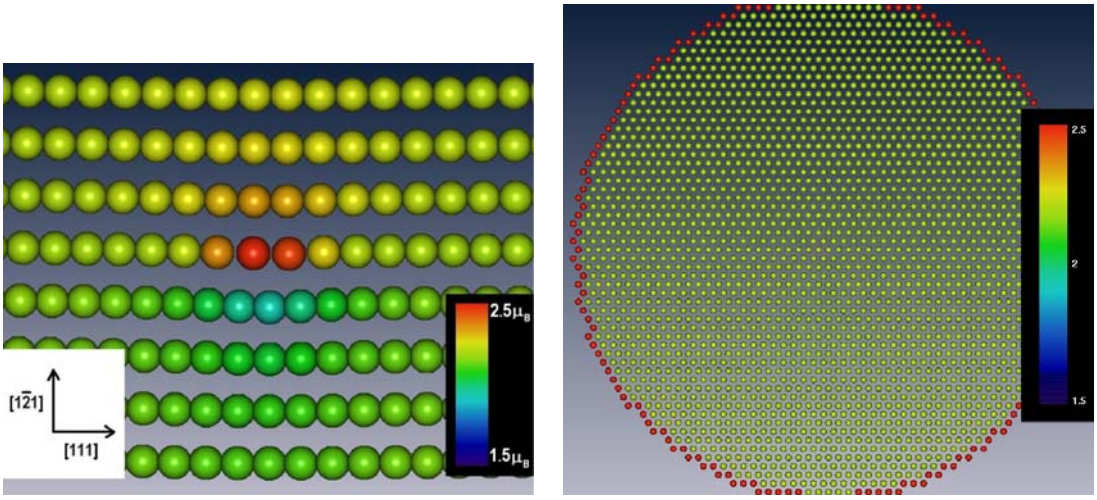

(a) (b)

Table 3.7: Optimal parameter set for CS3-00.

CS3-00		
A	18.42439658215181	
B	6.318801651265125	
Knot point	f_n	r_n^f
1	1.415806965777580	3.600000000000000
2	-3.172941853042061	3.457142857142857
3	2.518779011423245	3.314285714285715
4	1.5223391656998341E-002	3.171428571428572
5	-2.668402591084014	3.028571428571428
6	5.300933735220243	2.885714285714286
7	-6.253127207203284	2.742857142857143
8	4.354340872738243	2.600000000000000
Knot point	V_n	r_n^V
1	0.1671995832644735	3.640000000000000
2	5.748723734256789	3.457142857142857
3	1.238260767101568	3.285714285714286
4	-27.80866986307653	3.114285714285714
5	47.11807523555423	2.942857142857143
6	-27.30051838220325	2.771428571428571
7	-0.1513119116248357	2.600000000000000
8	40.00000000000000	2.500000000000000
λ_f	1.67606860	
λ_V	1.54501120	

A and B are given in eV, r_n^f and r_n^V in Å, f_n in 1/Å^5, V_n in eV/Å^5, λ_f and λ_V in 1/Å.

Table 3.8: Optimal parameter set for CS3-30.

CS3-30		
A	14.96128089567820	
B	4.754553632722176	
Knot point	f_n	r_n^f
1	2.403773687542704	3.600000000000000
2	-5.616539002612204	3.457142857142857
3	4.518414772417062	3.314285714285715
4	0.4511822086528371	3.171428571428572
5	-3.719791696378764	3.028571428571428
6	3.176870270223375	2.885714285714286
7	-0.5435529434135428	2.742857142857143
8	4.835150824080221	2.600000000000000
Knot point	V_n	r_n^V
1	4.852979304356857	3.400000000000000
2	-7.762255546111966	3.285714285714286
3	0.2118336138629596	3.171428571428571
4	-1.592481362817459	3.057142857142857
5	0.1193277971484847	2.942857142857143
6	23.52407656927417	2.828571428571429
7	-7.298957800246290	2.714285714285714
8	-1.386774762653686	2.600000000000000
λ_f	2.04390805	
λ_V	0.19900397	

A and B are given in eV, r_n^f and r_n^V in Å, f_n in 1/Å^5, V_n in eV/Å^5, λ_f and λ_V in 1/Å.

Table 3.9: Optimal parameter set for CS3-33.

CS3-33		
A	21.51448001905501	
B	8.093616756568505	
Knot point	f_n	r_n^f
1	0.5743629513080918	3.700000000000000
2	-1.856080700992208	3.516666666666667
3	2.419382074727780	3.333333333333333
4	-1.690722245925826	3.150000000000000
5	1.124207032421987	2.966666666666667
6	-0.9378621160151912	2.783333333333333
7	1.072376272490842	2.600000000000000
Knot point	V_n	r_n^V
1	3.9561191249708196E-004	4.000000000000000
2	0.7398586039192809	3.766666666666667
3	0.4779268352403156	3.533333333333333
4	-3.295383945850647	3.300000000000000
5	6.719355483414380	3.066666666666667
6	1.599123795740709	2.833333333333334
7	-5.098972177684258	2.600000000000000
8	40.00000000000000	2.500000000000000
λ_f	0.83959175	
λ_V	1.02153257	

A and B are given in eV, r_n^f and r_n^V in Å, f_n in 1/Å^5, V_n in eV/Å^5, λ_f and λ_V in 1/Å.

Chapter 4

Properties of the $b = 1/2\,[111]$ screw dislocation.

In the following we will explain in details how to construct and analyze the screw dislocation structures employed in this work. All the atomic configurations are first transformed in a convenient orthogonal system. The axis orientations and corresponding periodic vectors for the bcc lattice best suited to study the screw dislocation are as follows

$$\begin{aligned} x &\rightarrow [1\bar{2}1] \\ y &\rightarrow [10\bar{1}] \\ z &\rightarrow 1/2[111]. \end{aligned}$$

The so defined bcc supercell contains six atoms. In this supercell, the atoms lie on three (111) planes containing two atoms each, and the distance between the planes is $b/3 = \sqrt{(3)}a/6$. We will now refer to the left side of figure 4.1. This shows a projection of the bcc lattice on the (111) plane. The atoms are colored according to which (111) plane they belong to. Lets say the yellow atoms belong to the upper (111) plane (closest to the reader), the blue to the middle and the pink to the bottom plane. The right side of the figure shows a 3D view in the $[10\bar{1}]$ direction. Each bunch of atoms corresponds to a 'triangle' of [111] rows of atoms, indicated in the left side of this figure by left or right circular arrows. It can be seen that the 'Right hand bcc' structure forms an helical structure of atoms turning in the right hand sense, while the 'Left hand bcc' structure forms an helical structure of atoms turning in the left hand sense. Looking at a particular 'triangle' in the left side of the figure, the arrow is always following the sense pink-blue-yellow, that is from the bottom atomic plane to the upper atomic plane. Neighboring 'triangles' thus correspond to helical structures of atoms in the [111] direction rotating in opposite

Figure 4.1: Construction of screw dislocation cores. The left side of the figure shows a view of the bcc lattice from the [111] direction, where atoms are colored according to which (111) plane they belong, the right side a view of a 'triangle' of nearest neighboring [111] rows from the $[10\bar{1}]$ direction.

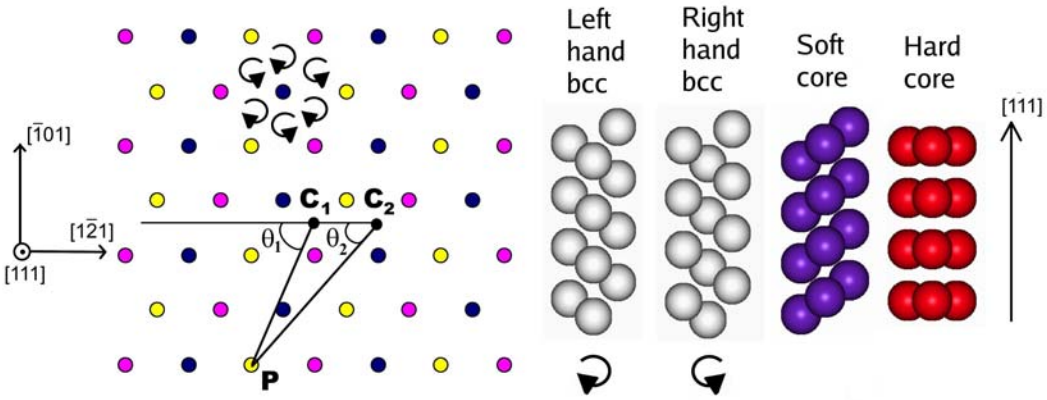

directions.

A screw dislocation with Burgers vector b=1/2[111] can be generated by shifting every atom in the positive z direction by

$$u_z(\theta_1) = \pm\frac{b}{2\pi}\theta_1 = \pm\frac{\sqrt{3}a}{4\pi}\theta_1 \tag{4.1}$$

where the dislocation line center is the point $C_1 = (C_{1,x}, C_{1,y})$ and θ_1 is the angle with the atom at $P = (P_x, P_y)$ in the xy plane. Equation (4.1) is the isotropic displacement field of a screw dislocation with Burgers vector b [58]. Isotropic elasticity is a good approximation at high distances $r_1 = \|C_1 - P\|$ from the dislocation line, that is for $r_1 \gg b$. The atoms in the region where r_1 is of the order of the Burgers vector b are however strongly distorted from the perfect lattice position and cannot be treated by the elastic approximation. The anisotropic solution for the displacement field, which is not available in analytical form, would give a better description in the intermediate range of r_1, but it will still not be sufficient for the atoms in the core. A lattice interatomic model, like EAM, Bond Order Potentials, Tight Binding or DFT are needed to find a better approximation of the minimum energy configuration in the core of the screw dislocation.

If the core center C_1 is set as in the figure, that is in the center of a 'triangle' of rows oriented like the 'Left hand bcc', the structure of the core after application of the strain field (4.1) will depend on the sign of the strain field, and results in either a so called soft (or easy) core configuration, setting $(-)$ in (4.1), or a hard core configuration, setting $(+)$ in (4.1). Of course the choice of a nearest

neighboring 'triangle' will change the helicity and thus a (+) will result in a soft core and a (−) in a hard core. In a soft core, the atoms in the 'triangle' of rows closest to the dislocation line have now opposite helicity as before and are thus strongly distorted with respect to neighboring rows. Taken alone, that is without considering the neighbor rows, the central row atoms in the soft core are still in a perfect bcc orientation, while, on the other hand, the atoms composing the central rows of the hard core are lying in the same plane, so that the absolute distance between the atoms is strongly reduced.

A very clever way of displaying the displacement field of the screw dislocation is by so called differential displacement maps[1] introduced by Vitek [78], like the one in figure 4.2. The arrows pointing between neighboring rows of atoms represent the

Figure 4.2: Differential displacement map of a non-degenerate core.

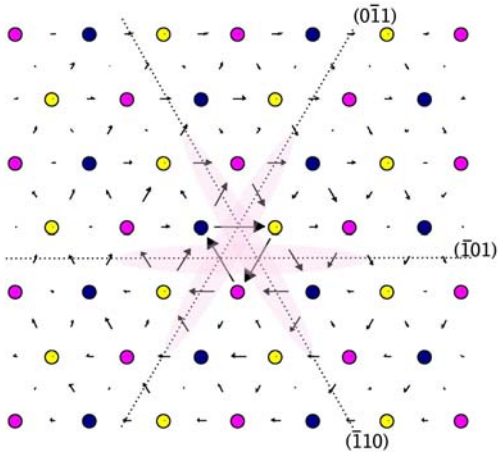

relative displacement caused by the dislocation in the [111] direction. By relative displacement it is meant the displacement caused by the dislocation with respect to the perfect bcc lattice. The perpendicular displacements correspond to the edge component of the displacement field and are usually very small compared to the screw component. The scale of the arrows is such that a displacement of $b/3$ is put equal to the side length of a 'triangle', that is $\|1/3[1\overline{2}1]\| = \sqrt{6}a/3$. The absolute direction of the arrows gives the sign of the displacement.

Energy minimization of the screw dislocation using EAM potentials can lead, depending on the potential employed, to a so called degenerate or polarized soft core structure, like the ones shown in Figure 4.3. The displacement of atomic

[1]To generate such maps we have employed the freeware software ddplot, which we have downloaded from `cnls.lanl.gov/~groger/codes/ddplot/ddplot.html` maintained by Roman Gröger.

rows in the {110} planes (or equivalently the ⟨112⟩ directions) is no longer symmetric with respect to the dislocation center. This core structure results from the displacement of the three central rows by a constant value of $b/6$, either in the positive or negative direction of the dislocations Burgers vector. As a consequence two polarized structures with the same energy exist. Other interatomic models predict that this degenerate or polarized structure is either unstable or metastable with respect to the non-degenerate (or non-polarized) structure shown in figure 4.2. Recent DFT calculations have suggested that the minimum energy configuration in all bcc transition metals, based on the analysis of the γ-surface, is non-degenerate [39], and this was confirmed by explicit structure relaxations in bcc iron [39, 47] and Mo and Ta [79]. The same result was found using the Bond Order Potentials for W and Mo [80]. The consequences of possible polarizations of the core structure on plasticity in iron is a matter of current research and debate [81]. Static calculations of the Peierls stress dependence on the direction of the applied shear stress employing EAM potentials with either a non-degenerate or a degenerate ground state core structure, lead to very different results [82]. Challenging HRTEM experimentally studies are ongoing to determine the ground state core configuration [83, 84].

Figure 4.3: Differential displacement maps of degenerate cores.

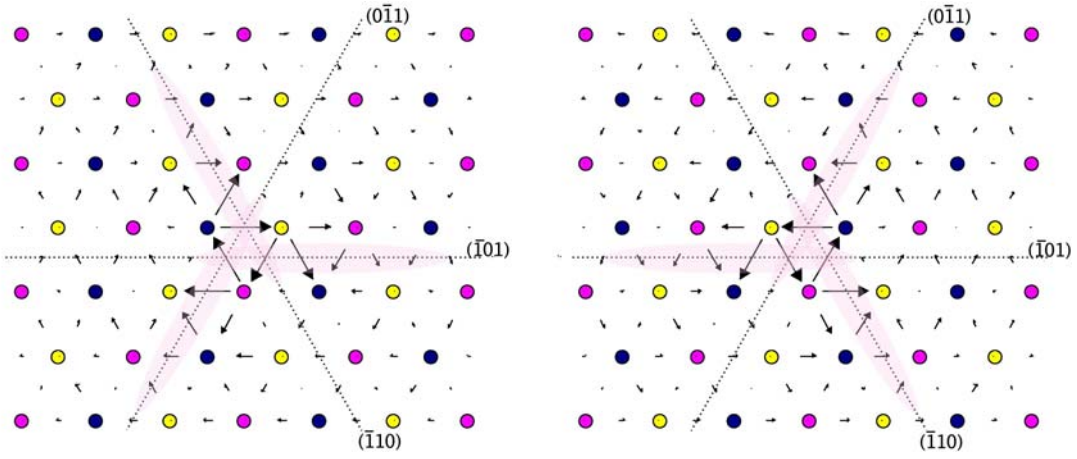

(a) (b)

4.1 Fundamental properties of the migration mechanism of the screw dislocation

The main goal of atomistic simulations of the screw dislocation is to understand its mobility laws, and more generally low temperature plasticity in bcc metals. A mobility law is basically a relation between the applied stress and the velocity of the dislocation. The research is focused on the screw dislocation, as non-screw dislocations are much more mobile, and move with an applied stress an order of magnitude lower than the screw dislocation [81]. A mobility law for bcc transition metals should depend also on the strain rate and the temperature, because of the observed strong dependence of the yield stress on strain-rate and temperature in bcc metals. A first model for the mobility of screw dislocations is due to Dorn and Rajnak [85]. This continuum model assumes that the dislocation can move by kink pair nucleation only along *one* direction. The effect of the discrete lattice on the core of the dislocation is taken into account by assuming a so called Peierls energy potential. The Peierls potential is assumed in the shape of an energy barrier between two energetically equivalent minima, akin to an inverted parabola. The activation energy for kink pair nucleation can then be calculated as a function of the applied shear stress, by assuming an isotropic line tension model, and that the dislocation bows continuously forth and back between the two minima to form a kink pair. The Peierls stress is then defined as the stress at which the kink pair formation energy is zero, or the stress required to move the dislocation at zero temperature. This model has been widely used to experimentally determine the kink pair formation energy. The kink pair formation energy so determined are scattered between 0.53 eV and 0.83 eV [85, 86, 87] for high purity α-iron. In [88] this model was extended to the case of a two dimensional Peierls potential (that is a potential surface now defined in the xy plane of figure 4.1 on page 72). The potential surface was assumed to be a simple periodical function, with minima at the soft core positions, and maxima at the hard core positions. Under an applied shear stress, the dislocation may now form kink pairs of *any* shape towards the nearest neighbor soft core configurations in the $\langle 1\overline{2}1\rangle$ directions. For an applied shear stress resulting in a force on the dislocation close to the $[1\overline{2}1]$ direction, they considered three kink pairs in the $[1\overline{2}1]$, $[2\overline{1}1]$ and $[1\overline{1}2]$ directions. The dislocation velocity is then expressed as the average over these three types of translations, weighted by the probability to thermally activate each kink pair. In spite of its simplicity, this model is a great improvement, as it incorporates the strong plastic anisotropy of the bcc lattice. This model has then been employed in a multiscale modeling approach of plastic deformation of Mo and W [89, 90, 91]. The Peierls surface has more or less the same functional form as in [88], but the parameters defining the surface are now determined by self-consistent fitting of the

Peierls stress found in atomistic calculations using Bond Order Potentials, which give a non-degenerate core structure consistent with DFT calculations. The Peierls surface does now implicitly depend on the applied stress. Because the Peierls stress is found to depend strongly on components of the applied stress *perpendicular* to the Burgers vector, the hydrostatic component of the applied stress has thus a strong effect on the core of the screw dislocation.

In this work we are limiting our investigation to some sampling of the Peierls surface at zero stresses by atomistic modeling, that is the one dimensional Peierls potential and the formation energies of kinks in the $\langle\overline{2}11\rangle$ direction, and the relative energies of different core structures. Up to now only the Ackland-Mendelev potentials were able to give a non-degenerate core structure of the screw dislocation. In this work, we have developed a method to fit the core structure, see later in section 4.2, and in the new fits of the DD potential CS3-00, CS3-30 and CS3-33 the non-degenerate core structure has lower energy than the degenerate core structure. We will see that all the EAM potentials with a very stable non-degenerate core predict however an additional minima in the (zero stress) Peierls surface. This minima corresponds to a so called split core, which can be obtained by applying the initial (unrelaxed) strain field

$$u_{\text{split}}(P) = \frac{1}{2}u_z(\theta_1) + \frac{1}{2}u_z(\theta_2) \tag{4.2}$$

where θ_1 and θ_2 are the angles as in figure 4.1, and u_z is the isotropic strain field of the screw dislocation from (4.1), see figure 4.4 for the differential displacement field of the unrelaxed and relaxed split core. We have found that very surprisingly under zero applied stress the relaxation of this structure gives the same energy as the soft core for all the potentials with a stable ground state non-degenerate core, that is Mend03, Mend04, CS3-30 and CS3-33.

4.1.1 Energy minimization of screw dislocation core structures

To investigate the core structure of the $b = 1/2\,[111]$ screw dislocation we employ a cylindrical bcc supercell at the equilibrium lattice constant a, see table 2.1 on page 25 with the symmetry axis of the cylinder oriented along the [111] direction, as in figure 4.5. The cylinder has a radius R_{cyl} of 5 nm and a height h_{cyl} corresponding to four Burger vectors b, that is $\sim$ 1 nm. The so obtained supercell contains approximately 6'576 atoms. Periodic boundary conditions are applied along the [111] direction and only the atoms within a radius R_{atom} of 4 nm from the cylinder axis are allowed to move, while the other atoms at the boundary of the cylinder are kept fixed. The soft non-degenerate and degenerate core, the hard core and the

Figure 4.4: Differential displacement map of the unrelaxed and relaxed split core.

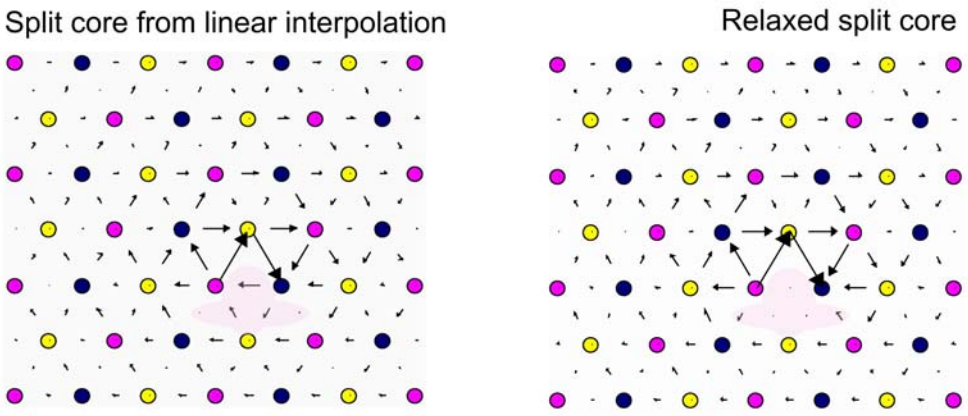

split core structures have been relaxed in this supercell. The soft and hard cores were obtained by displacing the atoms in the supercell according to the isotropic displacement field (4.1). The initial configuration for the degenerate core was obtained by relaxing the soft core using CS2, and then relaxing the so obtained configuration with another potential. The configuration of the split core is obtained by applying the displacement field (4.2) to the cylinder. These structures are then relaxed using the conjugate gradient algorithm until the force on every atom in less that 0.01 eV/Å. Figure 4.5 also shows the core structures after relaxation. The color represents the energy of the atom in eV. Only atoms with an energy of 0.05 eV bigger than the equilibrium energy E_{bcc} are shown. These are the atoms that contribute mostly in the energy difference between the structures. Atoms in blue have an energy close to E_{bcc}, and atoms in red have an excess energy of 0.2 eV or more with respect to E_{bcc}. Compared to the split and degenerate core structure, in a non-degenerate core the excess energy is more concentrated. The central rows of the hard core have an excess energy of 0.4 eV/atom. This is a general result that applies to all the potentials.

We now want to make some points on how to calculate the energy differences between these structures, which is a non trivial task, because dislocation displacement fields are long range. In our cylindrical simulation cell, the boundary atoms are fixed to the initial isotropic displacement field (4.1), and do not move during the structure relaxation. Because, however, atoms in the active region are displaced, the total energy of the boundary atoms changes after relaxation. Let us call E^{B} the *total* energy of all the atoms in the static boundary after relaxation, and E^{A} the *total* energy of all the atoms in the active region after relaxation. Even if the boundary atoms are fixed, the energy of the boundary is changing during

Figure 4.5: Construction of the cylinder supercell for the screw dislocation.

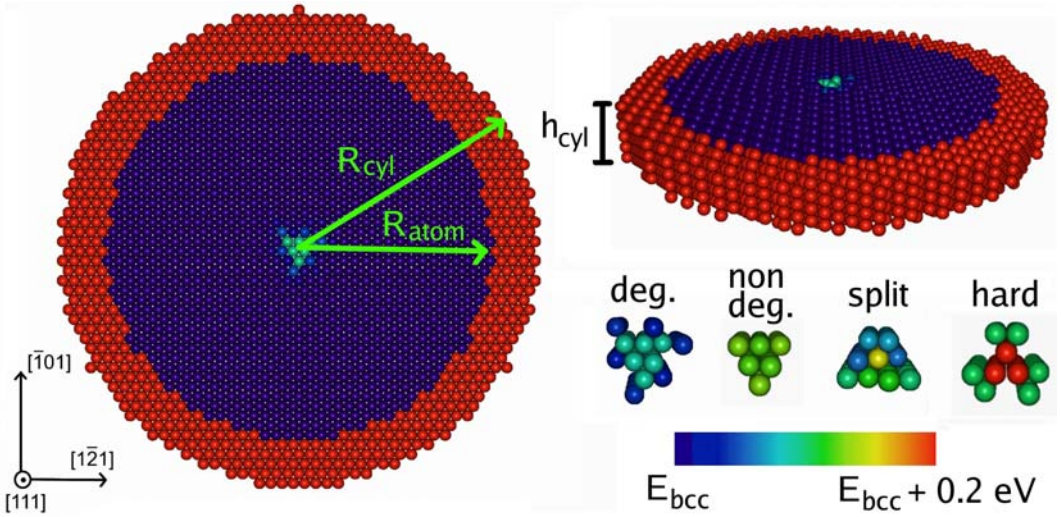

the relaxation, because atoms in the active region and *close* to the boundary are displaced. For the soft and hard cores, the boundary atoms are fixed to exactly the same positions, corresponding to the isotropic displacement field (4.1). The boundary energy difference between the two core structures is thus zero before relaxation. We consider the energy difference $E_1^{\mathrm{B}} - E_2^{\mathrm{B}}$ between the boundaries of the two core structure as the absolute error in the energy difference between the two core structures given by $E_1^{\mathrm{A}} - E_2^{\mathrm{A}}$. For the split core the situation is different, as the initial displacement field is not exactly the same as for the soft or hard core, thus also the displacement of the boundary atoms is not exactly the same. The error $E_1^{\mathrm{B}} - E_2^{\mathrm{B}}$ was anyhow always found to be $\lesssim 10$ % of $E_1^{\mathrm{A}} - E_2^{\mathrm{A}}$. Another problem is that the total energy of the system, typically ~ 5 eV per atom, or ~ 5'000 eV/b for a cylinder radius of ~ 5 nm, is much bigger than the energy differences between the structures, typically of the order of 0.1 eV/b. Thus, increasing the radius of the cylinder too much will inevitably cause numerical problems. A way to improve the precision of this calculation would be to use the anisotropic displacement field and so called flexible boundary condition to couple the boundary atoms with an elastic continuum.

Table 4.1 gives the so computed energy differences between dislocation structures. Sometimes the structure is unstable with respect to the conjugate gradient relaxation. The first column gives the energy difference between the non-degenerate and the degenerate core structure and the second column the difference between the hard core configuration and the ground state soft core structure. As explained before, we estimate an error of at least 0.01 eV/b. We note that potentials with a deep hump in the single string potential have generally stable

Table 4.1: Energy differences between core structures of the screw dislocation in eV/b. The first column gives the energy difference between the degenerate and non-degenerate core, in case they are both (meta-)stable, and the second column the energy difference between the hard and ground state soft core, in case they are both (meta-)stable. It is indicated whether some structures are unstable by the conjugate gradient algorithm.

	$E_{\text{deg}} - E_{\text{non-deg}}$	$E_{\text{hard}} - E_{\text{soft}}$
CS2	non-deg unst.	0.14
CS3-00	0.01	0.17
CS3-30	0.07	0.21
CS3-33	deg unst.	hard unst.
Mend04	deg unst.	hard unst.
ABO	-0.39	0.44
DFT	deg unst.	0.02-0.03[a]

[a] from [92]

non-degenerate cores, the only exception is CS3-00, where the two core structures have almost the same energy. CS2 and ABO, on the other hand, clearly favor a degenerate core structure, see figure 2.2 on page 27, and later in section 4.2 for more details. It is interesting to note that CS2, CS3-30, CS3-33 and ABO overestimate the hard to soft core energy difference from DFT by an order of magnitude and we mention again that, for potentials with a stable non-degenerate core, the split core has, within the error of the calculation method, the same energy as the non-degenerate core.

Although DFT is a more accurate description of interatomic bonding, and an accurate description *is needed* since the energy differences between the structures are very small, it is nevertheless limited to small simulation cells, which, if not a major problem for localized defects like self-interstitial, needs proper treatment for extended defects like the screw dislocation. The main drawback of a cylindrical supercell containing a single screw dislocation is that in DFT one cannot separate the energy contribution of the dislocation from the energy contribution of the surface, because DFT only gives the *total* energy of the system. To create a fully periodic supercell, one has to include pairs of screw dislocations, a so called dipole, with opposite Burgers vector, so that the total Burgers vector in the supercell is zero, but a dipole is inherently a metastable configuration, as dislocations with opposite Burgers vector tend to attract and annihilate. Another drawback is that, because the dislocations are very close to each other in a typical DFT supercell containing 100-200 atoms, an analysis based on anisotropic elasticity theory is necessary to estimate the interaction energy of the periodic array of screw dislocations. For instance, the hard to soft core energy difference calculated in the periodic dipole

configuration using DFT was found to strongly depend on the dipole arrangement, as many two dimensional array configurations of screw dislocations are possible. A correction based on anisotropic elasticity recently produced a converged value for the hard to soft energy difference [92], which is given in table 4.1. Note however that the core energy itself may be a very sensitive function of the applied local stress, and this can probably not be investigated using anisotropic elasticity.

4.1.2 The Peierls potential in the $\langle\overline{2}11\rangle$ directions

The $\langle\overline{2}11]\rangle$ Peierls potential can be defined as the minimum energy path at zero temperature and stress to move the dislocation line from two equivalent soft core configurations in the $[\overline{2}11]$ direction, or, referring to figure 4.1 on page 72, from a soft core centered at C_1 to a soft core at C_2, without the formation of any kink on the dislocation line. For simplicity[2], we only calculate the Peierls potential using semi-empirical potentials with ground state non-degenerate cores, that is CS3-00, CS3-30, CS3-33 and Mend04 (Mend03 is expected to give very similar results). To calculate the minimum energy path between the two equivalent soft cores we have used the NEB method [93], using the improved tangent estimate technique as described in [94]. In the NEB method, the transition path is defined as a set of $N_{\rm im}$ configurations, so called 'images' of the system. An initial guess for the transition path is given by a linear interpolation between the displacement fields of the two soft cores centered at C_1 and C_2. The displacement of atom P in the 'image' number n is thus initially given by

$$u_n(P) = u_1(P)(1 - \frac{n}{N_{\rm im}}) + u_2(P)(\frac{n}{N_{\rm im}}) \tag{4.3}$$

where u_1 and u_2 are the isotropic displacement fields for the screw dislocation centered respectively at C_1 and C_2, see figure 4.1 on page 72, and $n = 0, \ldots, N_{\rm im}$. If the atoms in every 'image' configuration would be allowed to relax, then every 'image' would relax to some local minima, as for instance a soft core at C_1 or a soft core at C_2. The trick in the NEB method is to link the 'image' configurations together by means of penalty functions by defining a distance between 'image' configurations, as to prevents them to relax to the initial or final configurations.

To calculate the $\langle\overline{2}11\rangle$ Peierls barrier by the NEB method we have used the same cylindrical supercells as in subsection 4.1.1, and also in this case the change in total energy of the boundary atoms along the path was very small. The Peierls potential of the semi empirical potentials calculated in this work and the DFT calculation

[2]The calculation of the Peierls barrier with an interatomic model giving a degenerate core structure is slightly more complicated, because one should consider both transition paths between the same polarizations and transition paths between opposite polarizations.

Figure 4.6: The $\langle \bar{2}11 \rangle$ Peierls potential (left figure) and typical core structures encountered along the transition path when using EAM potentials with very stable non-degenerate cores, that is CS3-30, CS3-33 and the Ackland-Mendelev potentials (right figure).

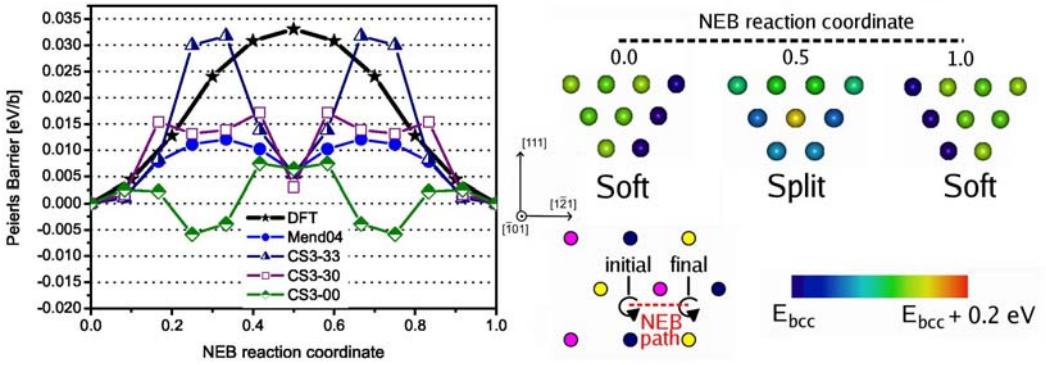

calculated in [47] are shown in figure 4.6. There is a qualitative difference between the DFT potential, which has a single hump shape [47], and the potential of the semi empirical potentials, which have a double hump shape. Inspection of the midway configuration reveals it to be the split core, when considering the semi empirical potentials, but the midway configuration from DFT was found to be more similar to the hard core configuration [47]. The barrier of CS3-00 reveals that the non-degenerate soft core configuration is unstable, which can be readily attributed to the small energy difference between the degenerate and the non-degenerate core structures for CS3-00, compared to the other potentials, see table 4.1 on page 79. The core structure corresponding to the minimum of the Peierls potential of CS3-00 can be identified as a sort of merged structure between a non-degenerate and a degenerate core. Although all the new fits have a very similar single string potential, see figure 2.2 on page 27, which favors the non-degenerate structure, the $\langle 2\bar{1}\bar{1} \rangle$ Peierls potentials are very different from each other, thus it seems to be no correlation between the single string potential, and the height of the Peierls potential. The main common feature is the split core configuration, which is not only a feature of Mend03, Mend04, CS3-30 and CS3-33, but of all the fits of the DD potentials with non-degenerate core structure and acceptable bulk and point defect properties as generate by the optimization algorithm. An analysis within the multi string Frenkel-Kontorova model suggests that this may be due to the relatively short range of the interactions in semi empirical potentials compared to DFT [63].

To check the effect of the boundary conditions in the DFT calculation, the soft cores were first relaxed, either on a cluster, akin to our cylinder and periodic

in one direction, or on a fully periodic dipole supercell, and the difference in the transition path between these two settings is of the order of 0.005 eV/b [47]. The Peierls potential was calculated with the drag method, where the atoms in every 'image' configuration are constrained to move in an hyperplane perpendicular to the initial path, but this is not a serious constrain, as it was found that, using the Ackland-Mendelev potential, the NEB and the drag method give very similar results. Also note that the midway configuration has been found to be similar to an hard core configuration, thus the energy should be corrected to account for anisotropic effects, as in the case of the DFT calculation of the hard to soft core energy difference [92], see also subsection 4.1.1.

4.1.3 Kinks in the $\langle\overline{2}11\rangle$ directions

A kink is defined as a step in the dislocation line in its glide plane. A *kink pair* is formed by two equal steps but in opposite directions. The two kinks in a kink pair are not equivalent because of symmetry breaking [95], and are referred to as right (or vacancy) kink and left (or interstitial) kink, see figure 4.7 and figure 4.8 on page 85. Kinks can be characterized by a kink height h_K and a kink length l_K, as in the figures. The screw dislocation is believed to migrate by the nucleation of kink pairs between energetically equivalent core structures, the kinks then migrate very fast along the dislocation line, resulting in the net movement of the dislocation by h_K. In the screw dislocation, in principle kinks can form in every direction, since the dislocation can glide in any plane containing its line. For instance kinks may also form in the $\langle\overline{2}11\rangle$ directions across the hard core configuration [96]. The kink pair formation energy is however proportional to the height h_K, so that in general short kinks are favored, this is the reason why we will limit ourselves to kinks in the $\langle\overline{2}11\rangle$ direction, as the goal here is to compare the semi-empirical potentials, rather than to investigate the dislocation mobility. In previous atomistic studies, kinks have always been assumed to form between equivalent soft core structures, that is, referring to figure 4.1 on page 72, between a soft core at C_1 and a soft core at C_2 with a kink height of $h_K = 2\sqrt{2}b/3$ [97, 96]. Yet, ignoring the DFT results, the fact that the split core configuration and the non-degenerate core are energetically equivalent suggests an alternative mechanism of migration, that is by the nucleation of double kinks from the soft core to the split core, with a kink height of $h_K = \sqrt{2}b/3$. This mechanisms has been indeed observed in MD simulations [82, 98] using Mend04. Although the split core was found to be systematically unstable in the molecular dynamic simulation, so that just after nucleation of one half height double kink, another half height double kink in the same direction was nucleated, shifting the dislocation line segment in the nearest neighbor soft core configuration along the $\langle\overline{2}11\rangle$ direction, it may not be excluded that at lower

stresses, strain rates or temperatures the split core may be more stable in molecular dynamic simulations.

Kink pair in the $\langle\overline{2}11\rangle$ directions and of full height, $h_K = 2\sqrt{2}b/3$

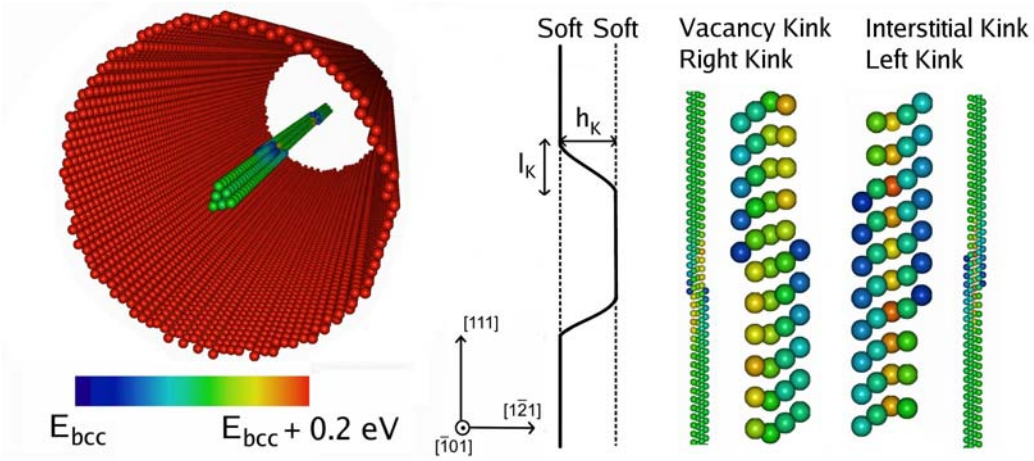

Figure 4.7: Construction of kink pairs in a cylinder supercell. The left figure is the cylinder supercell containing a double kink, where only atoms with an energy bigger than E_{bcc}+0.05 eV are shown. In the right picture a detail of the two different kinks composing the kink pair viewed from the $[10\overline{1}]$ direction.

A kink pair can be studied in the same type of cylindrical supercell as before, see subsection 4.1.1 and figure 4.7. The double kink was created by applying the isotropic displacement field of the screw dislocation (4.1). In the upper half of the cylinder ($z > 0$), the dislocation line center was shifted by $h_K = 2\sqrt{2}b/3$ along $\langle\overline{2}11\rangle$ with respect to the dislocation line center in the lower half of the cylinder ($z < 0$). The dislocation line in the lower half is set at the center of the cylinder: the two kinks are thus separated by a distance of half the cylinder height, $h_{\mathrm{cyl}}/2$. Because kinks are interacting in the direction of the dislocation line, to get converged values the height of the cylinder h_{cyl} must be at least 80 b [96]. In the same cylinder we also relax a screw dislocation without kinks. The kink pair formation energy is then calculated as the total energy difference (calculated without boundary atoms, see subsection 4.1.1 on page 76) between the dislocation with a kink pair and the straight dislocation. As in the case of the energy difference between the soft and the split core, the displacement field of the boundary atoms is *not* the same for the straight and kinked dislocations, but in this case the misfit is extended to 40 b in the dislocation line direction. Considering a typical energy difference of 0.01 eV/b due to the misfit, this gives rise to a total energy difference

between the boundary atoms of the order of 0.4 eV. It is thus necessary to check the convergence of the kink pair formation energy, and for this we employ cylinders of different radii and height as in table 4.2. We see in the left side of figure 4.9 that although the energy difference in the boundary atoms is slowly converging, the formation energy of the kink pair is actually converged, with small fluctuations that are probably due to the high numerical precision required: an error of 0.01 eV in the kink pair formation energy corresponds to the same accuracy in the *total* energy, which means that the energy per atom must be determined with a precision of typically 1 μeV.

	R_{atom} (nm)	R_{cyl} (nm)	h_{cyl}	n_{atom}
1	3	4	80 b	84640
2	4	5	80 b	132560
3	5	6	80 b	190640
4	6	7	80 b	260080
5	4	5	100 b	165700

Table 4.2: The five cylinder supercell configurations employed for convergence test of the kink pair formation energy.

Kink pair in the $\langle 1\bar{2}1\rangle$ directions and of half height, $h_K = \sqrt{2}b/3$

A kink pair between the soft core configuration and the split core configuration can be studied in the same type of cylindrical supercell as before, see subsection 4.1.1 and figure 4.8. In the upper half of the cylinder ($z > 0$), we apply the displacement field of a split core (4.2). The kink pair formation energy is then calculated as before, employing the cylinders in table 4.2 to check convergence, see also the right side of figure 4.9. The kink pair formation energies, both half and full height, calculated using CS3-00 are not converging, which is very likely due to the fact that in this case the non-degenerate core structure is actually not the ground state configuration.

The kink pair formation energy is proportional to the height of the Peierls potential, see figure 4.6 on page 81. The potential with the biggest barrier, CS3-33, has also the biggest kink pair formation energy. The kink pair formation energy is also clearly proportional to the height of the kink, where the formation energy of the half height kink pair is approximately half the formation energy of the full height double kink. In general, we see that the results strongly depend on fine details of the interatomic interactions.

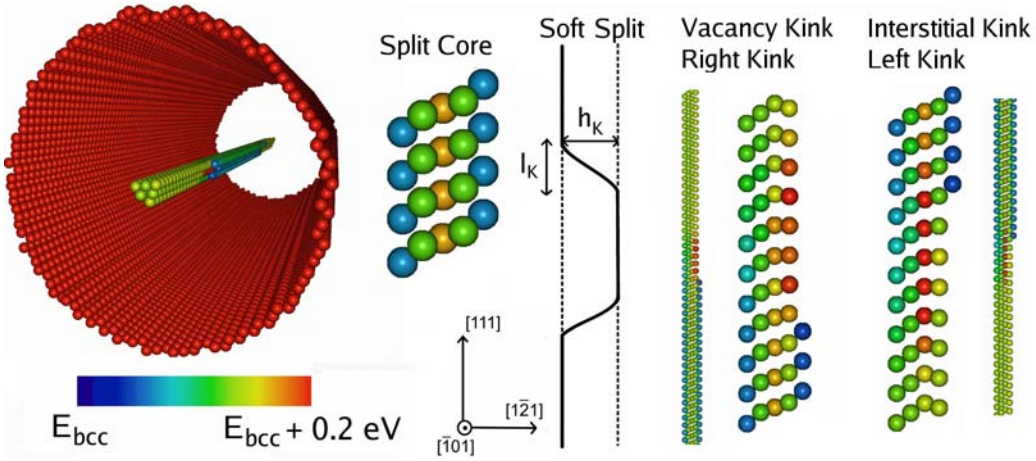

Figure 4.8: Construction of kink pairs of half height in a cylinder supercell. The left figure is the cylinder supercell containing a double kink of half height, where only atoms with an energy bigger than E_{bcc}+0.05 eV are shown. In the right picture a detail of the two different kinks composing the kink pair of half height viewed from the $[10\bar{1}]$ direction.

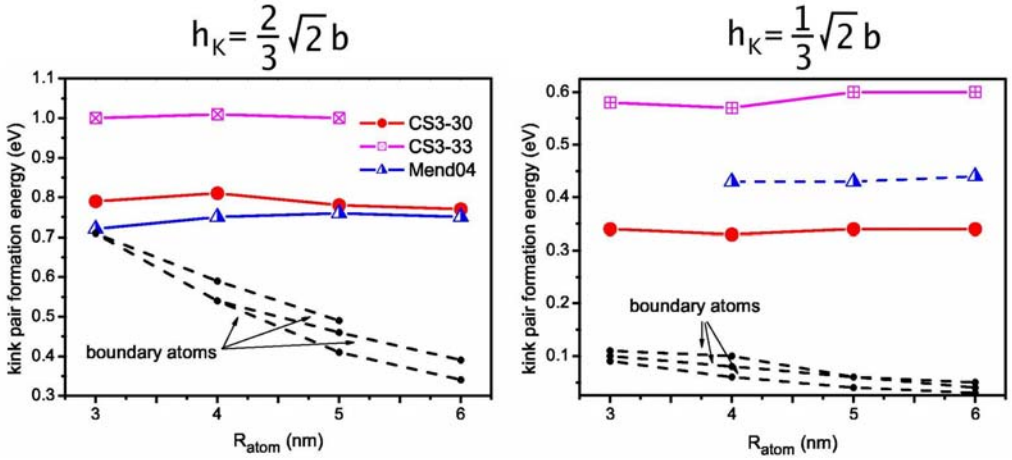

Figure 4.9: Convergence of kink pairs formation energies of full height, left figure, or half height, right figure, as a function of the cylinder radius R_{atom}. The total energy difference between the boundary atoms of the supercell with a kinked screw dislocation and of the supercell with a perfect screw are also shown.

Single kinks in the $\langle 1\bar{2}1\rangle$ directions and of full height, $h_K = 2\sqrt{2}b/3$

It is interesting to investigate the influence of the boundary conditions on the kink formation energies. In the following we will thus construct a fully periodic quadrupolar screw dislocation arrangement following [47], and then apply the method developed in [99] to calculate the formation energies of *single* kinks.

We will now refer to figure 4.10 to explain how we have constructed the quadrupole. As in figure 4.1 on page 72 the unit cell contains 6 atoms, with periodic vectors

$$\begin{aligned} \overrightarrow{x} &= [1\bar{2}1] \\ \overrightarrow{y} &= [10\bar{1}] \\ \overrightarrow{z} &= 1/2[111]. \end{aligned}$$

The first step to set up a screw dislocation dipole is to cut a supercell with periodic vectors

$$\begin{aligned} \overrightarrow{C_1} &= (2m_x+1)\,\overrightarrow{x} \\ \overrightarrow{C_2} &= (2m_x+1)/2\,\overrightarrow{x} \quad +(2m_y+1)/2\,\overrightarrow{y} \\ \overrightarrow{C_3} &= m_z\,\overrightarrow{z}, \end{aligned}$$

where m_x,m_y and m_z are integer numbers. $\overrightarrow{C_2}$ is actually a periodic vector of the bcc lattice, as can be easily checked. As shown in figure 4.10, it is now possible to set two dislocation centers separated by $\overrightarrow{C_1}/2$, such that one center corresponds to a 'Left handed bcc' (∇), and the other center to a 'Right handed bcc' (Δ). Applying now a negative isotropic strain field to the 'Left handed bcc', that is (4.1) on page 72 with $(-)$, and a positive isotropic strain field to the 'Right handed bcc', that is (4.1) with $(+)$, we can create two soft core dislocations with opposite Burgers vector in the same supercell, so that the net Burgers vector is zero. The so created periodic structure corresponds to a rectangular array of screw dislocations, where next nearest neighbor dislocations have opposite sign, see the left hand side of the figure. The dimensions in the array are

$$\begin{aligned} d_x &= \frac{2m_x+1}{2}\sqrt{6}a \\ d_y &= \frac{2m_y+1}{2}\sqrt{2}a, \end{aligned}$$

and the values for m_x and m_y must be chosen in such a way as to make the array as close as possible to a square. Following [100] and [47], we add a tilt component

Figure 4.10: Construction of a dipole of screw dislocations in the quadrupolar periodic arrangement. The left side of the figure shows a view of the bcc lattice from the [111] direction, where atoms are colored according to which (111) plane they belong. Also shown is the position of the two easy cores with opposite Burgers vector and the shape of the dipole supercell with zero total Burgers vector. On the right side we show how the dipole supercell generates a quadrupolar periodic arrangement of screw dislocations by applying periodicity.

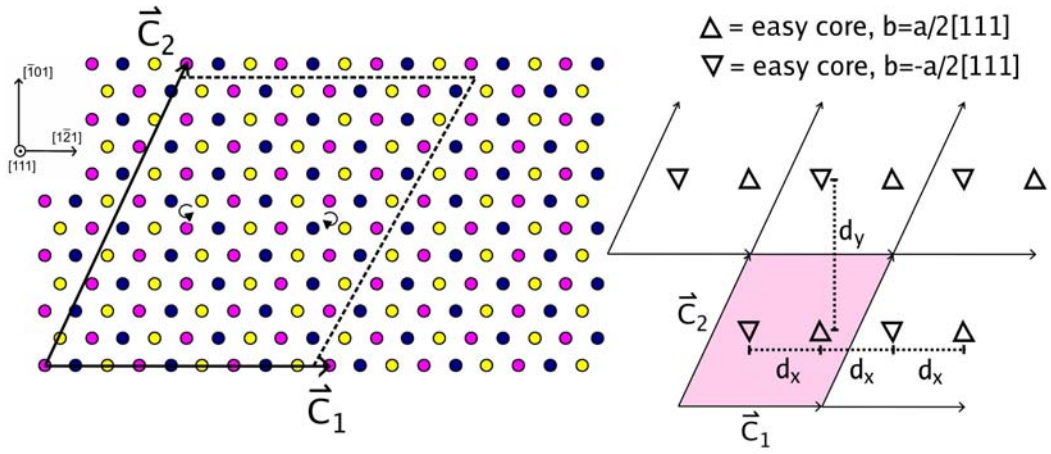

to the supercell, and define the new supercell vectors

$$\begin{aligned}\widetilde{\overrightarrow{C_1}} &= \overrightarrow{C_1} \\ \widetilde{\overrightarrow{C_2}} &= \overrightarrow{C_2} + 1/2\overrightarrow{z} \\ \widetilde{\overrightarrow{C_3}} &= \overrightarrow{C_3}.\end{aligned}$$

The component along the Burgers vector direction is added in order to set the *mean* plastic strain in the supercell introduced by the dipole to zero. This helps stabilizing the structure so that the two dislocations do not annihilate, as in this way the local stress acting on the dislocation cores is set to zero [101]. A supercell containing a dipole and relaxed using CS3-33 is shown in the left side of figure 4.11, where the atoms are colored according to their potential energy. It is not trivial to add a single kink because the kink vector $\pm 1/3\overrightarrow{x}$ is not a periodic vector of the bcc lattice. However the vectors

$$\begin{aligned}\overrightarrow{K_{\mathrm{R}}} &= 1/3\overrightarrow{x} - 2/3\overrightarrow{z} = a\,(0,-1,0) \\ \overrightarrow{K_{\mathrm{L}}} &= -1/3\overrightarrow{x} - 1/3\overrightarrow{z} = a\,(-1/2,1/2,-1/2)\,,\end{aligned}$$

Figure 4.11: Construction of single kinks. The left figure shows one of the relaxed dipole supercells containing two perfect screw dislocations employed in this work. Atoms are colored according to their energy as in figure 4.8. In the right side a detail of the two different kinks viewed from the $[10\overline{1}]$ direction, as obtained by adding $\overrightarrow{K_{\mathrm{R}}}$ or $\overrightarrow{K_{\mathrm{L}}}$ to $\widetilde{\overrightarrow{C_3}}$.

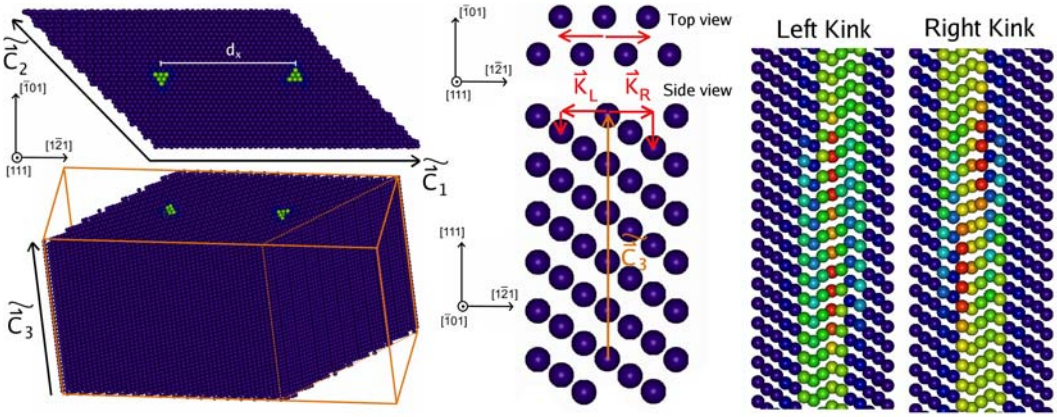

are periodic vectors of the perfect lattice, and can be thus added to the supercell vectors without creating any further defects. It is thus possible to create single kinks by simply adding $\overrightarrow{K_{\mathrm{R}}}$ or $\overrightarrow{K_{\mathrm{L}}}$ to $\widetilde{\overrightarrow{C_3}}$. These new periodic vectors define a supercell containing a different number of atoms than the dipole supercell with no kinks, and it is thus necessary to add or remove one (111) layer of atoms [99], or equivalently remove or add two (111) layer of atoms. In the right side of figure 4.11 we show the left and right kinks that we have constructed following this recipe.

The convergence on supercell size of the single kinks formation energies has been studied in [99] to explore the feasibility of DFT calculations of the single kinks formation energies, which is challenging, as for small supercells the convergence is slow. Here we consider only supercells which are big enough to give converged results. We check anyhow convergence by calculating the single kinks formation energies on three different supercells, as we vary the distance between the dislocations in the xy-plane and height of the supercell in the Burgers vector direction. The same considerations as for the calculation of formation energies in the cylinder supercell apply, in particular we note that because of the great number of atoms and the small energy considered, a precision of the order of 1 μeV per atom is required. The kink formation energies discussed in this subsection are summarized in table A.1.

The first important fact already noted in [99] is that the (full height) single kink formation energies of all the semi-empirical potentials with ground state non-degenerate cores are asymmetric, with formation energies for the vacancy single

Table 4.3: The three dipole configurations employed for convergence test of the single kinks formation energies.

	m_x	m_y	m_z	d_x (nm)	d_y (nm)	n_{atoms} dipole	left kink	right kink
1	17	31	40	12.29	12.77	63240	62186	62713
2	17	31	60	12.29	12.77	94860	93806	94333
3	27	47	40	19.31	19.26	152280	149742	151011

kink that may be as low as 0.1 eV, and much higher formation energies for the interstitial single kink. Moreover the sum of the vacancy and interstitial full height single kinks formation energies is not exactly equal to the full height double kink formation energies for any of the semi-empirical potentials. For Mend04, our result exactly agrees with previously published results, where the sum of the single kink formation energies was found to be 0.65 eV, and the double kink formation energy was found to be 0.75 eV, see [12]. Our calculation is thus validated. The discrepancy between the direct calculation of the double kink formation energy for a screw dislocation in a cylinder and the value calculated by summing the single kinks formation energies for a screw dislocation in a periodic dipole configuration may be related to the long range displacement field of the screw dislocation, in particular to the interaction of the dislocation with the cylinder surface or with its periodic images in the quadrupolar array.

We hope that the selection of potentials presented here, with different heights and "flavors" of the Peierls barrier, may be useful to further investigate the migration mechanism of the screw dislocation.

	single kinks			double kinks	
	interstitial	vacancy	int + vac	full height	half height
CS3-30	0.57	0.19	0.76	0.77	0.34
CS3-33	0.65	0.28	0.93	1.00	0.60
Mend04	0.57	0.08	0.65	0.75	0.44

Table 4.4: Summary of kink formation energies in eV. The single kinks are of full height and are calculated in the dipole supercell, that is with full periodic boundary conditions, and the double kinks are calculated in the cylinder supercell, that is with periodic boundary conditions only along the dislocation line. The sum of interstitial and vacancy single kinks formation energies calculated in the dipole is not equal to the double kink formation energy of full height calculated in the cylinder.

4.2 Suzuki-Takeuchi model for the core structure of the screw dislocation

In this section we analyze the structure of the soft core within the Suzuki-Takeuchi model [102], which is a one dimensional model where the [111] atomic rows are allowed to move only in the [111] direction. The model makes the following assumptions:

1. string or rows of atoms can move in the [111] direction, but are fixed in the $\{111\}$ plane. Each string i is thus solely characterized by its position z_i along the [111] direction. This assumption is justified for the 1/2[111] screw dislocation, because the edge component is negligible.

2. The strings are rigid, that is the distance between atoms in each string is the same as in the perfect lattice. This assumption is justified for a perfect line dislocation without any impurities in the core and under zero applied stress.

3. The energy of the system is determined by a pairwise interaction between nearest neighbor strings. Let the displacement of string i be given by

$$z_i = z_i^{\mathrm{bcc}} + s_i, \tag{4.4}$$

where z_i^{bcc} is the position of the string in the perfect lattice and s_i is an additional displacement. The energy of strings $i = 1, \ldots, N$ is then given by

$$E_{\mathrm{str}}(1, \ldots, N) = \frac{1}{2} \sum_{\substack{i=1,\ldots,N \\ j \text{ n.n. of } i}} U\left(z_i - z_j\right). \tag{4.5}$$

The function U defining the inter string interaction is a periodic function with a period given by the Burgers vector b of the 1/2[111] screw dislocation, because of this it is appropriate to measure U in units of eV/b.

This assumption is also appropriate for the EAM potentials considered in this thesis: the embedding function on atom k can indeed be expanded as

$$F(\rho_k) \simeq F(\rho_0) + F^{(1)}(\rho_0)(\rho_k - \rho_0). \tag{4.6}$$

where ρ_0 is a reference density, which may be taken for example as the density in the perfect lattice, and the expansion is valid in the limit that ρ_k is close to this reference value, and this is actually the case for a screw dislocation

described by EAM potentials. The reason for this is that in a soft core screw dislocation the local hydrostatic pressure distribution is almost the same as in the perfect lattice. A pairwise interaction law thus seems appropriate at least for the EAM potentials, because the *minimum* distance to the atoms in a next nearest neighbor string is $\sqrt{2}a \sim 4.05$ Å, that is the third neighbor distance in the perfect bcc lattice, and as can be see in figure 3.1 on page 34, the interaction at this distance is very small for the EAM potentials.

It is then possible to extract the inter string interaction U as follows. Take a perfect bcc lattice and displace only one string, that is

$$z_1 = z_1^{\text{bcc}} + s \tag{4.7}$$
$$z_j = z_j^{\text{bcc}} \text{ for } j \neq 1. \tag{4.8}$$

Because three of the nearest neighbor string are displaced by $+1/3b$ with respect to string number 1, and the other three nearest neighbor strings are displaced by $-1/3b$, the energy change from the perfect lattice is given by

$$\sigma(s) = E_{\text{str}} - E_{\text{str, bcc}} = 3U(1/3b + s) + 3U(-1/3b + s) + U_0, \tag{4.9}$$

where $U_0 = -3(U(1/3b) + U(-1/3b))$ is a constant, which we can set to zero for simplicity. We call $\sigma(s)$ the single string potential. By employing the periodicity of U it is easy to show that

$$\sigma(s + 1/3b) = 3U(-1/3b + s) + 3U(s), \tag{4.10}$$
$$\sigma(s - 1/3b) = 3U(1/3b + s) + 3U(s), \tag{4.11}$$

and thus, by combining with the previous equation,

$$U(s) = \frac{1}{6}\left(\sigma(s + 1/3b) + \sigma(s - 1/3b) - \sigma(s)\right). \tag{4.12}$$

The inter string interaction derived in this way from DFT was applied to the study of solid solution softening or hardening [103, 104], by investigating how the interstring interaction is affected by the presence of solute atom impurities.

In the right side of figure 4.12 we show how we have calculated the single string potential $\sigma(s)$ with the EAM potentials. In the left side we show typical shapes of the single string potential, that is either with a single or double hump structure. We characterize the shape of the single string potential $\sigma(s)$ by its curvature at $s = 1/2b$,

$$C_\sigma^{1/2} = \left.\frac{\partial^2 \sigma(s)}{\partial s^2}\right|_{s=1/2b} \tag{4.13}$$

Figure 4.12: Construction of the single string potential. As shown in the right side a single [111] row of atoms is displaced along the [111] direction, the single string potential $\sigma(d)$ is the given by the unrelaxed energy per atom in the string normalized so that $\sigma(0) = 0$. The left side shows typical shapes of $\sigma(d)$, either a single hump with negative curvature $C_\sigma^{1/2} < 0$, or a double hump with positive curvature $C_\sigma^{1/2} > 0$.

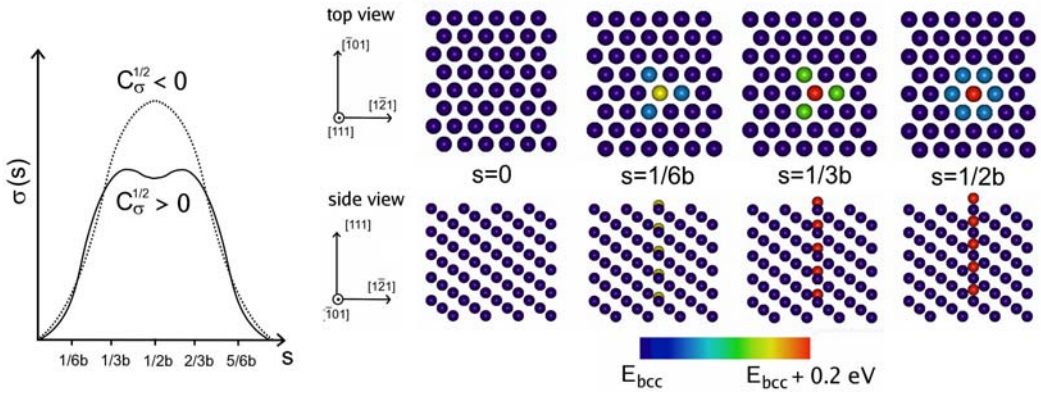

A negative curvature is associated with a single hump potential, and a positive curvature with a double hump potential. In [64] we have shown that whether an EAM interatomic potential predicts a degenerate or non-degenerate core structure is related to $C_\sigma^{1/2}$. To show this we have employed *all* the fits generated within the optimization of the DD potential. For each fit, we determine the structure of the 1/2[111] screw dislocation by relaxing a non-degenerate and a degenerate core structure in the same cylinder supercell as in section 4.1.1 on page 76. Depending on the fit, the non-degenerate core may be stable and the degenerate core unstable, or the non-degenerate core may be unstable and the degenerate core stable, or both may be stable. In the last case we determine which structure is the ground state by calculating the energy difference, as in section 4.1.1. For each fit we have also calculated the curvature of the string potential $C_\sigma^{1/2}$. The result is shown in figure 4.13. In the left side we see that most of the fits have a negative curvature and a positive curvature clearly favors a non-degenerate core structure. The right side of the figure shows the same data but in terms of the probability that, given a fit with a curvature $C_\sigma^{1/2}$, the ground state core structure be degenerate or non-degenerate. For negative curvatures between -30 eV/b^2 and -20 eV/b^2 there is a high probability to get a degenerate core structure, and for positive curvatures between 0 eV/b^2 and 30 eV/b^2 there is a high probability to get a non-degenerate core structure. We have found, however, no correlation between the curvature and the *energy difference* between the structures.

Figure 4.13: Correlation between single string potential and core structure. The left figure shows frequency counts for all the fits generated in this work for the occurrence of a ground state degenerate or non-degenerate core structure of the 1/2[111] screw dislocation as a function of the curvature of the single string potential $C_\sigma^{1/2}$. The right figure gives the corresponding probability that a given fit have a ground state degenerate or non-degenerate core structure as a function of $C_\sigma^{1/2}$.

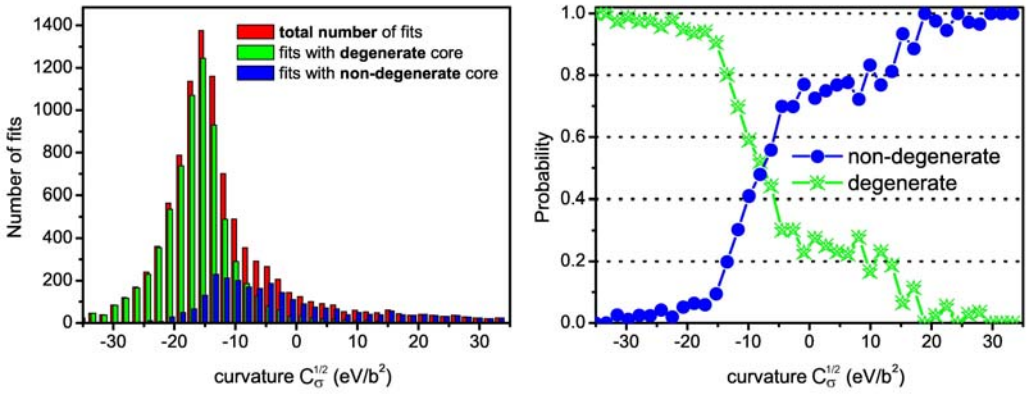

In the following, we will link the curvature $C_\sigma^{1/2}$ to an instability in the non-degenerate core structure. We will now refer to figure 4.14, which shows the displacement field of a non-degenerate and of a degenerate core. The position of the central rows in the perfect lattice is given by

$$z_{\mathrm{I}}^{\mathrm{bcc}} = 0, \tag{4.14}$$

$$z_{\mathrm{II}}^{\mathrm{bcc}} = +\frac{1}{3}b, \tag{4.15}$$

$$z_{\mathrm{III}}^{\mathrm{bcc}} = -\frac{1}{3}b. \tag{4.16}$$

Application of the isotropic strain field of the screw dislocation (4.1) on page 72 with $(-)$ generates a soft core dislocation. The position of the strings then becomes

$$z_{\mathrm{I}}^{\mathrm{iso}} = -\frac{1}{4}b \tag{4.17}$$

$$z_{\mathrm{II}}^{\mathrm{iso}} = -\frac{1}{4}b - \frac{1}{3}b, \tag{4.18}$$

$$z_{\mathrm{III}}^{\mathrm{iso}} = -\frac{1}{4}b - \frac{2}{3}b. \tag{4.19}$$

Figure 4.14: The figure shows the differential displacement maps of the degenerate and non-degenerate core structures of the 1/2[111] screw dislocation. The bcc lattice is viewed from the [111] direction, where atoms are colored according to which 111 plane they belong. The numbers indicate columns of atoms employed in the text.

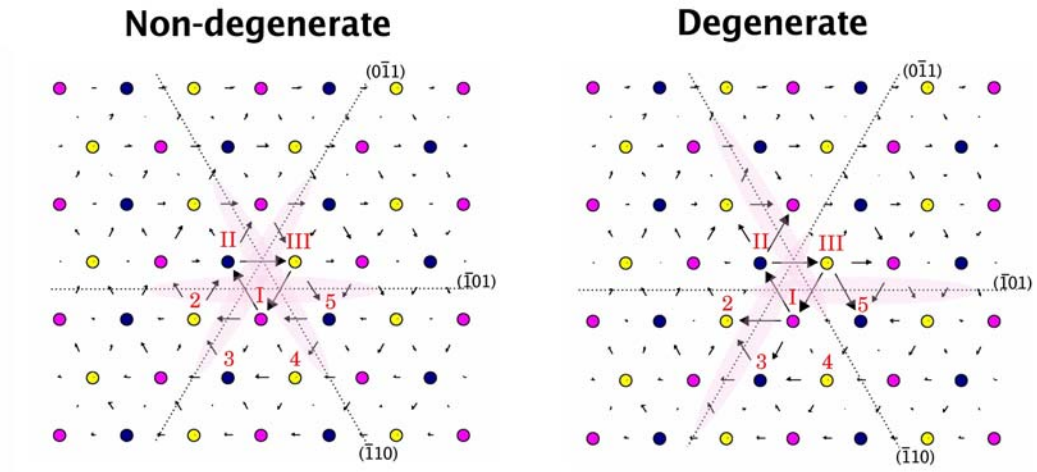

The displacement field of the non-degenerate core is actually very similar to the isotropic displacement field. The main difference with the degenerate core is that the central rows are shifted by $\pm b/6$, that is

$$z_{\rm I} = z_{\rm I}^{\rm iso} \pm b/6 \tag{4.20}$$
$$z_{\rm II} = z_{\rm II}^{\rm iso} \pm b/6, \tag{4.21}$$
$$z_{\rm III} = z_{\rm III}^{\rm iso} \pm b/6, \tag{4.22}$$

while the other strings have not been displaced appreciably from the initial isotropic displacement field. Because the two shifts are equivalent, this gives rise to two degenerate polarizations of the core. We will now investigate the stability of the non-degenerate core with respect to a simultaneous displacement of the central rows, that is

$$z_{\rm I}(u) = z_{\rm I}^{\rm iso} + u \tag{4.23}$$
$$z_{\rm II}(u) = z_{\rm II}^{\rm iso} + u \tag{4.24}$$
$$z_{\rm III}(u) = z_{\rm III}^{\rm iso} + u \tag{4.25}$$
$$z_j = z_j^{\rm iso} \text{ for } j \neq \text{I, II, III.} \tag{4.26}$$

The change in energy of the system will be then determined exclusively by the interaction of the central rows with their nearest neighbor strings.

Figure 4.15: Detail of figure 4.14 without displacement field and with the position of the dislocation line C_1 and the angles α, β and γ between the dislocation line and the strings 2, 3 and I as employed in the text.

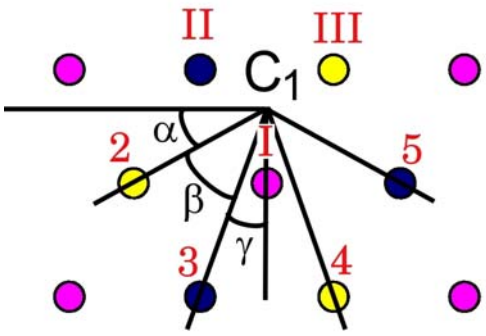

Because of symmetry considerations, it is sufficient to consider the change in energy due to the interaction of string number I with string number 2, 3, 4 and 5. The next step is to determine the position of string number 2, 3, 4 and 5 in the isotropic displacement field. The positions in the bcc lattice are given by

$$z_2^{\rm bcc} = z_4^{\rm bcc} = -\frac{1}{3}b \tag{4.27}$$

$$z_3^{\rm bcc} = z_5^{\rm bcc} = +\frac{1}{3}b \tag{4.28}$$

Referring to figure 4.15 for the angles α, β and γ, the position of the strings in the isotropic displacement field then becomes

$$z_2 = z_2^{\rm iso} = -\frac{1}{3}b - \frac{\alpha}{2\pi}b \tag{4.29}$$

$$z_3 = z_3^{\rm iso} = +\frac{1}{3}b - \frac{\alpha+\beta}{2\pi}b \tag{4.30}$$

$$z_4 = z_4^{\rm iso} = -\frac{1}{3}b - \frac{\alpha+\beta+2\gamma}{2\pi}b \tag{4.31}$$

$$z_5 = z_5^{\rm iso} = +\frac{1}{3}b - \frac{\alpha+2\beta+2\gamma}{2\pi}b. \tag{4.32}$$

so that the relative displacement of the string is

$$z_{\mathrm{I}}(u) - z_2 = u - \frac{1}{4}b + \frac{1}{3}b + \frac{\alpha}{2\pi}b \tag{4.33}$$

$$z_{\mathrm{I}}(u) - z_3 = u - \frac{1}{4}b - \frac{1}{3}b + \frac{\alpha+\beta}{2\pi}b \tag{4.34}$$

$$z_{\mathrm{I}}(u) - z_4 = u - \frac{1}{4}b + \frac{1}{3}b + \frac{\alpha+\beta+2\gamma}{2\pi}b \tag{4.35}$$

$$z_{\mathrm{I}}(u) - z_5 = u - \frac{1}{4}b - \frac{1}{3}b + \frac{\alpha+2\beta+2\gamma}{2\pi}b. \tag{4.36}$$

It is easy to see that

$$\alpha = \frac{2\pi}{12} \tag{4.37}$$

$$\alpha+\beta+\gamma = \frac{2\pi}{4}, \tag{4.38}$$

and using this in the previous equations we get

$$z_{\mathrm{I}}(u) - z_2 = u + \frac{1}{6}b \tag{4.39}$$

$$z_{\mathrm{I}}(u) - z_3 = u - \frac{1}{3}b - \frac{\gamma}{2\pi}b \tag{4.40}$$

$$z_{\mathrm{I}}(u) - z_4 = u + \frac{1}{3}b + \frac{\gamma}{2\pi}b \tag{4.41}$$

$$z_{\mathrm{I}}(u) - z_5 = u - \frac{1}{2}b. \tag{4.42}$$

The change in energy when displacing the central rows by u from their initial positions, given by isotropic displacement field, will thus be proportional to

$$\Delta E(u) = U(u+\frac{1}{6}b) + U(u-\frac{1}{6}b) + U(u-\frac{1}{3}b-\frac{\gamma}{2\pi}b) + U(u+\frac{1}{3}b+\frac{\gamma}{2\pi}b). \tag{4.43}$$

It is easy to check that the first derivative of the energy change with respect to u is zero, because the function U is symmetric. The second derivative at $u = 0$ is

given by

$$\begin{aligned}\frac{\partial^2 \Delta E(0)}{\partial s^2} &= 2U^{(2)}(\frac{1}{6}b) + 2U^{(2)}(\frac{1}{3}b + \frac{\gamma}{2\pi}b) \\ &= \frac{1}{3}C_\sigma^{1/2} + \frac{1}{3}\sigma^{(2)}(\frac{\gamma}{2\pi}b) + \frac{1}{3}\left[\sigma^{(2)}(\frac{1}{3}b - \frac{\gamma}{2\pi}b) - \sigma^{(2)}(\frac{1}{3}b + \frac{\gamma}{2\pi}b)\right]. \\ &\approx \frac{1}{3}C_\sigma^{1/2} + \frac{1}{3}\sigma^{(2)}(0) - \frac{2}{3}\sigma^{(3)}(\frac{1}{3}b)\frac{\gamma}{2\pi}b\end{aligned}$$

In the last row we have made a Taylor expansion because $\gamma/(2\pi) \sim 1/20$ is relatively small, and because the model functions, and thus also σ, are continuous up to the fifth order. Note that, by symmetry, $\sigma^{(3)}(0) = 0$. The term $\sigma^{(2)}(0)$ is positive and is expected to be almost independent on the particular fit of the DD potential, because all the fits considered here have exactly the same second order elastic constants. The last term is expected to be small, as it is a first order term in $\gamma/(2\pi)$. In case $C_\sigma^{1/2}$ is negative, then $\sigma^{(3)}(\frac{1}{3}b)$ is negative and the third term contributes to the stability of the non-degenerate core. We have thus also shown analytically how $C_\sigma^{1/2}$ is linked to the stability of the non-degenerate core, in addition to the correlation found previously in the fits of the DD potential.

Chapter 5

Conclusions

5.1 Summary

Three new fits of the DD potential have been successfully optimized to second and third order experimental elastic constants of α-iron, and to point defect and screw dislocation core structure properties from DFT. The new fits have been compared, in the perspective of radiation damage studies, with modern semi empirical potentials for bcc iron. In general all the semi empirical potentials suffer from similar limitations.

The relative formation energies, which are correlated to the migration properties, of the dumbbell type self-interstitial defects can be reproduced from DFT, but not the relative formation energies of the octahedral and tetrahedral type. The mean absolute value for the formation energy of self-interstitials is overestimated by ~ 0.3 eV by the ABO and the CS3 potentials with respect to DFT, but this does not seem to have any significant effect in cascade damage simulations, as shown in [21]. The value for the migration energy of the $\langle 110 \rangle$ dumbbell is scattered around the DFT and experimental value by about ~ 0.1 eV. The semi-empirical potentials generally overestimate, with the exception of Mend04, the DFT vacancy migration energy by 0.1 to 0.2 eV. The semi-empirical potentials also underestimate, with the exception of CS2, CS3-30 and CS3-33, the vacancy formation energy by 0.2 to 0.3 eV. The experimental formation volumes of the point defects are well reproduced, with the notable exception of the CS2 potential, which clearly underestimates the formation volume on the $\langle 110 \rangle$ self-interstitial defect. Also with respect to the energy difference between small clusters of self-interstitial oriented along $\langle 110 \rangle$ or $\langle 111 \rangle$ the semi-empirical potentials show the general behavior that by increasing the size of the cluster, the $\langle 111 \rangle$ orientation becomes energetically more favored, in agreement with DFT.

The 0 K cohesive energy of the DD Potential was found to be a different quantity than the 0 K equilibrium energy per atom, contrary to the other semi-empirical potentials, where these are the same quantity. This property of the DD Potential is consistent with spin-polarized DFT, where the cohesive energy and the equilibrium energy per atom are different quantities. The cohesive energy was not included in the objective function of the optimization algorithm. Nevertheless, the cohesive energy of the new fits is not dramatically out of range compared to the experimental and DFT value, and moreover can be corrected by modifying the low density limit of the embedding function. The ferromagnetic bcc is the ground state for all the new fits of the DD potential, followed in order of increasing energy by the ferromagnetic fcc, the non-magnetic bcc and the non-magnetic fcc. The parameters of the formula for the local ferromagnetic moment were fitted to both the DFT local magnetic moment distribution in the $\langle 110 \rangle$ dumbbell core and the bulk ferromagnetic moment as a function of volume. The bulk moment in the ferromagnetic bcc was fitted to 2.2 μ_B for all the fits of the DD potential. The bulk moment of the ferromagnetic fcc phase was found to be ~ 2.5 μ_B for the CS3 potentials with an equilibrium volume per atom $\sim 10\%$ bigger than that of the ferromagnetic bcc, and thus resembles the high spin ferromagnetic fcc found in DFT. The ground state fcc phase predicted by DFT is however anti-ferromagnetic with an equilibrium volume per atom $\sim 10\%$ *smaller* than that of the ferromagnetic bcc. The elastic properties of the other phases, and in particular C', are at odds with DFT calculations. The energy difference between the non-magnetic and ferromagnetic bcc is generally well reproduced. The energy difference between the non-magnetic and ferromagnetic fcc is overestimated. The bulk properties of the ferromagnetic bcc are generally well reproduced by the new fits: the thermal expansion coefficient of the new fits is now closer to the experimental linear extrapolation at 0 K. The linear extrapolation is appropriate in this case since molecular dynamics is a classical method.

The diffusion coefficient has been estimated by an MD simulation of the $\langle 110 \rangle$ dumbbell in the range from 300 K to 700 K. In this range the diffusion coefficient shows an exponential dependence which can be well described by standard rate theory using the activation energy for migration calculated by static methods. At room temperature there is a significant scatter in the diffusion coefficient between the semi-empirical potentials. This difference can be well explained by the differences in the migration energies, where in order of increasing migration energy, the diffusion coefficient decreases, the pre-exponential factor thus plays a minor role. This is particularly evident when looking at Mend04 and CS3-33, both with an activation energy of ~ 0.3 eV, very close to DFT and the experimental value, and both with very similar diffusion coefficients over the entire temperature range. At 600 K, the scatter in the predictions of the semi-empirical potentials falls within

the range from 1×10^{-6} cm^2/s to 10 $\times10^{-6}$ cm^2/s. At room temperatures the scatter extends over three orders of magnitude. For the vacancy, assuming the same pre exponential factor for all the semi empirical potentials, the vacancy diffusion coefficient is scattered by four orders of magnitude at room temperature, an by two orders of magnitude at 600 K.

The formation free energy of the $\langle 110 \rangle$ dumbbell has been calculated by the harmonic, quasi-harmonic and thermodynamical integration method in the range from 300 K to 600 K. The formation free entropy of the self-interstitial given by the semi-empirical potentials is seen to fall within a bandwidth of 30 k_B when using the harmonic method, within 20 k_B when using the quasi-harmonic method, and within 6 k_B when using the thermodynamical integration method. The thermodynamical technique is limited by the onset of diffusion, but can be employed when diffusion can still be considered a rare event, and the point defect has time to thermalize between the jumps. The formation free energy of the $\langle 111 \rangle$ dumbbell could not be calculated, because it is unstable at all temperatures.

Because of the above, the question as to whether the $\langle 111 \rangle$ configuration becomes favored at higher temperatures cannot be answered. As emerged from the analysis of diffusion, moreover, at temperatures approaching 600 K the $\langle 110 \rangle$ self-interstitial is frequently rotating, and every time it migrates it comes closer to the $\langle 111 \rangle$ orientation, but also to the other self-interstitial geometries, like the octahedral and tetrahedral, which are almost energetically degenerate with the $\langle 111 \rangle$ dumbbell. It is thus clear that as the temperature is increased, the dumbbell will spend less and less time oriented along $\langle 110 \rangle$, until, very likely, at sufficiently high temperatures the orientation cannot be determined any longer. We thus propose that only at low temperatures it is possible to consider the different orientations of a single dumbbell as distinct entities. At higher temperatures, with frequent diffusion events, the orientation of the point defect becomes more and more undetermined.

We have also derived new expressions for the magnetic moment, the Stoner parameter and the Stoner exchange energy in the DD potential formalism based on a more exact derivation. The Stoner parameter of the new fits is significantly higher than the Stoner parameter of CS2. We have thus discussed a way to optimize the parameters for the magnetic moment is such a way that this can be related to the Stoner exchange energy by a similar Stoner parameter for all the DD potentials, such as to allow a more meaningful comparison between these models. This has been partly discussed in the appendix, together with a detailed derivation of the DD potential formalism.

The occurrence of degenerate versus non-degenerate ground state core structures of the $b = 1/2[111]$ screw dislocation could be explained within the Suzuki-Takeuchi model. For the short range semi-empirical potentials considered in this

work, the structure is determined entirely by the single string potential and the interactions between next nearest neighbor strings. By fitting to the DFT single string potential, it was possible to control the core structure of the screw dislocation to be non-degenerate, in agreement with DFT. This is however not enough to reproduce, even qualitatively, the DFT $\langle \overline{2}11 \rangle$ Peierls potential. The Peierls potential of the semi-empirical potentials shows a double hump structure with a midway configuration energetically degenerate with the soft core, in addition to this, even if all the potentials have a very similar single string potential, the potentials lead to very different values for the Peierls barrier. Because of the existence of an additional minima it is possible to define either a full height double kink, which is the type of kink investigated in the literature, or an half height double kink, which has never been considered before. The half height double kink is for every potential the lower energy path for migration of the screw dislocation, with a formation energy of approximately half that of the full height double kink.

5.2 Outlook

In this section we want to conclude this work with some remarks about ongoing development of the DD potential and some ideas for further research:

- The new fits of the DD potential presented in this work are not yet suited for cascade damage simulations, because one first needs to fit the intermediate interaction range, and this development is being carried out by the European Fusion Development Agreement.

- It would be useful to test the new fits with the spin lattice dynamics algorithm, in particular to investigate the thermal expansion curve and the dependence of the anisotropic elastic constants on temperature. It would be then also very interesting to see what is the effect of including the spin degrees of freedom to the formation free energy of the self-interstitial and to the diffusion coefficient, which can be calculated by the dynamical methods described in this work, and also to repeat both calculations for the vacancy. This would give for the first time an estimation of the magnetic fluctuation contribution to fundamental point defect properties.

- The migration mechanism of the screw dislocation should be better characterized. It would be interesting to calculate the Peierls stress dependence on the type of applied stress, considering also the isostatic component, the dependence of the Peierls stress on temperature, and to perform molecular dynamics calculations to further investigate the kink pair formation mechanism, or more generally to perform a multiscale comparison with experiments

to investigate whether the details of the zero stress and zero temperature migration mechanism are actually so important. Research is ongoing to understand why the Peierls potential predicted by the semi empirical potentials is so different from the Peierls potential calculated from DFT.

- One should investigate whether it is possible to stabilize the fcc phase at least at higher temperatures by letting some parameters of the DD potential vary with temperature, as for instance the magnetic parameter B. Since at high temperatures the fcc phase is paramagnetic, one should also try to perform spin lattice dynamics on this system. Also it would be interesting to extend the DD potential to include the fourth moment of the electronic density of states to try improving the description of the fcc phase at zero temperatures.

- The DD potential formalism should be extended beyond pure elements to describe magnetism in alloys, and then applied for instance to the study of magnetic effects in binary Fe-Cr and Fe-Ni systems. As a guidance to this, one may refer to the recent development of a Tight Binding Stoner model for binary Fe-Cr systems [105].

- We suggest to further develop the fitting strategy to include some improved statistical analysis of the generated fits and to be then able to correlate the model parameters, the objective function weights and the fitted properties, so as to speed up the fitting process, and to get more easily some information about the accuracy and flexibility of any given embedded atom method potential.

Appendix A

The DD potential formalism

We now derive the DD potential formalism in a similar way as in the original derivation [1]. The first part of the derivations are fully equivalent, the only difference is that here we do not approximate (A.23) to the fourth order. We show that neglecting the sixth order has a negligible effect near equilibrium, but not at low densities, although this regime corresponds anyhow to the very limits of the main assumptions leading to the DD potential. We then derive new expressions for the magnetic moment, the Stoner exchange energy and the Stoner parameter, as given by the DD potential formalism, without approximating (A.23) to the fourth order. We then compare the so derived Stoner exchange energy and Stoner parameters as predicted by the fits of the DD potential, and discuss a way to define a local magnetic moment which allows comparison between the different fits of the DD potential.

Consider a general expression for the band energy of electrons assuming that the form of the density of states *per atom per spin* does not depend on the magnetic moment ζ

$$E_{\mathrm{tot}}(N,\zeta) = \int_{-\infty}^{\epsilon_{F\uparrow}} ED(E)dE + \int_{-\infty}^{\epsilon_{F\downarrow}} ED(E)dE - I_S\zeta^2/4 \tag{A.1}$$

The first two terms give the energies of the filled majority and minority spin subbands given by integrals of the density of states up to the Fermi energies $\epsilon_{F\uparrow}$ and $\epsilon_{F\downarrow}$ of spin up and down electrons. The last term

$$E_{\mathrm{X}}(\zeta) = -\frac{1}{4}I_S\zeta^2 \tag{A.2}$$

is the electron Stoner exchange energy with a constant Stoner parameter I_S in units of eV per μ_B^2. This form is subject to the charge neutrality condition [44]

asserting that in a metal the total number of electrons per atom remains constant

$$N = \int_{-\infty}^{\epsilon_{F\uparrow}} D(E)dE + \int_{-\infty}^{\epsilon_{F\downarrow}} D(E)dE = \text{constant}. \tag{A.3}$$

The magnetic moment *per atom* ζ is given by the difference between the occupation numbers of spin up and down states

$$\zeta = \int_{-\infty}^{\epsilon_{F\uparrow}} D(E)dE - \int_{-\infty}^{\epsilon_{F\downarrow}} D(E)dE. \tag{A.4}$$

Note that in equation A.1-A.4 the Fermi energies themselves are functions of the total number of electrons in the band N and the magnetic moment ζ. The equilibrium condition of this model requires that the chemical potentials of spin up and down electrons be equal, that is

$$\mu_\uparrow = \frac{\partial E_{\text{tot}}(N,\zeta)}{\partial N_\uparrow} = \frac{\partial E_{\text{tot}}(N,\zeta)}{\partial N_\downarrow} = \mu_\downarrow. \tag{A.5}$$

The stability condition requires that if some electrons change spin orientation for instance from up to down, then there is a restoring force in the opposite direction, in this case to change the spin from down to up. In mathematical terms the following equations must be satisfied

$$\frac{\partial\left(\mu_\uparrow - \mu_\downarrow\right)}{\partial N_\uparrow} > 0 \tag{A.6}$$

$$\frac{\partial\left(\mu_\uparrow - \mu_\downarrow\right)}{\partial N_\downarrow} < 0. \tag{A.7}$$

It can be very easily shown by substituting $\frac{\partial}{\partial N_\uparrow} = \frac{\partial}{\partial N} + \frac{\partial}{\partial \zeta}$ and $\frac{\partial}{\partial N_\downarrow} = \frac{\partial}{\partial N} - \frac{\partial}{\partial \zeta}$ in the above equations that the equilibrium and stability conditions are equivalent to

$$\frac{\partial E_{\text{tot}}(N,\zeta)}{\partial \zeta} = 0 \tag{A.8}$$

$$\frac{\partial^2 E_{\text{tot}}(N,\zeta)}{\partial \zeta^2} > 0. \tag{A.9}$$

With the total number of electrons per atom N being constant the stability of the system is thus only determined by the magnetic moment ζ. It can be shown [1] that a condition that relates the Fermi energies of the spin up and down sub-bands

to the *equilibrium* value of the magnetic moment is

$$\zeta = \frac{\epsilon_{F\uparrow}(N,\zeta) - \epsilon_{F\downarrow}(N,\zeta)}{I_S}, \tag{A.10}$$

and here it can be seen that $\zeta = 0$ is always an equilibrium point. Because the stability condition of any equilibrium point is given by

$$\frac{1}{2}\left[\frac{1}{D(\epsilon_{F\uparrow})} + \frac{1}{D(\epsilon_{F\downarrow})}\right] - I_S > 0, \tag{A.11}$$

we see that if

$$\frac{1}{D(\epsilon_F)} - I_S < 0, \tag{A.12}$$

then the non-magnetic solution $\zeta = 0$ is unstable. This criterion has proved very effective in explaining the onset of ferromagnetism across the transition metal elements [77].

The model described above needs the specification of the non-magnetic density of states and the total number of electrons per atoms and either the equilibrium magnetic moment per atom ζ or the Stoner parameter I_S. Calculations of the non-magnetic density of states based on the full potential LMTO and the tight-binding approximation developed in [67] were used in [1] to test this model at equilibrium. In both cases it could be shown that the non-magnetic configuration of bcc iron is unstable assuming respectively I_S =0.78 eV/(atom μ_{B}^2) and I_S =0.66 eV/(atom μ_{B}^2), and that the instability gives rise to the formation of a symmetry broken magnetic configuration with $\zeta \simeq \pm 2.26\mu_B$ which is very close to the experimental value. The assumption for the Stoner parameter is justified since the experimental and theoretical value for pure α-iron lies in the range from 0.4 to 0.8 eV/(atom μ_{B}^2) [67, 77].

To derive a semi-empirical magnetic potential we assume that the density of states $D(E)$ has a scalable form

$$D(E) = \frac{1}{W} F\left(\frac{E}{W}\right). \tag{A.13}$$

If we choose the origin of the energy axis at the Fermi energy of the non-magnetic state we find that the total number of electrons occupying the band equals

$$N = 2\int_{-\infty}^{0} D(E)dE. \tag{A.14}$$

We see that the number of electrons per atom N remains independent of W, as

required by the local charge neutrality condition. We now further assume that near the origin (or, equivalently, in the vicinity of the Fermi energy of the non-magnetic state) the density of states $D(E)$ is approximated by a parabola

$$D(E) = \frac{1}{W} F\left(\frac{E}{W}\right) \simeq \frac{1}{W}\left[a - b\left(\frac{E}{W}\right)^2\right] \tag{A.15}$$

where $a > 0$ and $b > 0$ are constant factors independent of W. Formula A.15 is valid within the interval of energies where $|E| < W\sqrt{a/b}$, because outside this interval the parabola takes negative values. Since the parabolic term in A.15 gives the leading contribution to the density of states near the Fermi energy of the non-magnetic state we are now dealing with a density of states which is symmetric around the Fermi level of the non-magnetic state.

Let the non-magnetic density of states be symmetric around the non-magnetic Fermi level, that is $D(E) = D(-E)$, then from A.3 it follows that

$$\int_0^{\epsilon_{F\uparrow}} D(E)dE = -\int_0^{\epsilon_{F\downarrow}} D(E)dE = \int_{\epsilon_{F\downarrow}}^{0} D(E)dE. \tag{A.16}$$

Because the density of states is a positive quantity then either $\epsilon_{F\uparrow} > 0 > \epsilon_{F\downarrow}$ or $\epsilon_{F\uparrow} < 0 < \epsilon_{F\downarrow}$, but from the symmetry of the density it follows

$$\epsilon_{F\uparrow} = -\epsilon_{F\downarrow} = \Delta, \tag{A.17}$$

where we have defined a new parameter Δ which is appropriate to treat the model in the case that the density of states in assumed symmetric around the non-magnetic Fermi level. We now show that in this case the problem of finding a solution for A.1 via minimization over ζ is fully equivalent to a minimization over Δ, because

$$\frac{\partial \zeta}{\partial \Delta} = \frac{\partial}{\partial \Delta}\int_{-\Delta}^{\Delta} D(E)dE = 2D\left(\Delta\right) \tag{A.18}$$

and the density of states is positive.

To find a solution we now assume a simplified non-magnetic density of states

$$D_P(E) = \begin{cases} \alpha - 3\beta E^2 & \text{if } |E| < \Delta_{\max} = \sqrt{\frac{\alpha}{3\beta}}, \\ 0 & \text{otherwise} \end{cases} \tag{A.19}$$

α and β are positive quantities and we look for minima of the total energy

$$E_{\text{tot}}(\Delta) = E_{\text{Band}}(\Delta) - \frac{1}{4} I_S \zeta^2 = 2 \int_{-\infty}^{0} E D_P(E) dE + f(\Delta) \tag{A.20}$$

for $\Delta \in (-\Delta_{\max}, +\Delta_{\max})$, where the magnetic moment is then given by

$$\zeta = \int_{-\Delta}^{\Delta} D_P(E) dE = \alpha \Delta^2 - \frac{3}{2} \beta \Delta^4 \tag{A.21}$$

and the band part of the total energy is

$$E_{\text{Band}}(\Delta) = 2 \int_{-\infty}^{0} E D_P(E) dE + \int_{0}^{\Delta} E D_P(E) dE + \int_{0}^{-\Delta} E D_P(E) dE. \tag{A.22}$$

The first term is a negative contribution that does not depend on Δ and we will thus ignore this term for the moment since it plays no role in the minimization: we thus need to minimize the function

$$f(\Delta) = -I_S \beta^2 \Delta^6 + \beta \left(2 I_S \alpha - \frac{3}{2} \right) \Delta^4 + \left(\alpha - I_S \alpha^2 \right) \Delta^2. \tag{A.23}$$

It turns out that the problem of finding the extrema of f is exactly solvable with some elementary mathematics which is not the case to reproduce here, but involves only differentiation, solution of second order equations and some algebra. The derivative of f vanishes at the following values of Δ

$$\Delta_1 = 0 \tag{A.24}$$

$$\Delta_{2,3} = \pm \sqrt{\frac{1}{I_S \beta} \left(I_S \alpha - 1 \right)} \tag{A.25}$$

$$\Delta_{4,5} = \pm \Delta_{\max} \tag{A.26}$$

and by evaluating the second derivative of f at these values of Δ gives

$$\frac{\partial^2 f(\Delta_1)}{\partial \Delta^2} > 0 \quad \text{if and only if} \quad \alpha I_S \leq 1 \tag{A.27}$$

$$\frac{\partial^2 f(\Delta_{2,3})}{\partial \Delta^2} > 0 \quad \text{if and only if} \quad 1 \leq \alpha I_S \leq \frac{3}{2}. \tag{A.28}$$

If $\frac{3}{2} \leq \alpha I_S$ then there is no minima in $(-\Delta_{\max}, +\Delta_{\max})$ and the minimal value is taken at the border of the interval. For every set of positive parameters α, β and I_S there exists thus a well defined minima of f. The first solution Δ_1 corresponds

to a non-magnetic state since the magnetic moment vanishes. For the other two solutions the state is magnetic since the magnetic moment does not vanish. The total energy of the system defined by the density of states A.19 is thus given by

$$E_{\rm tot} = 2\int_{-\infty}^{0} ED_P(E)dE + \begin{cases} 0 & \text{if} \quad \alpha I_S \leq 1 \\ -\frac{1}{2}\frac{1}{I_S^2\beta}\left(I_S\alpha - 1\right)^2 & \text{if} \quad 1 \leq \alpha I_S \leq \frac{3}{2} \\ -\frac{4}{27}I_S\frac{\alpha^3}{\beta} + \frac{1}{6}\frac{\alpha^2}{\beta} & \text{otherwise} \end{cases} \tag{A.29}$$

Considering now a density of states which is approximated by (A.15) near the non-magnetic Fermi level, we arrive at the embedding functional

$$F(\rho) = -A\sqrt{\rho} - BM(\rho) \tag{A.30}$$

where

$$M(\rho) = \begin{cases} 0 & \text{if} \quad \rho \geq 1 \\ -3\sqrt{\rho}\left(1-\sqrt{\rho}\right)^2 & \text{if} \quad \frac{4}{9} \leq \rho \leq 1 \\ \sqrt{\rho} - \frac{8}{9} & \text{otherwise} \end{cases} \tag{A.31}$$

This was derived by substituting in (A.29)

$$\alpha = a/W, \tag{A.32}$$

$$\beta = b/(3W^3), \tag{A.33}$$

$$B = 1/2I_S\frac{a^3}{b}, \tag{A.34}$$

$$\sqrt{\rho} = \frac{W}{I_S a}, \tag{A.35}$$

In the last equation ρ is the local electronic density, which can be written as a sum over pair functions. We thus assume here that the energy may be written as a sum over local contributions, and that the square of the width of the local electronic density of states W^2 may written as a sum over pair functions, which is the usual assumption of any EAM or Finnis-Sinclair potential. A is a further constant obtained by collecting the remaining constant terms.

The magnetic functional (2.9) on page 17 is very similar to the one derived here (A.31). The only difference in the previous published derivation [1] is that the function f in (A.23) was approximate to the fourth order in Δ, and then the solution was obtained within Ginzburg-Landau theory for second order phase transitions. The embedding functional was then further approximated using a smooth function. In figure A.1 we have compared these two magnetic functionals, and we see that they are almost identical in the region $\rho > 0.3$ and differ somehow only at low densities. At least for all the fits considered in this work, the equilibrium

Figure A.1: Comparison of the magnetic part of the embedding functions M as derived in [1] (DD potential) and as derived in this appendix.

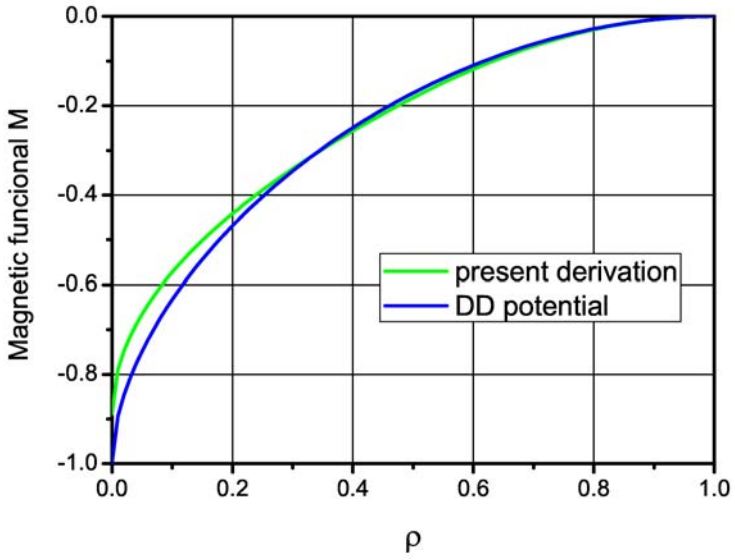

value for the density in the bcc lattice varies between 0.48 for CS2 to 0.60 for CS3-30, thus both functionals are to be considered equivalent for situations not involving free surfaces. Note that anyhow the low density regime corresponds to the limits of validity of the parabolic approximation, that is when the minimum of f is at $\Delta_{\max}$: it is thus not very surprising to find a difference in the functionals right in this region where a simple parabolic approximation of the density of states becomes very questionable.

By making the same substitutions (A.35) we obtain from (A.21) the magnetic moment

$$\zeta(\rho) = \begin{cases} 0 & \text{if} \quad \rho \geq 1 \\ \sqrt{24}\sqrt{\frac{B}{I_S}}\sqrt{\rho}\sqrt{1-\sqrt{\rho}} & \text{if} \quad \frac{4}{9} \leq \rho \leq 1 \\ \sqrt{24}\sqrt{\frac{B}{I_S}}\sqrt{\frac{4}{9}}\sqrt{1-\sqrt{\frac{4}{9}}} & \text{otherwise} \end{cases} \tag{A.36}$$

This new expression gives us the opportunity to determine explicitly the Stoner parameter of the DD potential, which is then simply given by

$$I_S = \frac{24B}{\zeta_0^2}\rho_0^2(1-\sqrt{\rho_0}) \tag{A.37}$$

where ζ_0 is the equilibrium magnetic moment per atom and ρ_0 is the equilibrium

Table A.1: Stoner parameters of the DD potentials. First column is the equilibrium density per atom, second column the magnetic moment per atom in units of μ_B, third column the fitting parameter B and last column the Stoner parameter in eV/(atom μ_B^2)

	ρ_0	ζ_0	B	I_S
CS2	0.48	2.2	1.642	1.20
CS3-00	0.598	2.2	6.32	4.25
CS3-30	0.59	2.2	4.75	3.22
CS3-33	0.545	2.2	8.09	5.72

electronic density per atom. Assuming $\zeta_0 = 2.2$ as the equilibrium magnetic moment per atom, the Stoner parameter can the be calculated for each fit of the DD potential, see table A.1, where the Stoner parameter is given in units of eV/(atom μ_{B}^2). We see that the CS3 fits strongly overestimate the Stoner parameter, which from experiments and theoretical calculations should be in the range from 0.4 to 0.8 eV/(atom μ_{B}^2). When looking at figures 3.3 on page 37 we note however that the CS3 fits are very close in predicting the energy difference between the non-magnetic and ferromagnetic bcc phases as a function of volume per atom from DFT calculations. Because the Stoner parameter was derived from the parabolic approximation, we thus conclude that the present form of the DD potential is not accurate enough to capture the correct dependence of the Stoner exchange energy on the magnetic moment, when higher priority is given to the bulk and defect properties in the optimization, including anharmonic effects. The relative Stoner exchange energy, as given by the DD potential, is

$$E_{\mathrm{X}}(\zeta) - E_{\mathrm{X}}(\zeta_0) = \frac{1}{4} I_S \left(\zeta_0^2 - \zeta^2\right) = 6B \left(\rho_0(1 - \sqrt{\rho_0}) - \rho(1 - \sqrt{\rho})\right). \qquad \text{(A.38)}$$

which is represented in figure A.2 by the continuous lines as a function of hydrostatic pressure. Note again that only the energy difference between the magnetic and non-magnetic bcc phases was included in the fitting, but not the Stoner exchange energy. We would now like to define, in the spirit of a very genuine empirical approach like in most of this work, an effective magnetic moment ζ^* that can be related to the Stoner exchange energy (A.38) using the same Stoner parameter I_S^* for all the semi empirical potentials. We thus need to equate the Stoner exchange energy as given by ζ^* and I_S^*, to the one given by (A.38),

$$(\zeta^*)^2 = \frac{I_S}{I_S^*}\zeta^2 + \left(1 - \frac{I_S}{I_S^*}\right)\zeta_0^2. \qquad \text{(A.39)}$$

It is easy to see that if $I_S^* < I_S$, then a solution only exists for $\zeta > \sqrt{1 - \frac{I_S^*}{I_S}}\zeta_0$, and

Figure A.2: Relative exchange energy as a function of hydrostatic pressure. The continuous line is the value given by (A.38) and the dotted line the value given by the optimal parametrization.

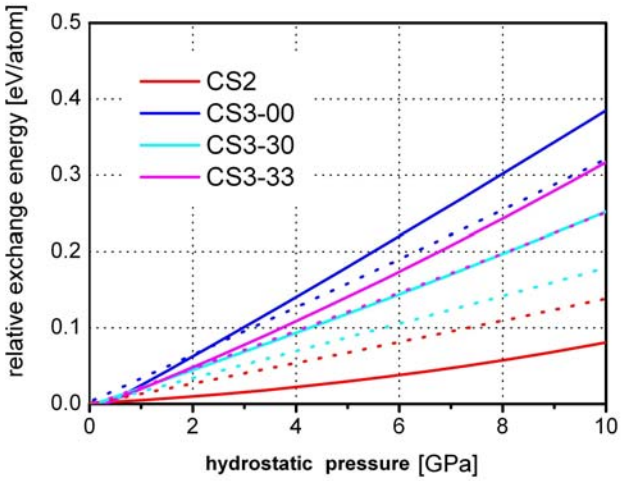

that

$$\zeta^* = 0 \text{ for } \zeta = \sqrt{1 - \frac{I_S^*}{I_S}}\zeta_0. \tag{A.40}$$

We have then employed this equations as a guidance to optimize the three parameters of the previously published formula for the local ferromagnetic moment (2.11) on page 18, with ζ_0=2.2μ_B and I_S^*=0.7 eV/atom: the parameter ρ_c, at which the magnetic moment in formula (2.11) vanishes, is approximately determined by (A.40), and the other two parameters are then fitted to get a good match with (A.40). The parameters so obtained are given in table 3.5 and have been employed in chapter 3 to compare the magnetic moment predicted by the fits of the DD potential. The dotted lines in figure A.2 give the exchange energy as predicted by the optimal parametrization. The reason why the match is not exact is that we have also considered the magnetic moment distribution in the core of the ⟨110⟩ self-interstitial as given from DFT to determine the parameters, see table 3.6 on page 65.

Curriculum Vitae

Personal Information

Samuele Chiesa
Via alla peschiera
6874 Castel S. Pietro
Switzerland
tel: +41 (0)79 820 75 36
chiesax@hotmail.com

I was born and raised in the Italian speaking part of Switzerland. After high school I moved to study physics at the Swiss Federal Institute of Technology (ETHZ) and later on to get my PhD degree in materials science at the Paul Scherrer Institute (PSI), so that for the last ten years I have lived in Zürich. My undergraduate education was mainly mathematical-analytic, I later on did some experiences in teaching and turned to programming during my PhD. I also enjoy reading, traveling, skiing and playing tennis.

Education

PhD in materials science from the Swiss Federal Institute of Technology Lausanne (2006-2010) Thesis director: Prof. Helena Van Swygenhoven-Moens (PSI), Supervisor: Dr. Peter Derlet (PSI), Cosupervisor: Dr. Sergei Dudarev (Imperial College London). Thesis title: *Optimization of embedded atom method interatomic potentials to simulate defect structures and magnetism in α-iron.* Mostly numerical work.

Master (pre Bologna system) in physics from ETHZ (1999-2005) Thesis title: *Finite temperature localization in the tight binding Anderson model.* Analytical work. References: Prof. G. M. Graf (ETHZ) and Dr. J. Schenker (Michigan

State University).

High school, Liceo cantonale Mendrisio (1995-1999) Scientific orientation.

Publications

- Chiesa S, Derlet P M, Dudarev S L, Van Swygenhoven H, *Atomistic calculation of elastic constants of α-iron containing point defects by means of magnetic interatomic potentials*, Journal of nuclear materials, 386, 49-51 (2009), conference proceeding.
- Chiesa S, Derlet P M, Dudarev S L, *Free energy of a ⟨110⟩ dumbbell interstitial defect in bcc Fe: harmonic and anharmonic contributions*, Physical Review B, 79, 214109 (2009). Two of the optimized fits have been published in the appendix of this paper.
- Chiesa S, Gilbert M R, Dudarev S L, Derlet P M, Van Swygenhoven H, *The non-degenerate core structure of a 1/2⟨111⟩ screw dislocation in bcc transition metals modeled using Finnis-Sinclair potentials: The necessary and sufficient conditions*, Philosophical magazine, 89, 3235-3243 (2009), special issue: twenty five years of Finnis-Sinclair potentials.

In preparation

- Chiesa S, Derlet P M, Dudarev S L, Van Swygenhoven H, *Optimization of embedded atom method interatomic potentials to simulate defect structures and magnetism in α-Fe.*. This paper will summarize the main results of my PhD thesis.

Conference contributions

I have given the following talks.

- The development of a magnetic potential for BCC Fe, Euromat 2009, Glasgow (UK).
- Free energy of a ⟨110⟩ dumbbell interstitial defect in BCC Fe: Harmonic and anharmonic contributions, Euromat 2009, Glasgow (UK).
- The development of a magnetic potential for BCC Fe, EMMM 2009, Zürich (CH).

- The development of a magnetic potential for BCC Fe, MRS fall meeting 2009, Boston (USA).

Computer knowledge

I have good programming skills. My PhD was done by employing Fortran and Linux Bash scripts and LaTeX. I have also a basic knowledge of C++, MS Office, MATLAB and Mathematica.

Languages

My mother tongue is Italian. I am fluent in English, French and German. I have improved my English a lot during my PhD. My knowledge of the German language stems from my undergraduate studies in Zürich.

Bibliography

[1] S. L. Dudarev and P. M. Derlet. A 'magnetic' interatomic potential for molecular dynamics simulations. *Journal of Physics-condensed Matter*, 17 (44):7097–7118, November 2005.

[2] G. J. Ackland. Two-band second moment model for transition metals and alloys. *Journal of Nuclear Materials*, 351(1-3):20–27, June 2006.

[3] S. L. Dudarev and P. M. Derlet. A 'magnetic' interatomic potential for molecular dynamics simulations (vol 17, pg 7097, 2006). *Journal of Physics-condensed Matter*, 19(23):239001, June 2007.

[4] D. Nguyen-Manh, A. P. Horsfield, and S. L. Dudarev. Self-interstitial atom defects in bcc transition metals: Group-specific trends. *Physical Review B*, 73(2):020101, January 2006.

[5] H. C. Herper, E. Hoffmann, and P. Entel. Ab initio full-potential study of the structural and magnetic phase stability of iron. *Physical Review B*, 60 (6):3839–3848, August 1999.

[6] P. M. Derlet and S. L. Dudarev. Million-atom molecular dynamics simulations of magnetic iron. *Progress In Materials Science*, 52(2-3):299–318, February 2007.

[7] S. L. Dudarev and P. M. Derlet. Molecular dynamics modelling of radiation defects in ferromagnetic alpha-iron. *Journal of Nuclear Materials*, 367:251–256, August 2007.

[8] P. W. Ma, W. C. Liu, C. H. Woo, and S. L. Dudarev. Large-scale molecular dynamics simulation of magnetic properties of amorphous iron under pressure. *Journal of Applied Physics*, 101(7):073908, April 2007.

[9] P. Van Zwol, P. M. Derlet, H. Van Swygenhoven, and S. L. Dudarev. Bccfe surface and cluster magnetism using a magnetic potential. *Surface Science*, 601(16):3512–3520, August 2007.

[10] P. W. Ma, C. H. Woo, and S. L. Dudarev. Large-scale simulation of the spin-lattice dynamics in ferromagnetic iron. *Physical Review B*, 78(2):024434, July 2008.

[11] P. W. Ma, C. H. Woo, and S. L. Dudarev. High-temperature dynamics of surface magnetism in iron thin films. *Philosophical Magazine*, 89(32):2921–2933, 2009.

[12] S. L. Dudarev, J. L. Boutard, R. Lasser, M. J. Caturla, P. M. Derlet, M. Fivel, C. C. Fu, M. Y. Lavrentiev, L. Malerba, M. Mrovec, D. Nguyen-Manh, K. Nordlund, M. Perlado, R. Schaublin, H. Van Swygenhoven, D. Terentyev, J. Wallenius, D. Weygand, and F. Willaime. The eu programme for modelling radiation effects in fusion reactor materials: An overview of recent advances and future goals. *Journal of Nuclear Materials*, 386:1–7, April 2009.

[13] L. Malerba. Molecular dynamics simulation of displacement cascades in alpha-fe: A critical review. *Journal of Nuclear Materials*, 351(1-3):28–38, June 2006.

[14] D. A. Terentyev, L. Malerba, and M. Hou. Dimensionality of interstitial cluster motion in bcc-fe. *Physical Review B*, 75(10):104108, March 2007.

[15] D. Terentyev, L. Malerba, D. J. Bacon, and Y. N. Osetsky. The effect of temperature and strain rate on the interaction between an edge dislocation and an interstitial dislocation loop in alpha-iron. *Journal of Physics-condensed Matter*, 19(45):456211, November 2007.

[16] H. J. Wollenberger. *Physical Metallurgy*, volume II. 1996. chapter 18 pp.

[17] C. Domain and C. S. Becquart. Ab initio calculations of defects in fe and dilute fe-cu alloys. *Physical Review B*, 65(2):024103, December 2001.

[18] M. I. Mendelev, S. Han, D. J. Srolovitz, G. J. Ackland, D. Y. Sun, and M. Asta. Development of new interatomic potentials appropriate for crystalline and liquid iron. *Philosophical Magazine*, 83(35):3977–3994, December 2003.

[19] G. J. Ackland, M. I. Mendelev, D. J. Srolovitz, S. Han, and A. V. Barashev. Development of an interatomic potential for phosphorus impurities in alpha-iron. *Journal of Physics-condensed Matter*, 16(27):S2629–S2642, July 2004.

[20] M. Muller, P. Erhart, and K. Albe. Analytic bond-order potential for bcc and fcc iron - comparison with established embedded-atom method potentials. *Journal of Physics-condensed Matter*, 19(32):326220, August 2007.

[21] C. Bjorkas and K. Nordlund. Comparative study of cascade damage in fe simulated with recent potentials. *Nuclear Instruments & Methods In Physics Research Section B-beam Interactions With Materials and Atoms*, 259(2): 853–860, June 2007.

[22] S. M. H. Haghighat, J. Fikar, and R. Schaublin. Effect of interatomic potential on the behavior of dislocation-defect interaction simulation in alpha-fe. *Journal of Nuclear Materials*, 382(2-3):147–153, December 2008.

[23] G. J. Ackland, D. J. Bacon, A. F. Calder, and T. Harry. Computer simulation of point defect properties in dilute fe-cu alloy using a many-body interatomic potential. *Philosophical Magazine A-physics of Condensed Matter Structure Defects and Mechanical Properties*, 75(3):713–732, March 1997.

[24] M. C. Marinica and F. Willaime. Orientation of interstitials in clusters in alpha-fe: A comparison between empirical potentials. *Sol. Stat. Phenomena*, 129:67–74, 2007.

[25] S. P. Fitzgerald and D. Nguyen-Manh. Peierls potential for crowdions in the bcc transition metals. *Physical Review Letters*, 101(11):115504, September 2008.

[26] A. Souidi, C. S. Becquart, C. Domain, D. Terentyev, L. Malerba, A. F. Calder, D. J. Bacon, R. E. Stoller, Y. N. Osetsky, and M. Hou. Dependence of radiation damage accumulation in iron on underlying models of displacement cascades and subsequent defect migration. *Journal of Nuclear Materials*, 355 (1-3):89–103, September 2006.

[27] D. Terentyev and L. Malerba. Interaction of ¡ 100 ¿ and (1/2)¡ 111 ¿ dislocation loops with point defects in ferritic alloys. *Journal of Nuclear Materials*, 377(1):141–146, June 2008.

[28] D. Terentyev, L. Malerba, P. Klaver, and P. Olsson. Formation of stable sessile interstitial complexes in reactions between glissile dislocation loops in bcc fe. *Journal of Nuclear Materials*, 382(2-3):126–133, December 2008.

[29] S. Chiesa, P. M. Derlet, S. L. Dudarev, and H. Van Swygenhoven. Atomistic calculation of elastic constants of alpha-iron containing point defects by means of magnetic interatomic potentials. *Journal of Nuclear Materials*, 386:49–51, April 2009.

[30] S. L. Dudarev, R. Bullough, and P. M. Derlet. Effect of the alpha-gamma phase transition on the stability of dislocation loops in bcc iron. *Physical Review Letters*, 100(13):135503, April 2008.

[31] M. R. Gilbert, S. L. Dudarev, P. M. Derlet, and D. G. Pettifor. Structure and metastability of mesoscopic vacancy and interstitial loop defects in iron and tungsten. *Journal of Physics-condensed Matter*, 20(34):345214, August 2008.

[32] M. Samaras, M. Victoria, and W. Hoffelner. The structure, role and flexibility of grain boundaries. *Materials For Future Fusion and Fission Technologies*, 1125:101–107, 2009.

[33] F. G. Djurabekova, L. Malerba, C. Domain, and C. S. Becquart. Stability and mobility of small vacancy and copper-vacancy clusters in bcc-fe: An atomistic kinetic monte carlo study. *Nuclear Instruments & Methods In Physics Research Section B-beam Interactions With Materials and Atoms*, 255(1):47–51, February 2007.

[34] J. Kuriplach, O. Melikhova, C. Domain, C. S. Becquart, D. Kulikov, L. Malerba, M. Hou, A. Almazouzi, C. A. Duque, and A. L. Morales. Vacancy-solute complexes and their clusters in iron. *Applied Surface Science*, 252(9):3303–3308, February 2006.

[35] R. Schaublin and N. Balue. Radiation damage in ferritic/martensitic steels for fusion reactors: a simulation point of view. *Nuclear Fusion*, 47(12):1690–1695, December 2007.

[36] G. Lucas and R. Schaublin. Stability of helium bubbles in alpha-iron: A molecular dynamics study. *Journal of Nuclear Materials*, 386:360–362, April 2009.

[37] D. M. Duffy and A. M. Rutherford. Including the effects of electronic stopping and electron-ion interactions in radiation damage simulations. *Journal of Physics-condensed Matter*, 19(1):016207, January 2007.

[38] S. Chiesa, P. M. Derlet, and S. L. Dudarev. Free energy of a 110 dumbbell interstitial defect in bcc fe: Harmonic and anharmonic contributions. *Physical Review B*, 79(21):214109, June 2009.

[39] S. L. Frederiksen and K. W. Jacobsen. Density functional theory studies of screw dislocation core structures in bcc metals. *Philosophical Magazine*, 83 (3):365–375, January 2003.

[40] C. Engin, L. Sandoval, and H. M. Urbassek. Characterization of fe potentials with respect to the stability of the bcc and fcc phase. *Modelling and Simulation In Materials Science and Engineering*, 16(3):035005, April 2008.

[41] R. A. JOHNSON. Interstitials + vacancies in alpha iron. *Physical Review A-general Physics*, 134(5A):1329–&, 1964.

[42] M. S. DAW and M. I. BASKES. Embedded-atom method - derivation and application to impurities, surfaces, and other defects in metals. *Physical Review B*, 29(12):6443–6453, 1984.

[43] M. W. FINNIS and J. E. SINCLAIR. A simple empirical n-body potential for transition-metals. *Philosophical Magazine A-physics of Condensed Matter Structure Defects and Mechanical Properties*, 50(1):45–55, 1984.

[44] G. J. ACKLAND, M. W. FINNIS, and V. VITEK. Validity of the 2nd moment tight-binding model. *Journal of Physics F-metal Physics*, 18(8): L153–L157, August 1988.

[45] A. F. CALDER and D. J. BACON. A molecular-dynamics study of displacement cascades in alpha-iron. *Journal of Nuclear Materials*, 207:25–45, December 1993.

[46] C. C. Fu, F. Willaime, and P. Ordejón. Stability and mobility of mono- and di-interstitials in α-fe. *Physical Review Letters*, 92(17):175503, April 2004.

[47] L. Ventelon and F. Willaime. Core structure and peierls potential of screw dislocations in alpha-fe from first principles: cluster versus dipole approaches. *Journal of Computer-aided Materials Design*, 14:85–94, 2007.

[48] J. TERSOFF. Chemical order in amorphous-silicon carbide. *Physical Review B*, 49(23):16349–16352, June 1994.

[49] D. W. BRENNER. Empirical potential for hydrocarbons for use in simulating the chemical vapor-deposition of diamond films. *Physical Review B*, 42(15): 9458–9471, November 1990.

[50] D. G. Pettifor and I. I. Oleinik. Analytic bond-order potentials beyond tersoff-brenner. i. theory. *Physical Review B*, 59(13):8487–8499, April 1999.

[51] K. Albe, K. Nordlund, and R. S. Averback. Modeling the metal-semiconductor interaction: Analytical bond-order potential for platinum-carbon. *Physical Review B*, 65(19):195124, May 2002.

[52] N. Juslin, P. Erhart, P. Traskelin, J. Nord, K. O. E. Henriksson, K. Nordlund, E. Salonen, and K. Albe. Analytical interatomic potential for modeling nonequilibrium processes in the w-c-h system. *Journal of Applied Physics*, 98(12):123520, December 2005.

[53] Rahman A Parinello M. Polymorphic transitions in single-crystals - a new molecular-dynamics method. *JOURNAL OF APPLIED PHYSICS*, 52:7182–7190, 1981.

[54] N. RIDLEY and H. STUART. Lattice parameter anomalies at curie point of pure iron. *Journal of Physics D-applied Physics*, 1(10):1291–&, 1968.

[55] F. W. SHEARD. Calculation of the thermal expansion of solids from the 3rd-order elastic constants. *Philosophical Magazine*, 3(36):1381–1390, 1958.

[56] A. S. Bhalla. *Low properties of dielectric crystals: piezoelectric, pyroelectric, and related constants*, volume NS III/29b. Landolt-Börnstein, 1993. 635 pp.

[57] M. Lopuszynski and J. A. Majewski. Ab initio calculations of third-order elastic constants and related properties for selected semiconductors. *Physical Review B*, 76(4):045202, July 2007.

[58] J. P. Hirth and J. Lothe. *Theory of dislocations*. Wiley-Interscience Publication, 1982.

[59] R. C. LINCOLN, K. M. KOLIWAD, and P. B. GHATE. Morse-potential evaluation of 2nd- and 3rd-order elastic constants of some cubic metals. *Physical Review*, 157(3):463–&, 1967.

[60] M. W. GUINAN and D. N. BESHERS. Pressure derivatives of elastic constants of alpha-iron to 10 kbs. *Journal of Physics and Chemistry of Solids*, 29(3):541–&, 1968.

[61] Marcus P M Hong Ma, Qiu S L. Pressure instability of bcc iron. *Phys. Rev. B*, 66:024113, 2002.

[62] J. J. Adams, D. S. Agosta, R. G. Leisure, and H. Ledbetter. Elastic constants of monocrystal iron from 3 to 500 k. *Journal of Applied Physics*, 100(11): 113530, December 2006.

[63] M. R. Gilbert and S. L. Dudarev. Ab initio multi-string frenkel-kontorova model for a b = a/2[111] screw dislocation in bcc iron. *Philosophical Magazine*, 90(7-8):1035–1061, 2010.

[64] S. Chiesa, M. R. Gilbert, S. L. Dudarev, P. M. Derlet, and H. Van Swygenhoven. The non-degenerate core structure of a 1/2 ¡ 111 ¿ screw dislocation in bcc transition metals modelled using finnis-sinclair potentials: The necessary and sufficient conditions. *Philosophical Magazine*, 89(34-36):3235–3243, 2009.

[65] R. Drautz and D. G. Pettifor. Valence-dependent analytic bond-order potential for transition metals. *Physical Review B*, 74(17):174117, November 2006.

[66] A. E. CARLSSON. Angular forces in group-vi transition-metals - application to w(100). *Physical Review B*, 44(13):6590–6597, October 1991.

[67] G. Q. Liu, D. Nguyen-Manh, B. G. Liu, and D. G. Pettifor. Magnetic properties of point defects in iron within the tight-binding-bond stoner model. *Physical Review B*, 71(17):174115, May 2005.

[68] C. C. Fu, J. Dalla Torre, F. Willaime, J. L. Bocquet, and A. Barbu. Multiscale modelling of defect kinetics in irradiated iron. *Nature Materials*, 4(1): 68–74, January 2005.

[69] S. Y. Huang, D. L. Worthington, M. Asta, V. Ozolins, G. Ghosh, and P. K. Liaw. Calculation of impurity diffusivities in alpha-fe using first-principles methods. *Acta Materialia*, 58(6):1982–1993, April 2010.

[70] F. Willaime, C. C. Fu, M. C. Marinica, and J. Dalla Torre. Stability and mobility of self-interstitials and small interstitial clusters in alpha-iron: ab initio and empirical potential calculations. *Nuclear Instruments & Methods In Physics Research Section B-beam Interactions With Materials and Atoms*, 228:92–99, January 2005.

[71] Gary S. Was. *Fundamentals of Radiation Materials Science: Metals and Alloys*. 2007.

[72] C. Domain, C. S. Becquart, and J. Foct. Ab initio study of foreign interstitial atom (c, n) interactions with intrinsic point defects in alpha-fe. *Physical Review B*, 69(14):144112, April 2004.

[73] P. M. Derlet, D. Nguyen-Manh, and S. L. Dudarev. Multiscale modeling of crowdion and vacancy defects in body-centered-cubic transition metals. *Physical Review B*, 76(5):054107, August 2007.

[74] G. Lucas and R. Schaublin. Vibrational contributions to the stability of point defects in bcc iron: A first-principles study. *Nuclear Instruments & Methods In Physics Research Section B-beam Interactions With Materials and Atoms*, 267(18):3009–3012, September 2009.

[75] S. M. FOILES. Evaluation of harmonic methods for calculating the free-energy of defects in solids. *Physical Review B*, 49(21):14930–14938, June 1994.

[76] D. FRENKEL and A. J. C. LADD. New monte-carlo method to compute the free-energy of arbitrary solids - application to the fcc and hcp phases of hard-spheres. *Journal of Chemical Physics*, 81(7):3188–3193, 1984.

[77] Jürgen Kübler. *Theory of Itinerant Electron Magnetism*. Oxford science pubblications, 2000.

[78] V. VITEK, R. C. PERRIN, and D. K. BOWEN. Core structure of 1/2(111) screw dislocations in b c c crystals. *Philosophical Magazine*, 21(173):1049–&, 1970.

[79] S. Ismail-Beigi and T. A. Arias. Ab initio study of screw dislocations in mo and ta: A new picture of plasticity in bcc transition metals. *Physical Review Letters*, 84(7):1499–1502, February 2000.

[80] M. Mrovec, R. Groger, A. G. Bailey, D. Nguyen-Manh, C. Elsasser, and V. Vitek. Bond-order potential for simulations of extended defects in tungsten. *Physical Review B*, 75(10):104119, March 2007.

[81] Chang J Li J Yip S Cai W, Bulatov V. *Dislocation core effects on mobility*, volume 12. North-Holland, 2004. 1 pp. Chapter 64 in Dislocations in Solids.

[82] J. Chaussidon, M. Fivel, and D. Rodney. The glide of screw dislocations in bcc fe: Atomistic static and dynamic simulations. *Acta Materialia*, 54(13): 3407–3416, August 2006.

[83] B. G. Mendis, Y. Mishin, C. S. Hartley, and K. J. Hemker. Hrem imaging of screw dislocation core structures in bcc metals. *Electron Microscopy of Molecular and Atom-Scale Mechanical Behavior, Chemistry and Structure*, 839:73–78, 2005.

[84] B. G. Mendis, Y. Mishin, C. S. Hartley, and K. J. Hemker. Use of the nye tensor in analyzing hrem images of bcc screw dislocations. *Philosophical Magazine*, 86(29-31):4607–4640, October 2006.

[85] J. E. DORN and S. RAJNAK. Nucleation of kink pairs + peierls mechanism of plastic deformation. *Transactions of the Metallurgical Society of Aime*, 230(5):1052–&, 1964.

[86] K. Okazaki. Solid-solution hardening and softening in binary iron alloys. *Journal of Materials Science*, 31(4):1087–1099, February 1996.

[87] W. A. SPITZIG and A. S. KEH. Orientation dependence of strain-rate sensitivity and thermally activated flow in iron single crystals. *Acta Metallurgica*, 18(9):1021–&, 1970.

[88] K. Edagawa, T. Suzuki, and S. Takeuchi. Motion of a screw dislocation in a two-dimensional peierls potential. *Physical Review B*, 55(10):6180–6187, March 1997.

[89] R. Groger, V. Racherla, J. L. Bassani, and V. Vitek. Multiscale modeling of plastic deformation of molybdenum and tungsten: Ii. yield criterion for single crystals based on atomistic studies of glide of 1/2 ¡ 111 ¿ screw dislocations. *Acta Materialia*, 56(19):5412–5425, November 2008.

[90] R. Groger, A. G. Bailey, and V. Vitek. Multiscale modeling of plastic deformation of molybdenum and tungsten: I. atomistic studies of the core structure and glide of 1/2 ¡ 111 ¿ screw dislocations at 0 k. *Acta Materialia*, 56(19):5401–5411, November 2008.

[91] R. Groger and V. Vitek. Multiscale modeling of plastic deformation of molybdenum and tungsten. iii. effects of temperature and plastic strain rate. *Acta Materialia*, 56(19):5426–5439, November 2008.

[92] E. Clouet, L. Ventelon, and F. Willaime. Dislocation core energies and core fields from first principles. *Physical Review Letters*, 102(5):055502, February 2009.

[93] G. MILLS, H. JONSSON, and G. K. SCHENTER. Reversible work transition-state theory - application to dissociative adsorption of hydrogen. *Surface Science*, 324(2-3):305–337, February 1995.

[94] G. Henkelman and H. Jonsson. Improved tangent estimate in the nudged elastic band method for finding minimum energy paths and saddle points. *Journal of Chemical Physics*, 113(22):9978–9985, December 2000.

[95] V. V. Bulatov, J. F. Justo, W. Cai, and S. Yip. Kink asymmetry and multiplicity in dislocation cores. *Physical Review Letters*, 79(25):5042–5045, December 1997.

[96] D. A. Terentyev and L. Malerba. Effect of cr atoms on the formation of double kinks in screw dislocations in fe and its correlation with solute hardening and softening in fe-cr alloys. *Computational Materials Science*, 43(4):855–866, October 2008.

[97] A. H. W. Ngan and M. Wen. Dislocation kink-pair energetics and pencil glide in body-centered-cubic crystals. *Physical Review Letters*, 87(7):075505, August 2001.

[98] C. Domain and G. Monnet. Simulation of screw dislocation motion in iron by molecular dynamics simulations. *Physical Review Letters*, 95(21):215506, November 2005.

[99] L. Ventelon, F. Willaime, and P. Leyronnas. Atomistic simulation of single kinks of screw dislocations in alpha-fe. *Journal of Nuclear Materials*, 386: 26–29, April 2009.

[100] W Cai. Modeling dislocations using a periodic cell. *In: S. Yip (ed.) Handbook of Materials Modeling*, page 813, 2005.

[101] J. Li, C. Z. Wang, J. P. Chang, W. Cai, V. V. Bulatov, K. M. Ho, and S. Yip. Core energy and peierls stress of a screw dislocation in bcc molybdenum: A periodic-cell tight-binding study. *Physical Review B*, 70(10):104113, September 2004.

[102] S. TAKEUCHI. Core structure of a screw dislocation in the bcc lattice and its relation to slip behavior of alpha-iron. *Philosophical Magazine A-physics of Condensed Matter Structure Defects and Mechanical Properties*, 39(5): 661–671, 1979.

[103] Z. Chen, N. Kioussis, N. Ghoniem, and T. Hasebe. Lubricant effect of copper nanoclusters on the dislocation core in alpha-fe. *Physical Review B*, 77(1): 014103, January 2008.

[104] N. I. Medvedeva, Y. N. Gornostyrev, and A. J. Freeman. Solid solution softening in bcc mo alloys: Effect of transition-metal additions on dislocation structure and mobility. *Physical Review B*, 72(13):134107, October 2005.

[105] D. Nguyen-Manh and S. L. Dudarev. Model many-body stoner hamiltonian for binary fecr alloys. *Physical Review B*, 80(10):104440, September 2009.